The solution processing and stoichiometry of ZrC

M Mastoroudes

orcid.org 0000-0002-6282-7965

Thesis accepted in fulfilment of the requirements for the degree *Doctor of Philosophy in Engineering Sciences* at the North-West University

Promoter:	Prof J Markgraaff
Co-promoter:	Dr JC Barry

Graduation:	May 2020
Student number:	2114282

ACKNOWLEDGEMENTS

Soli Deo Gloria

I would like to extend my gratitude to:

- The Advanced Metals Initiative (AMI) of the Department of Science and Technology (DST) for their financial support.

- Prof. J. Markgraaff and Dr J.C. Barry for their help and guidance during the study.

- Necsa for the use of their laboratories, as well as the personnel of the department of Applied Chemistry, especially the following Plasma Technology personnel: Mr J.L. Havenga, Mr P.C. Smith, Mr M.M. Makhofane, Mr K.P. Mthimkhulu and Mr R.W. Makhubela for their help and support while working with the vacuum furnace.

- The following persons for their help with the various analytical techniques used during this study:
    - Dr L.R. Tiedt of the North-West University and Dr S.J. Lötter of Necsa (SEM/EDS),
    - Mr T. Ntsoane of Necsa and Dr S. Verryn of XRD Analytical and Consulting CC (XRD and Rietveld refinement),
    - Mr B.M. Vilakazi of Necsa (TG/DSC),
    - Mr J.L. Mokgawa and Mr S. Sibiya of PAL (IGF)

- My family for supporting me throughout my studies and providing me with much needed encouragement.

- And my husband, Bruce, for all his love, support and encouragement throughout the study.

ABSTRACT

In the aftermath of the incident at Fukushima Daiichi, evaluation of alternative Accident-Tolerant Fuel (ATF) was initiated. The purpose of ATF systems is to achieve greater safety margins by delaying the initiation of severe core damage that can lead to more managing time to implement mitigation strategies during an accident situation. One of the candidate materials identified for new cladding materials for ATF is zirconium carbide (ZrC).

This thesis reviewed the crystal chemistry and phase chemistry of ZrC in an effort to derive the fundamental parameters that influence the synthesis of ZrC. Standard fabrication methods were also reviewed in order to *find and apply* a method to synthesize and characterize *stoichiometric* and *non-stoichiometric* ZrC powders. Solution-based processing was reviewed in order to find a method to synthesize ZrC powders.

After a brief overview of some of the properties of zirconium carbide, it was found that the stoichiometry of ZrC greatly influences the parameters as well as the mechanical and thermal properties. The review found that a thorough understanding of the thermodynamic, mechanical, and heat transport properties of ZrC is limited and that a careful and systematic detailed characterization of ZrC, as a function of stoichiometry, with emphasis on resulting microstructures, is required.

Various synthesis routes of the formation of quality ZrC that can be used in the nuclear industry were reviewed. The review showed that solution-based synthesis routes hold the greatest advantage regarding control of the stoichiometry. The Pechini method was chosen to synthesize ZrC powders as a solution-based synthesis technique for ZrC. The Pechini method is also a simple and benign method for precursor preparation *via* the formation of an *in situ* polymerizable complex, *in situ* charring and *in situ* reaction at 1300 °C.

The Pechini method was used to prepare stoichiometric and non-stoichiometric ZrC powders. The variation of the stoichiometry of ZrC powders was investigated by varying the carbon content during the formation of ZrC powders. Carbothermal reduction reactions were carried out at various temperatures (1000 °C to 1500 °C) and the resulting powders were characterised by X-ray powder diffraction (XRD) analysis to identify the phases present. According to XRD analysis, the formation of ZrC starts at temperatures around 1200 °C and is substantially completed by 1500 °C. X-ray photoelectron spectroscopy (XPS) analysis showed that the synthesized ZrC powders are in close agreement to ZrC powders available commercially.

In order to achieve different stoichiometries of ZrC, the molar ratio of the starting materials, citric acid and zirconium oxychloride was varied, by varying the amount of citric acid added to the zirconium oxychloride during synthesis. The stoichiometries of the synthesized ZrC powders, using the Pechini method and carbothermal reduction, were determined by considering the XRD and Inert Gas Fusion (IGF) analyses results. Stoichiometries varying between $ZrC_{0.49}O_{0.51}$ and $ZrC_{0.96}O_{0.04}$ were derived for the synthesized ZrC powders. The amounts of carbon and oxygen (determined by IGF) in each sample revealed that even samples with an excess amount of initial carbon formed ZrC powders with a stoichiometry of $ZrC_{0.96}O_{0.04.}$ Comparing the lattice parameter of the synthesized ZrC powders with respect to the determined stoichiometric carbon content, the best results for ZrC synthesis *via* the Pechini method were achieved after carbothermal reduction at 1300 °C for 2 hours.

The Pechini method was chosen as synthesis method due to no oxygen being reported in the ZrC powders synthesized from this method, but like all of the other solution-based synthesis methods, the Pechini method also forms oxygen containing ZrC powders.

Based on these results, a process to remove the oxygen from the ZrC powders was investigated. By adding magnesium powder to the dried Pechini gels before carbothermal reduction, magnesiothermic reduction of the ZrO_2 in the dried gels was performed. XRD analysis of the reaction products of the magnesiothermic reduction of the dried gels of the Pechini method, pyrolysed at 900 °C, results in a powdered mixture of 56.0 wt. % ZrC and 44.0 wt. % MgO. These weight percentages when compared to the theoretical weight percentages calculated for ZrC and MgO (56.15% ZrC and 43.85% MgO) shows a near complete conversion into ZrC and MgO. The observation of MgO in the powdered samples shows that magnesium acts as an “oxygen-getter” during the synthesis of ZrC *via* magnesiothermic reduction.

After comparison of the d-spacing values of the ZrC data file JCPDS 00-035-0784, with the d-spacing values of S1.00-1500 it is concluded that the stoichiometry of the ZrC used to generate the ZrC data file JCPDS 00 035 0784, is closer to the stoichiometry of S1.00-1500, which is $ZrC_{0.96}O_{0.04.}$

Key words: Zirconium carbide, Stoichiometry of ZrC, Phase diagram, Carbothermal reduction, Sol-gel, Magnesiothermic reduction

TABLE OF CONTENT

LIST OF TABLES

LIST OF FIGURES

LIST OF ABBREVIATIONS

General abbreviations

A_N	Nucleophilic Addition
ATF	Accident Tolerant Fuel
bcc	body centred cubic
BWR	Boiling Water Reactor
CSIR	Council for Scientific and Industrial Research
CVD	Chemical Vapour Deposition
DiD	Defence in depth
fcc	face centred cubic
hcp	hexagonal close packed
IAEA	International Atomic Energy Agency
LOCA	loss-of-coolant-accident
LWR	Light Water Reactor
NECSA	The South African Nuclear Energy Corporation
NMISA	National Metrology Institute of South Africa
SHS	Self-propagating High temperature Synthesis
S_N	Nucleophilic Substitution
S_N2	Substitution Nucleophilic Bimolecular
SSM	Solid State Metathesis
TRISO	Tristructural isotropic

Chemical abbreviations

CA	citric acid
EG	ethylene glycol
m-ZrO_2	monoclinic zirconia
SiC	Silicon carbide
t-ZrO_2	tetragonal zirconia
YSZ	Yttria Stabilized Zirconia
ZOC	Zirconium oxychloride, $ZrOCl_2.8H_2O$
ZrC	Zirconium carbide
ZrO_2	Zirconium oxide, zirconia

Analytical abbreviations

DSC	Differential Scanning Calorimetry
EDS	Energy Dispersive Spectrometry
ESEM	Environmental Scanning Electron Microscope
IGF	Inert Gas Fusion
SEM	Scanning Electron Microscopy
TG	Thermogravimetry
XPS	X-ray photoelectron spectroscopy
XRD	X-ray diffraction

CHAPTER 1 INTRODUCTION

1.1 Background and problem statement

The 2011 earthquake near the coast of Japan and the subsequent tsunami led to severe damage of the Boiling Water Reactors (BWRs) at the Fukushima Daiichi nuclear power plant. The tsunami caused flooding and power outages of the pumps of the reactor cooling system. The resulting loss of coolant led to a loss-of-coolant-accident (LOCA). The incident at Fukushima Daiichi reasserted the need for safety and reliability at nuclear power plants (Charit, 2018).

The safety and reliability of nuclear power plants is extremely important. The implementation of the defence in depth (DiD) concept (IAEA, 1996) may be one method to slow or eliminate the release of radioactive materials and is centred on levels of protection and barriers in terms of safety. Fission products are confined by means of four successive physical barriers: the fuel matrix, the fuel cladding, the boundary of the reactor coolant system and the containment system. The cladding tubes provide an enclosure to the radioactive nuclear fuel and remain in constant contact with the cooling water during operation of the reactor, which also makes them vulnerable to corrosion (Alam *et al.*, 2011). The material used for cladding tubes must thus have the following qualities: low thermal neutron capture cross-section, high corrosion resistance, high thermal conductivity and high strength.

Zr-based alloys are widely used as materials for commercial Light Water Reactor (LWR) fuel cladding, due to the combination of a low thermal neutron capture cross-section, adequate corrosion resistance in high-temperature water, high melting point (1830 °C) and good thermal conductivity (Duan *et al.*, 2017, Charit, 2018).

During severe loss-of-coolant-accidents, the zirconium alloy fuel cladding of a BWR or LWR reactor core, becomes exposed to steam due to the ever increasing coolant water temperature. Decays of short-lived isotopes being produced in the core, will also continue to increase the temperature of the fuel and cladding (Wray and Marra, 2011). Rapid exothermic oxidation of Zr-alloy fuel will then begin at temperatures between 700 and 1000 °C under high steam pressures (Cheng *et al.*, 2016). This rapid oxidation/corrosion of the Zr-alloy gives rise to the formation of hydrogen according to Equation 1.1 (Charit, 2018, Duan *et al.*, 2017), that can lead to an explosion

$$Zr(s) + 2H_2O(g) \rightarrow ZrO_2(s) + 2H_2(g) \quad (1.1)$$

Furthermore, in the absence of an explosion, when the temperature exceeds 900 °C, fuel rod collapse and dislocation may occur due to polymorphic transformation of zirconium from the alpha phase (hcp) to the beta phase (bcc) (Charit, 2018). The phase change leads to the loss of mechanical strength of the Zr-alloy above 850 °C (Cheng *et al.*, 2016, Alam *et al.*, 2011), leading to possible exposure of radioactive material to the environment due to systematic fracture and cracking of the fuel rod. If the temperature increases further, the fuel pellets will melt at temperatures above 2500 °C (Cheng *et al.*, 2016).

In the aftermath of the incident at Fukushima Daiichi, evaluation of alternative Accident-Tolerant Fuel (ATF) was initiated, focusing mainly on the fuel designs of current LWRs.

Alternative ATF should meet the following requirements (Charit, 2018):

(i) Maintain high fuel safety under normal LWR operating conditions,

(ii) Under abnormal conditions, delay fission product release and meltdown with slower hydrogen generation due to lowered reaction kinetics with steam,

(iii) Possess sufficient strength at higher temperatures (1200 °C – 1500 °C) for longer times to maintain the integrity and geometry of the fuel assembly.

The purpose of ATF systems is to achieve greater safety margins by delaying the initiation of severe core damage (by approximately 5 – 20 hours), that can lead to more managing time to implement mitigation strategies during an accident situation (Pint *et al.*, 2015).

In the light of ATF, candidate materials for new cladding materials have been identified, which include: coated Zr-alloy (materials currently being considered for coatings are titanium, chromium and nitrides and carbides of titanium or chromium), Al-containing stainless steel, silicon carbide (SiC) fiber-reinforced SiC ceramic composites and refractory metal (mainly molybdenum alloy) (Zinkle *et al.*, 2014).

Due to the advantages of coating technology, this technology is currently being widely applied in cladding to increase the water corrosion and wear resistance. Coatings will aid in mitigating severe accident consequences by lowering the Zr-alloy's hydrogen absorption and hydrogen generation at high temperature and giving the cladding a higher melting point (Barrett *et al.*, 2012, Duan *et al.*, 2017).

The fabricating methodologies of coatings include magnetron sputtering, physical and chemical vapour deposition and laser deposition in order to obtain high adhesion to the Zr-alloy (Duan *et al.*, 2017). The development of Zr-based coated claddings is however, hindered by significant

disadvantages such as the lack of improvement on mechanical strength at higher temperature, the adhesion of the coating material to the Zr-alloy, phase stability of the coating at high temperatures, the neutron capture cross section of the coating material, irradiation susceptibility, thermal expansion coefficient, thermal conductivity and manufacturability of the tubes (Kim *et al.*, 2016, Duan *et al.*, 2017).

Zirconium carbide (ZrC) potentially meets the most important property criteria for fuel coating applications. ZrC is a refractory ceramic of one of the group IV transition metals. ZrC is applied in areas where it can be subjected to severe conditions of temperature, pressure and high mechanical stresses. ZrC has a high melting temperature (>3500 °C) and excellent thermomechanical properties, such as high thermal conductivity at elevated temperatures, (Katoh *et al.*, 2013). ZrC has a relatively low thermal neutron capture cross-section and weak damage sensitivity under irradiation, which makes it a good candidate for nuclear applications such as a coating material for nuclear fuel.

Although ZrC can serve as a coating that can protect Zr-fuel rods, Zr as a base metal is ductile and malleable. ZrC, on the other hand, as a transition metal carbide, will exhibit brittle failure similarly to ZrO_2 which was however, successfully deposited on Zr-alloy (presumably Zircaloy) after yttria stabilisation (YSZ) using sol-gel processing (Rezaee *et al.*, 2013).

Limited information on the stability of the stoichiometry and the microstructural homogeneity of ZrC exist and thus data on the properties of ZrC solid solutions need to be carefully determined and evaluated. Furthermore, a lack of thorough characterization due to non-stoichiometry leads to uncertainties regarding the mechanical properties of ZrC_x (Jackson *et al.*, 2011, Manara *et al.*, 2013, Katoh *et al.*, 2013) and published data on the properties of ZrC often contain little information on the synthesis. The potential of modification of the structure to conform to the expansion coefficient of Zr cladding also needs to be investigated.

1.2 Aim of the study

This thesis aims to review the crystal chemistry and the phase chemistry of ZrC in an effort to derive the fundamental parameters that influence the synthesis of ZrC. This thesis also aims to review fabrication methods in order to *find and apply* a method to synthesize and characterize *stoichiometric* and *non-stoichiometric* ZrC powders taking recognisance of the limiting chemistry.

Synthesized ZrC powders will be used in subsequent studies of the properties in order to find a ZrC_x composition that is less prone to cracking and brittle failure and composition susceptible to stabilisation as a protection layer on Zr nuclear fuel rod cladding.

In order to achieve the aim of this study the following objectives were identified:

1. Review of the phase and crystal chemistry and properties in view of possible strategies with reference to stability.

2. Review of possible processing methods in view of stoichiometric control and ease of processing and stabilisation.

3. Application and evaluation of the identified processing method to fabricate a stable ZrC_x composition.

1.3 References

ALAM, T., KHAN, M.K., PATHAK, M., RAVI, K., SINGH, R. and GUPTA, S.K. 2011. A review on the clad failure studies. *Nuclear Engineering and Design,* 241**,** 3658-3677.

BARRETT, K., BRAGG-SITTON, S. and GALICKI, D. 2012. Advanced LWR nuclear fuel cladding system development trade-off study. Idaho National Laboratory (INL).

CHARIT, I. 2018. Accident tolerant nuclear fuels and cladding materials. *The Journal of The Minerals, Metals & Materials Society (TMS),* 70**,** 173-175.

CHENG, B., KIM, Y.-J. and CHOU, P. 2016. Improving Accident Tolerance of Nuclear Fuel with Coated Mo-alloy Cladding. *Nuclear Engineering and Technology,* 48**,** 16-25.

DUAN, Z., YANG, H., SATOH, Y., MURAKAMI, K., KANO, S., ZHAO, Z., SHEN, J. and ABE, H. 2017. Current status of materials development of nuclear fuel cladding tubes for light water reactors. *Nuclear Engineering and Design,* 316**,** 131-150.

IAEA 1996. *Defence in Depth in Nuclear Safety,* Vienna, INTERNATIONAL ATOMIC ENERGY AGENCY.

JACKSON, H.F., JAYASEELAN, D.D., MANARA, D., PERINETTI CASONI, C. and LEE, W.E. 2011. Laser Melting of Zirconium Carbide: Determination of Phase Transitions in Refractory Ceramic Systems. *Journal of the American Ceramic Society,* 94**,** 3561-3569.

KATOH, Y., VASUDEVAMURTHY, G., NOZAWA, T. and SNEAD, L.L. 2013. Properties of zirconium carbide for nuclear fuel applications. *Journal of Nuclear Materials,* 441**,** 718-742.

KIM, H.-G., YANG, J.-H., KIM, W.-J. and KOO, Y.-H. 2016. Development Status of Accident-tolerant Fuel for Light Water Reactors in Korea. *Nuclear Engineering and Technology,* 48**,** 1-15.

MANARA, D., JACKSON, H.F., PERINETTI-CASONI, C., BOBORIDIS, K., WELLAND, M.J., LUZZI, L., OSSI, P.M. and LEE, W.E. 2013. The ZrC–C eutectic structure and melting behaviour: A high-temperature radiance spectroscopy study. *Journal of the European Ceramic Society,* 33**,** 1349-1361.

PINT, B.A., TERRANI, K.A., YAMAMOTO, Y. and SNEAD, L.L. 2015. Material Selection for Accident Tolerant Fuel Cladding. *Metallurgical and Materials Transactions E,* 2**,** 190-196.

REZAEE, S., RASHED, G.R. and GOLOZAR, M.A. 2013. Electrochemical and Oxidation Behavior of Yttria Stabilized Zirconia Coating on Zircaloy-4 Synthesized *via* Sol-Gel Process. *International Journal of Corrosion,* 2013**,** 1-9.

WRAY, P. and MARRA, J. 2011. Materials for Nuclear Energy in the Post-Fukushima Era. *American Ceramics Society Bulletin,* 90**,** 24-28.

ZINKLE, S.J., TERRANI, K.A., GEHIN, J.C., OTT, L.J. and SNEAD, L.L. 2014. Accident tolerant fuels for LWRs: A perspective. *Journal of Nuclear Materials,* 448**,** 374-379.

CHAPTER 2 CRYSTAL AND PHASE CHEMISTRY OF ZIRCONIUM CARBIDE

2.1 Introduction

As discussed in Chapter 1, ZrC can be subjected to severe conditions of temperature, pressure and high mechanical stresses, due to its properties. This chapter reviews the crystal and phase chemistry of ZrC as well as some of its mechanical and thermal properties in order to provide a better understanding of the ZrC structure. This chapter also identifies opportunities to alter the ZrC structure in order to improve the mechanical properties.

2.2 Crystal structure and phase chemistry

2.2.1 Crystal structure

Stoichiometric ZrC has a Zr content of 88.4 wt. % and a C content of 11.6 wt. % (Preiss *et al.*, 1998), but due to the occurrence of carbon vacancies in the octahedral sites of the fcc lattice of Zr, the composition can exist over a wide range of carbon-deficient non-stoichiometry with a variation of between 33 at. % and 50 at. % C at 1800 °C (Jackson *et al.*, 2011, Storms, 1967). The formation of the wide stoichiometric range is due to the low formation energies for carbon vacancies, created by the removal of carbon atoms from the sub-lattice (Katoh *et al.*, 2013).

ZrC crystallizes in the same space group *Fm3m* (space group 225) as rock salt (Figure 2.1) but with a lattice parameter of approximately 0.4698 nm (Sara, 1965). The lattice parameter of ZrC depends on the C/Zr ratio[a] in the ZrC structure which increases with an increase in the C/Zr ratio. At a C/Zr ratio of 0.83 ($ZrC_{0.83}$) the lattice parameter is a maximum of 0.4702 nm (Storms, 1967, Sara, 1965). When all the carbon vacancies are filled, the excess carbon precipitates at the grain boundaries for carbon-rich ZrC and the lattice parameter is not significantly dependant on the C/Zr ratio when the ratio is more than 0.98 (Katoh *et al.*, 2013).

[a] The C/Zr ratio is the fraction of C per 1 Zr atom or a shorthand to the stoichiometry of ZrC_x with x the C/Zr ratio

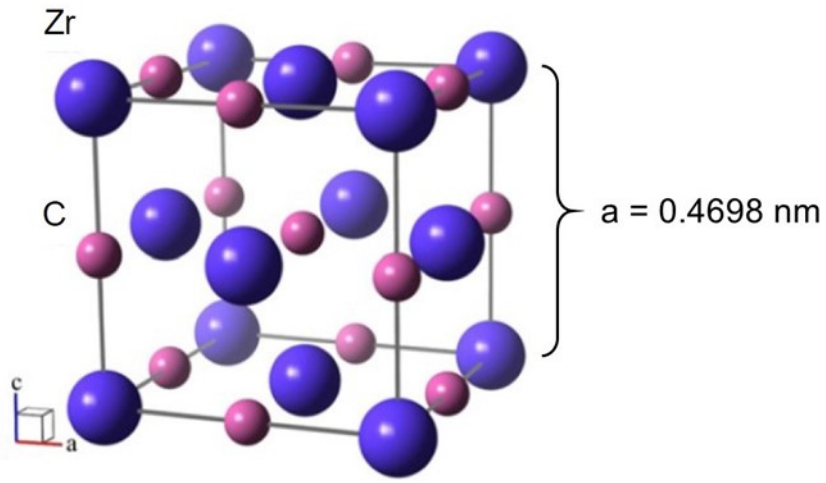

Figure 2.1: Representations of the crystal structure of ZrC (after Chinthaka Silva *et al.* (2012))

2.2.2 Phase chemistry

The Zr-C phase diagram has been determined by Guillermet (1995) using thermodynamic calculations and previously determined phase relations (Sara, 1965, Storms, 1967, Adelsberg *et al.*, 1966, Vil'k *et al.*, 1965, Rudy, 1969). Due to experimental uncertainties of the composition of equilibrium phases, a number of other researchers (Jackson *et al.*, 2011, Katoh *et al.*, 2013, Manara *et al.*, 2013) reviewed and endeavoured to complement previous work (Réjasse *et al.*, 2016). The phase diagrams reported in literature must be viewed at best as close approximations of the phase relations, because Zr is prone to oxygen-uptake and to some extent to nitrogen contamination (Katoh *et al.*, 2013). Jackson *et al.* (2011) investigated the phase relations by laser melting of prepared samples of ZrC with C/Zr ratios ranging between 0.66 and 2.6. Less than 1.0 wt. % oxygen and 0.001 wt. % nitrogen impurities were present in the samples and their (Jackson *et al.*, 2011) work correlated with the proposed phase diagram of Guillermet (1995).

Figure 2.2 presents the Zr-C phase diagram reviewed by Réjasse *et al.* (2016). (An enlargement of Figure 2.2 is also available in Appendix A as a reference guide.) Figure 2.2 has been provided with additional x axes of the C/Zr ratio and weight percentage carbon corresponding to each atomic fraction of carbon shown in the Zr-C phase diagram.

There is a general agreement that there are five stable condensed phases in the Zr-C system (Figure 2.2) (Guillermet, 1995):

1. A hcp Zr (α-Zr) phase
2. A bcc Zr (β-Zr) phase
3. ZrC_x ($0.55 \leq x \leq 0.98$) in a fcc structure
4. Graphite (C), and
5. A liquid phase.

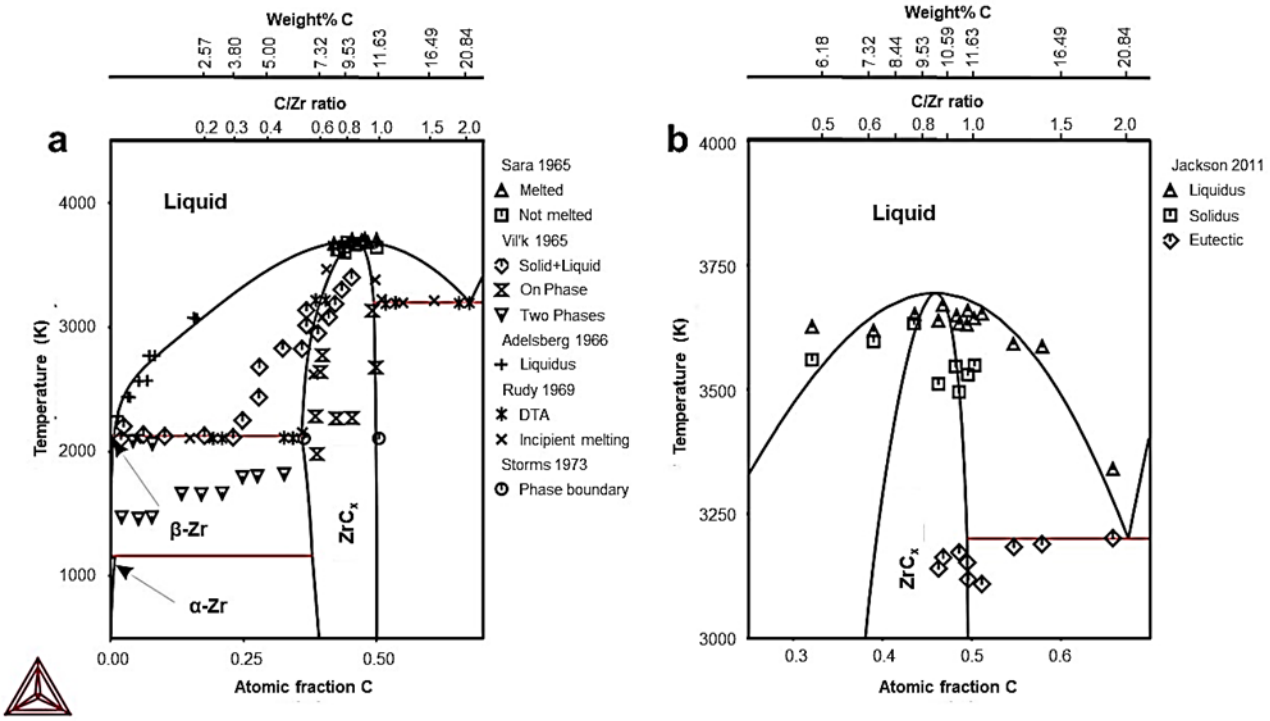

Figure 2.2: **Zr-C phase diagram calculated from Guillermet's optimized parameters with (a) some experimental data from Sara (1965), Vil'k *et al.* (1965), Adelsberg *et al.* (1966), Rudy (1969) and Storms (1973) and (b) experimental data from Jackson *et al.* (2011) according to Réjasse *et al.* (2016).**

A single intermediate compound exists as fcc ZrC_x ($0.55 \leq x \leq 0.98$; in the middle of Figure 2.2) with a wide phase field exhibiting only carbon deficient non-stoichiometric compositions and melting congruently at 3427 °C at a composition of approximately $ZrC_{0.85}$ (or 46 at. % carbon)

(Katoh *et al.*, 2013, Jackson *et al.*, 2010). The actual composition range, is still not clear (Katoh *et al.*, 2013), but it is suggested to be between $ZrC_{0.55}$ and $ZrC_{0.98}$ (Storms, 1967).

On the right-hand side of the fcc ZrC_x; $0.55 \leq x \leq 0.98$ (Figure 2.2), an eutectic occurs between ZrC and C at 2927 °C (2882 °C according to Manara *et al.* (2013)) at a carbon content of approximately 67 at. % carbon in the system with ZrC_x + C as end members (Katoh *et al.*, 2013).

While on the left-hand side of the fcc ZrC_x; $0.55 \leq x \leq 0.98$ (Figure 2.2), hcp Zr (α-Zr) and fcc ZrC_x ($x \leq 0.60$) occurs at equilibrium at a carbon content of between 0 and 0.39 at. % C. As the temperature increases to temperatures above 848 – 886 °C, the hcp Zr undergoes phase change to bcc Zr (β-Zr) phase. The fcc ZrC_x ($x \leq 0.55$) is then in equilibrium with the β-Zr until the temperature reaches a temperature of between 1807 and 1860 °C[b], thereafter the fcc ZrC_x ($0.55 \leq x \leq 0.60$) exists in equilibrium with melted Zr until the congruent melting point of ZrC_x ($x = 0.85$).

2.2.3 Bonding nature of C-C, Zr-C and Zr-Zr bonds in ZrC

The atoms in the ZrC lattice are bound by ionic, covalent (C-Zr) and metallic (Zr-Zr) bonds (Storms, 1967). The relative electronegativity, established by Pauling (1960), is used to predict the nature of the bond that will form. When the electronegativity of the elements forming a bond are similar, covalent bonds will form, while a large difference in electronegativity (Δx) will lead to ionic bonds. However, the transition between covalent and ionic bonding is not clearly discernible, leading to most bonds having both covalent and ionic character (Barsoum, 2003).

Considering Pauling's electronegativity scale (Pauling, 1960), carbon has an electronegativity value of 2.55 (due to the increased ability to attract electron density arising from poor electron shielding of its nucleus), while the electronegativity of zirconium is 1.33. This leads to a difference in electronegativity between the carbon and zirconium atoms of 1.22, causing bonds of ionic character to form (Harrison and Lee, 2016). In spite of the considerable charge transfer of approximately 0.42 e/pair from the zirconium to the carbon atom, the contribution of covalent

[b] The variation in temperature of the alpha-beta transition temperature is ascribed to the presence of dissolved oxygen (which increases the alpha-beta transition temperature) and the presence of carbon (which reduces the alpha-beta transition temperature) (Katoh *et al.*, 2013). Storms (1967) accordingly, suggests the use of the lower temperature as a more reliable value.

bonding is significantly higher (Katoh *et al.*, 2013), because the electronegativity difference is smaller than 1.7[c] and the Zr-C bond can thus be defined as polar covalent (Barsoum, 2003).

The electronic configurations of carbon and zirconium are $[He]2s^2 2p^2$ and $[Kr]5s^2 4d^2$ respectively (Barsoum, 2003). The overlap between the 2p orbitals of carbon and the 4d orbitals of zirconium result in covalent and metallic bonding (overlapping d orbitals of neighbouring Zr atoms) (Harrison and Lee, 2016, Storms, 1967). Metallic bonding also arises when the atoms are ionised; the electrostatic attraction between the positive metal ions located in the lattice and the delocalised electrons that can move freely throughout the lattice gives rise to the bonds (Harrison and Lee, 2016). ZrC has good electrical and thermal conductivity (close to that of zirconium metal), due to the metallic bonds in the lattice.

The metal-to-carbon bond is stronger than the metal-to-metal bonds (Yang *et al.*, 2015), as illustrated by their bond lengths and charge densities listed in Table 2.1. Like most transition metal carbides, ZrC is polar covalent (Katoh *et al.*, 2013) with a bond energy of 5.812 eV for the C-Zr bond. This strong covalent bonding is often cited as the main reason for the characteristic thermal and mechanical properties of ZrC (Katoh *et al.*, 2013).

Table 2.1: The bond energies, bond lengths and charge densities at bond points along the nearest bonds of C-C, Zr-C and Zr-Zr bonds of ZrC

Bonds	Bond Type	Bond Energy (eV)	Bond Length (nm)	Charge Density (e/au^3)
C-C	Covalent	6.288	0.3340	0.0226
C-Zr	Ionic-covalent	5.812	0.2209	0.0412
Zr-Zr	Metallic	-	0.3340	0.0218

(Katoh *et al.*, 2013, Yang *et al.*, 2015)

2.3 Mechanical and thermal properties

A material's resistance to local plastic deformation is represented by its indentation hardness. Brittle materials often form microcracks as a consequence of hardness that may affect the hardness value due to crack propagation rather than plastic deformation resistance influenced by dislocation evolutions in ductile materials. The hardness of metal carbides is related to the

[c] As a rough guide, bonds are predominantly considered as covalent when $\Delta x < 1.7$ and predominantly ionic if $\Delta x > 1.7$ (Barsoum, 2003, Atkins et al., 2006).

strong hybrid ionic-covalent bonds (rather than the weaker metallic Zr-Zr bonds) present in the carbide structure. The ionic-covalent Zr-C bonds in ZrC tend to prevent plastic deformation, resulting in brittle failure when a load is applied. Imperfections, such as crystal defects which develop during manufacturing of samples, influence the hardness of the material leading to a decrease in the resistance to failure. The Vickers hardness of near-stoichiometric ZrC is reported to be 27 to 35 GPa at 20 °C (Katoh *et al.*, 2013). An extensive study on the variation of hardness with varying stoichiometry has not yet been carried out.

The Young's modulus is determined for ZrC with a C/Zr ratio between 0.77 and 0.96 in the temperature range of 27 to 2027 °C and measured using the sonic resonance technique. When the C/Zr ratio is above 0.95, the Young's modulus starts to decrease due to excess carbon present in the sample according to Katoh *et al.* (2013). This is due to the presence of the carbon secondary phase in ZrC_x samples with $x \geq 1$. The Poisson's ratio at 27 °C increases from 0.21 to 0.23 with increasing C/Zr ratio of 0.77 to 0.96 (Katoh *et al.*, 2013). Using the calculated Young's modulus and Poisson's ratio at room temperature the shear modulus for stoichiometric ZrC is 167 GPa. It is thought (Katoh *et al.*, 2013), that this data must however be corrected for porosity and no correlation between temperature and C/Zr ratio has been established.

Data on the fracture toughness of ZrC is limited. Katoh *et al.* (2013) report that the fracture toughness of $ZrC_{0.93}$ is 1.40 MPa $m^{1/2}$ as determined by the Evans-Charles method, but when the toughness is measured according to the Chevron-notched beam flexure test, the value is 2.74 MPa $m^{1/2}$. The fracture strength of brittle ceramics is determined by the intrinsic fracture toughness and the flaw governing the fracture initiation. The manufacturing history of the sample (synthesis method, process conditions and test sample preparation), seem to have an important effect on the determination of the fracture strength (Katoh *et al.*, 2013). When the sample is porous or grain growth occurs during heat treatment, fracture strength decreases (Katoh *et al.*, 2013, Lanin *et al.*, 1991).

Thermal creep affects the failure criteria for nuclear materials such as SiC and ZrC. Stress developed due to fission product gases and other volatile fission product formation as well as CO_2 formed during oxidation of ZrC, can cause creep that can result in stress rupture. In this regard the microstructure of the ceramic material can play an important role in containment of the products in the nuclear fuel. According to Katoh *et al.* (2013) grain-growth of sub-stoichiometric ZrC during heat treatment can lead to thermal creep deformation, whereas stoichiometric and carbon-rich ZrC will retard this deformation due to the graphitic second phase in the ZrC compounds. Investigations of the thermal behaviour of $ZrC_{0.94}$ reported plastic

deformation at temperatures above 1197 °C and creep that occurs in the temperature range of 1400 to 2600 °C under a stress range of 2 to 70 MPa (Darolia and Archbold, 1976, Katoh *et al.*, 2013).

Katoh *et al.* (2013) report a number of thermal expansion values for a wide range of stoichiometric variations of ZrC, but the influence of the stoichiometry on the thermal expansion remains unclear. The thermal expansion coefficient may increase with increasing carbon vacancies and decrease when the vacancies are occupied with impurities. Table 2.2 presents a summary of the available data from Katoh *et al.* (2013) on the mechanical and thermal properties of ZrC as a function of the C/Zr ratio.

Table 2.2: Mechanical and thermal properties of ZrC

Property	Value	C/Zr ratio
Young's modulus (GPa)	350 – 440	0.77 – 0.96
Poisson's ratio	0.21 – 0.23	0.77 – 0.96
Shear modulus (GPa)	167	1.0
Vickers hardness (GPa)	27 – 35	~1.0
Fracture toughness (MPa $m^{1/2}$)	1.40 – 2.74	0.93
Thermal creep (K)	1470	0.94
Thermal expansion (x 10^{-6}/K)	6.7 – 7.6	0.72 – 0.94

Considering the data in Table 2.2, the optimum ZrC to be used for the coating of fuel rods, should have fracture toughness close to 1.40 MPa $m^{1/2}$ and Vickers hardness close or less than 27 GPa for the use in coatings or the values of these properties may be far less if manipulation of the ZrC structure through variation of the composition can be employed. The aim of the study sets out to find these values, but the best synthesis method of ZrC must first be determined.

2.4 Concluding remarks

A brief overview of some of the properties of zirconium carbide is given in this chapter. The crystal structure and lattice parameters as well as the mechanical and thermal properties of ZrC, as a function of the stoichiometry of ZrC, are presented and summarised. Discussing the mechanical and thermal properties, it is found that the stoichiometry of ZrC greatly influences

these parameters as well as the crystal structure and lattice parameters. The review found that a thorough understanding of the thermodynamic, mechanical and heat transport properties of ZrC is limited and that a careful and systematic detailed characterization of ZrC, as a function of stoichiometry, with emphasis on resulting microstructures, is required.

2.5 References

ADELSBERG, L.M., CADOFF, L.H. and TOBIN, J.M. 1966. Kinetics of the zirconium-carbon reaction at temperatures above 2000 °C. *Transactions of Metallurgical Society of AIME,* 236**,** 972-977.

ATKINS, P., OVERTON, T., ROURKE, J., WELLER, M. and ARMSTRONG, F. 2006. *Shriver & Atkins inorganic chemistry, 4th Ed,* New York, Oxford University Press; W.H. Freeman and Co.

BARSOUM, M. 2003. *Fundamentals of ceramics,* Bristol and Philadelphia, Institute of Physics Publishing.

CHINTHAKA SILVA, G.W., KERCHER, A.A., HUNN, J.D., MARTIN, R.C., JELLISON, G.E. and MEYER, H.M. 2012. Characterization of zirconium carbides using electron microscopy, optical anisotropy, Auger depth profiles, X-ray diffraction, and electron density calculated by charge flipping method. *Journal of Solid State Chemistry,* 194**,** 91-99.

DAROLIA, R. and ARCHBOLD, T.F. 1976. Plastic deformation of polycrystalline zirconium carbide. *Journal of Materials Science,* 11**,** 283-290.

GUILLERMET, A.F. 1995. Analysis of thermochemical properties and phase stability in the zirconium-carbon system. *Journal of Alloys and Compounds,* 217**,** 69-89.

HARRISON, R.W. and LEE, W.E. 2016. Processing and properties of ZrC, ZrN and ZrCN ceramics: a review. *Advances in Applied Ceramics,* 115**,** 294-307.

JACKSON, H.F., JAYASEELAN, D.D., LEE, W.E., REECE, M.J., INAM, F., MANARA, D., PERINETTI CASONI, C., DE BRUYCKER, F. and BOBORIDIS, K. 2010. Laser melting of spark plasma-sintered zirconium carbide: Thermophysical properties of a generation IV very high-temperature reactor material. *International Journal of Applied Ceramic Technology,* 7**,** 316-326.

JACKSON, H.F., JAYASEELAN, D.D., MANARA, D., PERINETTI CASONI, C. and LEE, W.E. 2011. Laser Melting of Zirconium Carbide: Determination of Phase Transitions in Refractory Ceramic Systems. *Journal of the American Ceramic Society,* 94**,** 3561-3569.

KATOH, Y., VASUDEVAMURTHY, G., NOZAWA, T. and SNEAD, L.L. 2013. Properties of zirconium carbide for nuclear fuel applications. *Journal of Nuclear Materials,* 441**,** 718-742.

LANIN, A.G., MARCHEV, E.V. and PRITCHIN, S.A. 1991. Non-isothermal sintering parameters and their influence on the structure and properties of zirconium carbide. *Ceramics International,* 17**,** 301-307.

MANARA, D., JACKSON, H.F., PERINETTI-CASONI, C., BOBORIDIS, K., WELLAND, M.J., LUZZI, L., OSSI, P.M. and LEE, W.E. 2013. The ZrC–C eutectic structure and melting behaviour: A high-temperature radiance spectroscopy study. *Journal of the European Ceramic Society,* 33**,** 1349-1361.

PAULING, L. 1960. *The Nature of the Chemical Bond*, Cornell university press Ithaca, NY.

PREISS, H., SCHIERHORN, E. and BRZEZINKA, K.-W. 1998. Synthesis of polymeric titanium and zirconium precursors and preparation of carbide fibres and films. *Journal of Materials Science,* 33**,** 4697-4706.

RÉJASSE, F., RAPAUD, O., TROLLIARD, G., MASSON, O. and MAÎTRE, A. 2016. Experimental investigation and thermodynamic evaluation of the C–O–Zr ternary system. *RSC Advances,* 6**,** 100122-100135.

RUDY, E. 1969. Ternary phase equilibria in transition metal-boron-carbon-silicon systems. part 5. compendium of phase diagram data. Air Force Materials Laboratory, Wright-Patterson AFB**,** 165-167.

SARA, R.V. 1965. The System Zirconium-Carbon. *Journal of the American Ceramic Society,* 48**,** 243-247.

STORMS, E.K. 1967. *The Refractory Carbides,* New York, Academic Press.

STORM, E.K. and GRIFFIN, J. 1973. Vaporization behavior of the defect carbides. IV. The zirconium-carbon system. *High temperature science,* 5**,** 291-310.

VIL'K, Y.N., ORDAN'YAN, S.S., AVARBE, R.G., AVGUSTINIK, A.I., RYZHKOVA, T.P. and OMEL'CHENKO, Y.A. 1965. *Journal of applied chemistry of the USSR,* 38**,** 1472-1476.

YANG, X.-Y., LU, Y., ZHENG, F.-W. and ZHANG, P. 2015. Mechanical, electronic, and thermodynamic properties of zirconium carbide from first-principles calculations. *Chinese Physics B,* 24**,** 116301-116306.

CHAPTER 3 PROCESSING METHODOLOGIES OF ZIRCONIUM CARBIDE

3.1 Introduction

Processing of ZrC is achieved through a number of different techniques. Reactions in the solid phase through carbothermic reduction, from solution based precursors and from the vapour phase, are used to synthesise ZrC. Samples prepared using the different synthesis techniques have varying characteristics, microstructure, chemical composition, purity and concentrations (Katoh *et al.*, 2013). Katoh *et al.* (2013) consequently declares that it is thus important to evaluate the characteristics of ZrC synthesized by a specific synthesis technique as it will affect the material properties. Factors that need to be considered during evaluation are: the stoichiometry of ZrC_x, chemical purity in terms of oxygen and nitrogen contamination, grain size, texture, morphology, porosity and the presence of secondary phases such as ZrO_2 (Katoh *et al.*, 2013).

Factors for this study that should also be considered during the choice of synthesis method are: availability of equipment needed (such as furnaces and mills), type of reagents used including the handling of said reagents (such as zirconium halides or zirconium alkoxides) and similar research projects running at the same time of this study.

In this chapter the synthesis of ZrC will be discussed to identify the most suitable synthesis route to effectively control the stoichiometry.

3.2 Synthesis of ZrC using solid phase reactions

3.2.1 Carbothermal reduction synthesis

Carbothermal reduction, or the reduction of zirconia (ZrO_2) with carbon (Equation 3.1), is an inexpensive and simple operation. This processing method is the most common method used for fabricating bulk ZrC on a commercial level. The process is highly endothermic and thus intensive in terms of temperatures (1800 – 2600 °C) and process time (16 – 24 h), and often requires repeated heating cycles (Katoh *et al.*, 2013, Maitre and Lefort, 1997) with the sample purity only ensured until near-melting conditions are reached, that may further result in sub-stiochiometric phases in graphitic carbon matrices.

$$ZrO_2(s) + 3C(s) \rightarrow ZrC(s) + 2CO(g) \quad (3.1)$$

For the carbothermic reduction processing of ZrC, the degree of mixing at the microscale and surface chemistry of the reacting powders, affect the degree of carbonization (Katoh *et al.*, 2013) of the sintered end product. The carbothermal reduction reaction needs to be carried out in vacuum or under inert gas to ensure the purity of the final product. The rate of the reaction becomes dependant on the partial pressure of the carbon monoxide gas evolved from the reaction.

3.2.2 Self-propagating high temperature synthesis

Self-propagating high temperature synthesis (SHS) is used to prepare phase pure ceramics and intermetallic compounds by exothermic reactions in the reactant mixture. This method is simple, requires only the ignitor energy, has short processing times (seconds) and reaches temperatures of above 4500 °C (Mallick *et al.*, 2016).

It is reported (Katoh *et al.*, 2013, Jain, 2004) that the fabrication of ZrC by direct combination of pure zirconium or zirconium hydride powder with carbon, where the reactant mixture is pressed to form a green body which is then heated to an ignition temperature, gives rise to an exothermic reaction - the heat released by the reaction being sufficient to sustain and drive the reaction to completion (instead of a diffusion dependant reaction as in the carbothermic reaction). In this method the product purity also strongly depends on the degree of microscale mixing, the specific surfaces of the reactant particles, the initial green body density and the applied external pressure. Moreover, it is noted by Katoh *et al.* (2013) that because the combustion reaction is highly energetic and rapid, an explosion and hence a collapse of the green body, can take place in cases where the reactants are not confined by means of external pressure – a requirement that might impede the adaption of this process to coating of fuel rods. Furthermore, it is thought that controlling the exact product stoichiometry in this method to the size of standard fuel rods will be a challenge.

3.2.3 Reduction by addition of reductants

Many researchers have been using SHS to fabricate ZrC. Song *et al.* (2008) synthesized ZrC by ball milling Zr, C and Al powders together. The reaction was slow although the synthesis temperature was raised to almost 2000 °C and the final product contained impurity phases of Al and $ZrAl_3$. Zhang *et al.* (2011) similarly used copper instead of aluminium and found that the

very low dissolubility of carbon into melted copper may inhibit the growth of the ZrC particles, resulting in formation of nano-sized particles.

3.2.4 Solid State Metathesis

Nartowski *et al.* (1999) synthesized ZrC *via* Solid State Metathesis (SSM). During SSM a zirconium halide (such as $ZrCl_4$) and metallic zirconium are reacted with a metal carbide (such as Al_4C_3 or CaC_2). The carbon and zirconium sources are ground together and heated in a sealed evacuated container. Equation 3.3 and Equation 3.4 represent the chemical reactions involved in SSM using Al_4C_3 and CaC_2 as carbon sources:

$$3ZrCl_4(s) + Al_4C_3(s)\ (1000\ °C) \rightarrow 3ZrC(s) + 4AlCl_3(s) \quad (3.3)$$

$$ZrCl_4(s) + 2CaC_2(s)\ (500\ °C) \rightarrow ZrC(s) + 2CaCl_2(s) + 3C(s) \quad (3.4)$$

The $AlCl_3$ can be removed by sublimation, while the $CaCl_2$ can be removed by dissolution in methanol and water.

Davoodi *et al.* (2015) synthesized nano-sized ZrC by magnesiothermic reduction. Magnesiothermic reduction relies on the reduction of ZrO_2 with Mg metal and the resulting Zr to react with the carbon present in the reaction mixture. The typical reaction equation is given in Equation 3.5:

$$ZrO_2(s) + 2Mg(s) + C(s) \rightarrow ZrC(s) + 2MgO \quad (3.5)$$

3.3 Preparation of ZrC *via* reactions in the vapour phase

Vapour phase synthesis of ZrC is carried out employing techniques such as vapour phase deposition (CVD), magnetron sputtering and pulse laser deposition (Meng *et al.*, 2013). During the CVD technique a zirconium halide (usually $ZrCl_4$) is reacted with a hydrocarbon (usually methane) in the gas phase at relatively low temperatures (1300 – 1500 °C). Equation 3.6 represents a simplified reaction equation for this process:

$$ZrX_4(g) + xCH_4(g) + 2(1-x)H_2(g) \rightarrow ZrC_x(s) + 4HX(g) \quad (X = Cl, Br, I;\ x \leq 1) \quad (3.6)$$

The zirconium halide can be used as is or it can be synthesized *in situ* using the halide process. Ogawa *et al.* (1979) developed the halide process where they (*op crit.*) synthesize zirconium

halide by reacting the halide (mostly bromide) with zirconium sponge at temperatures between 400 and 600 °C, using a carrier gas to transport the so-formed zirconium halide to mix with the carbon source and reach the substrate.

It is claimed that the stoichiometry of the resulting ZrC_x can be controlled by varying the concentrations of the $ZrCl_4$ and the hydrocarbon gas in the reaction mixture. This method has been successfully applied to coating of tristructural isotropic (TRISO) spherical fuel particles using a fluidized bed process. However, it is thought that this process needs to be further developed in order to be used for the application of a ZrC coating to fuel rod cladding with dimensions orders of magnitude larger than those of UO_3 fuel kernels.

3.4 Synthesis of ZrC using solution-based processes

Synthesis of ZrC can also be achieved *via* solution-based processes. This technique involves the mixing of a soluble organo-zirconium compound and a polymeric carbon source together in a solvent (usually ethanol) to form a sol or a gel. Carbothermal reduction of the formed gel affords ZrC (Preiss *et al.*, 1998, Sacks *et al.*, 2004, Yan *et al.*, 2007, Yan *et al.*, 2013, Zhao *et al.*, 2010). This technique mixes the reactants at a molecular level, which can lead to shorter reaction times for carbothermal reduction compared to solid state mixing and reduction.

3.4.1 Sol-gel process

The sol-gel process is traditionally referred to as the hydrolysis and condensation of metal alkoxide-based precursors to synthesize metal oxides. Synthesis of carbides using sol-gel processing follows the same fundamental principles as presented in Appendix B, but carbide synthesis must be carried out in an inert atmosphere and by addition of a carbon source to avoid metal oxide formation.

Zirconium alkoxides such as zirconium n-propoxide ($Zr(OC_3H_7)_4$) (Sacks *et al.*, 2004, Ang *et al.*, 2013) and zirconium n-butoxide ($Zr(OC_4H_9)_4$) (Zhao *et al.*, 2010) are commonly used as zirconium sources during the solution-based synthesis of ZrC. Due to the high reactivity of zirconium alkoxides with water, the metal alkoxides need to be modified with acetic acid, acetylacetone or ethyl acetoacetate to reduce the reactivity with water (Preiss *et al.*, 1998, Dollé *et al.*, 2007). The modification process uses specialized glassware and an inert atmosphere to convert the alkoxide into a compound with reduced reactivity towards water. Zirconium oxychloride octahydrate ($ZrOCl_2.8H_2O$, commonly abbreviated as ZOC) (Yan *et al.*, 2007, Yan

et al., 2013, Li *et al.*, 2014) and zirconium 2,4-pentanedionate ($Zr(O_2C_5H_7)_4$) (Jain, 2004, Katoh *et al.*, 2013) can be used as an alternative to zirconium alkoxides.

The following tables (Table 3.1 and Table 3.2) summarize the synthesis of ZrC using solution-based techniques and also list some of the qualities of the produced ZrC with such a method. Yan *et al.* (2007) prepared ZrC powder using ZOC as zirconium source and phenolic resin as carbon source. Pyrolysis of the dried gel in a graphite furnace at various temperatures from 1200 °C up to 1400 °C yielded ZrC powders with different stoichiometries. Dong *et al.* (2015) converted $ZrCl_4$ to zirconium ethoxide ($Zr(OC_2H_5)_4$) and added acetylacetone as chemical modifier and phenol as carbon source. After pyrolysis in an alumina tube furnace at various temperatures, ZrC powders with varying purity were obtained. Ang *et al.* (2013) synthesized fine ZrC powder (< 100 nm) from zirconium n-propoxide ($Zr(OC_3H_7)_4$) and furfuryl alcohol with the assistance of a polymer surfactant to homogeneously mix the reaction mixture. Nanocrystalline ZrC was prepared by Dollé *et al.* (2007) from $Zr(OC_3H_7)_4$, acetic acid as chemical modifier and sucrose as carbon source. The ZrC phase was observed in the XRD pattern of a sample prepared at 1200 °C, but the sample still contained a high amount of oxygen and with further heat treatment at higher temperatures (up to 1800 °C) the oxygen could be substantially removed from the ZrC powders.

Yan *et al.* (2015) demonstrated the synthesis of ZrC powders *via* the Pechini method through the use of ZOC as zirconium source, citric acid as a chelate ligand and ethylene glycol as a cross-linker. This was shown to provide a simple and benign method for precursor preparation *via* the formation of an *in situ* polymerizable complex. Homogeneous nanostructured carbides, inclusive of ZrC, were produced after reaction at 1300 °C.

Although it is claimed that the disadvantage of the sol-gel method is the presence of residual oxygen as an impurity in the ZrC product (Jain, 2004) (which has been found to contribute to non-stiochiometry *op cit*.), it is thought that this *disadvantage* may provide the mechanism to control the process of formation of non-stoichiometric variants – of importance to the subject of this study.

Table 3.1: ZrC processing methods and parameters with the composition of the ZrC expressed as weight percentages of Zr, C and O

				Product quality				
				Lattice parameter (nm)	Composition (wt. %)			
Ref #	**Zr source**	**C source**	**Processing parameters**		**Zr**	**C**	**O**	**Stoichiometry***
(Sacks *et al.*, 2004)	$Zr(OC_3H_7)_4$, acetylacetone	Glycerol ($C_3H_8O_3$), Phenol-formaldehyde (novolac resin)	1200 – 1800 °C, 2h	1475 °C: 0.4691 1800 °C: 0.4696		13.4	3.3	$ZrC_{1.22}O_{0.23}$
(Yan *et al.*, 2007)	ZOC	Phenolic resin	Graphite furnace, 1100 – 1400 °C, 10 °C/min, 1h	1200 °C: 0.4680 1300 °C: 0.4690 1400 °C: 0.4693	70.13 68.81 87.54	8.52 12.88 10.68	20.03 8.14 0.66	$ZrC_{0.92}O_{1.65}$ $ZrC_{1.42}O_{0.67}$ $ZrC_{0.93}O_{0.04}$
(Dong *et al.*, 2015)	$ZrCl_4$ (converted to $Zr(OC_2H_5)_4$)	Phenol Acetylacetone	Alumina tube furnace, 300 – 1600 °C, 10 °C/min, 1h	1200 °C: n/a 1300 °C: n/a 1400 °C: n/a 1500 °C: n/a 1600 °C: n/a	57.92 63.72 69.81 76.28 87.05	21.24 19.32 18.39 16.01 12.34	20.84 16.96 11.81 7.71 0.61	 $ZrC_{1.08}O_{0.04}$
(Chu *et al.*, 2013)	$Zr(NO_3)_4.5H_2O$	Glucose Urea	Graphite furnace, 1200 – 1600 °C, 10 °C/min, 3h	1500 °C: 0.4692 1600 °C: 0.4692		12.9 12.7	1.4 1.1	$ZrC_{1.14}O_{0.09}$ $ZrC_{1.12}O_{0.07}$

* Calculated stoichiometry based on the weight percentage of C and O

Table 3.2: ZrC synthesis parameters with the purity of the ZrC expressed as oxygen content

				Product quality		
Ref #	**Zr source**	**C source**	**Processing parameters**	**Lattice parameter (nm)**	**Oxygen content**	**Stoichiometry***
(Yan *et al.*, 2012a)	ZOC, acetylacetone	Phenolic resin	Graphite furnace, 1200 – 1600 °C, 2h		Trace oxygen (2.5 at. %)	$ZrC_{0.98}O_{0.02}$
(Yan *et al.*, 2013)	ZOC	Chitosan	Graphite furnace, 1200 – 1550 °C, 2h		Trace oxygen (3.0 at. %)	$ZrC_{0.97}O_{0.03}$
(Ang *et al.*, 2013)	$Zr(OC_3H_7)_4$, acetylacetone	Furfuryl alcohol	Tube furnace, up to 1450 °C, 2h	0.4695	Some oxygen observed, not quantified	
(Dollé *et al.*, 2007)	$Zr(OC_3H_7)_4$	Acetic acid Sucrose	Graphite furnace, 1400 – 1800 °C, 20 °C/min, 3h	1400 °C: 0.4690 1500 °C: 0.4694 1600 °C: 0.4695 1400 °C (150 min), 1800 °C (6 min): 0.4697	Oxygen: 8 at. % Oxygen: 5 at. % Oxygen: 3 at. % Oxygen: 2 at. %	$ZrC_{0.92}O_{0.08}$ $ZrC_{0.95}O_{0.05}$ $ZrC_{0.97}O_{0.03}$ $ZrC_{0.98}O_{0.02}$
(Yan *et al.*, 2012b)	Zr-complexes from ZOC with acetyl acetone, ethylene glycol, salicylic acid or lactic acid	Phenolic resin	Graphite furnace, 1400 – 1550 °C, 8 °C/min, 2h	1500 °C: 0.4670 1550 °C: 0.4685	Trace oxygen (2.5 at. %)	$ZrC_{0.98}O_{0.02}$
(Yan *et al.*, 2015)	ZOC	Citric acid Ethylene glycol	Graphite furnace, 1000 – 1400 °C, 6 °C/min, 2h	1300 °C: 0.4688	Oxygen not reported	ZrC

* Stoichiometry based on the atomic percentage O

3.4.2 Pechini method

The Pechini method is named after its inventor, Maggio P. Pechini, who modified a sol-gel method in 1967, that could be used for the preparation of metals that are not suitable for the fundamental sol-gel type reactions as presented in Table 3.1 and Appendix B. The method was originally invented for the preparation of thin films of metal oxides in the electronics industry, focussing on niobates, titanates and zirconates for capacitor materials (Pechini and Adams, 1967, Kakihana and Yoshimura, 1999). This method has been extensively applied to synthesize a variety of multicomponent oxides, due to its suitability to form highly pure homogeneous oxides at reduced temperatures (Kakihana and Yoshimura, 1999).

The basic chemistry of the Pechini method shown in Figure 3.1, involves the formation of metal complexes and the esterification reaction of an alpha-hydroxycarboxylic acid and a polyhydroxy alcohol. Citric acid and ethylene glycol are mostly used as the α-hydroxycarboxylic acid and a polyhydroxy alcohol respectively. The metal cations chelate with the citric acid and undergo esterification with ethylene glycol upon heating, leading to a polyester with a homogeneous distribution of constituent metal ions throughout the polymer. The ability of citric acid to form stable chelates with a variety of metal ions can be attributed to citric acid being a polybasic compound with three carboxylic acid groups and one alcoholic group in one molecule. Citric acid thus has the ability to solubilize a wide range of metal ions in a mixture of water and ethylene glycol and prevent cations from easily hydrolysing and precipitating out of the solution in the presence of water. This is of use especially for systems containing titanium or zirconium complexes.

When a polyalcohol, such as ethylene glycol, is added to the metal citrate complexes, esterification and cross-linking occur, resulting in the gelation of the reaction mixture. The metal citrate complexes are immobilised in a rigid polyester network, which preserves the initial stoichiometric ratio of the metal ions during polymerisation. The principle of the Pechini method is thus to obtain a polymer with metal cations distributed homogeneously throughout the polymer network as illustrated in Figure 3.1. The reactions taking place during the synthesis of the precursor are metal chelate formation (metals A and B chelate with the O atoms of the carboxylic acid groups of the citric acid) and hydrolysis-condensation (esterification reaction of the citric acid and ethylene glycol).

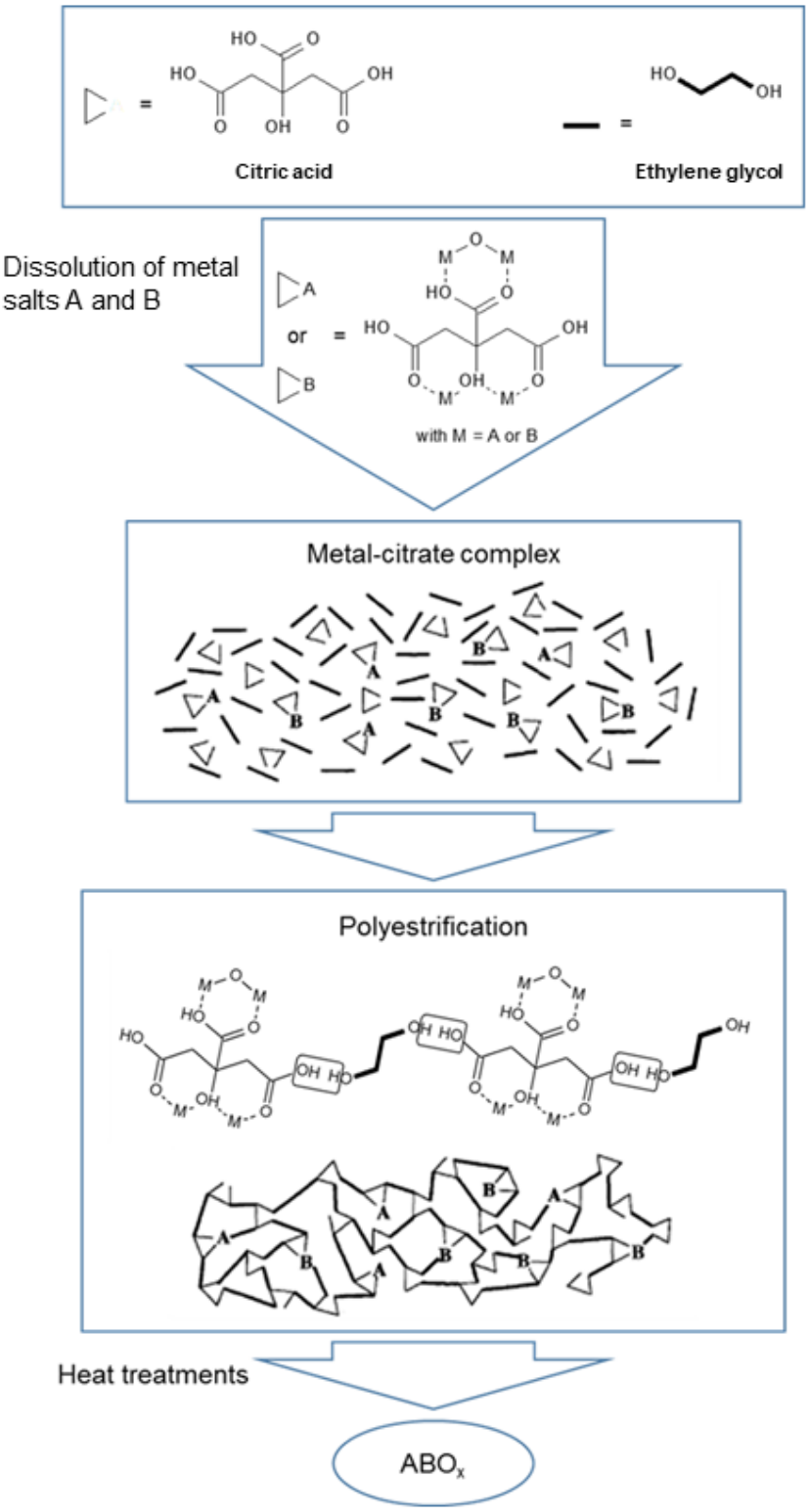

Figure 3.1: **The in-situ polymerisation of the Pechini method, after Kakihana and Yoshimura (1999)**

The Pechini method bypasses the requirement that the metals used must form suitable hydroxo complexes, by forming stable complexes of a variety of metals over a wide pH range. The water-soluble metal salts used during the synthesis of a Pechini-type sol are more readily available and easier to work with than metal alkoxides. The Pechini method has the advantage over other sol-gel techniques, to synthesize complicated multicomponent oxides with a homogeneous distribution of elements.

3.5 Concluding remarks

Considering the various synthesis routes to the formation of quality ZrC that can be used in the nuclear industry, the following conclusions could be made:

Although the solid state reaction route may be the largest commercial route to fabricate ZrC, the processing times and temperatures are not economical. The particles have a bigger chance to be contaminated with oxygen and possible contamination from the milling media used to create fine particles is also possible. Another drawback is that an additional processing method is needed to apply the ZrC powder to the fuel rods.

Vapour phase synthesis of ZrC through the CVD process does fabricate the purest phase ZrC, but the processing method uses complicated reagents and processing set-ups. The scale of a fuel rod is also orders of magnitude larger than the TRISO fuel kernels being coated *via* this process. (This process has recently been investigated by Biira *et al.* (2017).)

The literature shows solution-based synthesis routes to hold the greatest advantage regarding control of the stoichiometry. ZrC (with various stoichiometries) were achieved at temperatures ranging from 1200 °C to 1800 °C. In addition, the Pechini method is a simple and benign method for precursor preparation *via* the formation of an *in situ* polymerizable complex, *in situ* charring and *in situ* reaction at 1300 °C Table 3.2.

Considering the aim of this thesis, the Pechini method is chosen as synthesis technique to synthesize stoichiometric and non-stoichiometric ZrC powders.

3.6 References

ANG, C., WILLIAMS, T., SEEBER, A., WANG, H. and CHENG, Y.-B. 2013. Synthesis and Evolution of Zirconium Carbide *via* Sol–Gel Route: Features of Nanoparticle Oxide–Carbon Reactions. *Journal of the American Ceramic Society,* 96**,** 1099-1106.

BIIRA, S., CROUSE, P.L., BISSETT, H., HLATSHWAYO, T.T., VAN LAAR, J.H. and MALHERBE, J.B. 2017. Design and fabrication of a chemical vapour deposition system with special reference to ZrC layer growth characteristics. *Journal of the Southern African Institute of Mining and Metallurgy,* 117**,** 931-938.

CHU, A., QIN, M., RAFI UD, D., ZHANG, L., LU, H., JIA, B. and QU, X. 2013. Carbothermal synthesis of ZrC powders using a combustion synthesis precursor. *International Journal of Refractory Metals and Hard Materials,* 36**,** 204-210.

DAVOODI, D., HASSANZADEH-TABRIZI, S., EMAMI, A.H. and SALAHSHOUR, S. 2015. A low temperature mechanochemical synthesis of nanostructured ZrC powder by a magnesiothermic reaction. *Ceramics International,* 41**,** 8397-8401.

DOLLÉ, M., GOSSET, D., BOGICEVIC, C., KAROLAK, F., SIMEONE, D. and BALDINOZZI, G. 2007. Synthesis of nanosized zirconium carbide by a sol–gel route. *Journal of the European Ceramic Society,* 27**,** 2061-2067.

DONG, Z., ZHANG, X., HUANG, Q., ZHANG, J., ZUO, X., LI, W., YUAN, G. and LI, X. 2015. Synthesis and pyrolysis behavior of a soluble polymer precursor for ultra-fine zirconium carbide powders. *Ceramics International,* 41**,** 7359-7365.

JAIN, A. 2004. *Synthesis and processing of nanocrystalline zirconium carbide formed by carbothermal reduction.* Master of Science Thesis, Georgia Institute of Technology.

KAKIHANA, M. and YOSHIMURA, M. 1999. Synthesis and characteristics of complex multicomponent oxides prepared by polymer complex method. *Bulletin of the Chemical Society of Japan,* 72**,** 1427-1443.

KATOH, Y., VASUDEVAMURTHY, G., NOZAWA, T. and SNEAD, L.L. 2013. Properties of zirconium carbide for nuclear fuel applications. *Journal of Nuclear Materials,* 441**,** 718-742.

LI, F., KANG, Z., HUANG, X., WANG, X.-G. and ZHANG, G.-J. 2014. Preparation of zirconium carbide foam by direct foaming method. *Journal of the European Ceramic Society,* 34**,** 3513-3520.

MAITRE, A. and LEFORT, P. 1997. Solid state reaction of zirconia with carbon. *Solid State Ionics,* 104**,** 109-122.

MALLICK, A., CHAKRABORTY, S. and DAS, P.K. 2016. Synthesis and consolidation of ZrC based ceramics: a review. *Reviews on Advanced Materials Science,* 44**,** 109-133.

MENG, Q.N., WEN, M., MAO, F., NEDFORS, N., JANSSON, U. and ZHENG, W.T. 2013. Deposition and characterization of reactive magnetron sputtered zirconium carbide films. *Surface & Coatings Technology,* 232**,** 876-883.

NARTOWSKI, A., PARKIN, I. and CRAVEN, A. 1999. Solid state metathesis routes to transition metal carbides. *Journal of Materials Chemistry,* 9**,** 1275-1281.

OGAWA, T., IKAWA, K. and IWAMOTO, K. 1979. Effect of gas composition on the deposition of ZrC-C mixtures: The bromide process. *Journal of Materials Science,* 14**,** 125-132.

PECHINI, M. and ADAMS, N. 1967. Method of preparing lead and alkaline earth titanates and niobates and coating method using the same to form a capacitor. US Patent 3330697.

PREISS, H., SCHIERHORN, E. and BRZEZINKA, K.-W. 1998. Synthesis of polymeric titanium and zirconium precursors and preparation of carbide fibres and films. *Journal of Materials Science,* 33**,** 4697-4706.

SACKS, M.D., WANG, C.-A., YANG, Z. and JAIN, A. 2004. Carbothermal reduction synthesis of nanocrystalline zirconium carbide and hafnium carbide powders using solution-derived precursors. *Journal of Materials Science,* 39**,** 6057-6066.

SONG, M., HUANG, B., ZHANG, M. and LI, J. 2008. Reaction Synthesis of Nano-scale ZrC Particulates by Self-propagating High-temperature Synthesis from Al–Zr–C Powder Mixtures. *ISIJ International,* 48**,** 1026-1029.

YAN, C., LIU, R., CAO, Y., ZHANG, C. and ZHANG, D. 2012a. Carbothermal Synthesis of Submicrometer Zirconium Carbide from Polyzirconoxane and Phenolic Resin by the Facile One-Pot Reaction. *Journal of the American Ceramic Society,* 95**,** 3366-3369.

YAN, C., LIU, R., CAO, Y., ZHANG, C. and ZHANG, D. 2012b. Synthesis of submicrometer zirconium carbide formed from inorganic–organic hybrid precursor pyrolysis. *Journal of Sol-Gel Science and Technology,* 64**,** 251-256.

YAN, C., LIU, R., CAO, Y., ZHANG, C. and ZHANG, D. 2013. Synthesis of zirconium carbide powders using chitosan as carbon source. *Ceramics International,* 39**,** 3409-3412.

YAN, C., LIU, R., ZHANG, C. and CAO, Y. 2015. Zirconium carbide, hafnium carbide and their ternary carbide nanoparticles by an in situ polymerization route. *RSC Advances,* 5**,** 36520-36529.

YAN, Y., HUANG, Z., LIU, X. and JIANG, D. 2007. Carbothermal synthesis of ultra-fine zirconium carbide powders using inorganic precursors *via* sol–gel method. *Journal of Sol-Gel Science and Technology,* 44**,** 81-85.

ZHANG, M., HU, Q., HUANG, B., LI, J. and LI, J. 2011. In situ synthesis of nano-sized ZrC and its formation mechanism by combustion synthesis from Zr–C–Cu system. *ISIJ International,* 51**,** 1576-1579.

ZHAO, D., HU, H., ZHANG, C., ZHANG, Y. and WANG, J. 2010. A simple way to prepare precursors for zirconium carbide. *Journal of Materials Science,* 45**,** 6401-6405.

CHAPTER 4 SYNTHESIS OF ZIRCONIUM CARBIDE

4.1 Introduction

The Pechini method was used to prepare stoichiometric and non-stoichiometric ZrC powders. The variation of the stoichiometry of ZrC powders was investigated by varying the carbon content during the formation of ZrC powders. Carbothermal reduction reactions were carried out at various temperatures (1300 °C to 1500 °C) and the resulting powders were characterized by XRD analysis to identify the crystalline phases present. Analytical techniques were used to determine the stoichiometry of the ZrC powders with varying carbon content that were prepared.

4.2 Experimental

4.2.1 Synthesis Procedure

Batch type synthesis

The Pechini method (Pechini and Adams, 1967), modified by Yan *et al.* (2015), was used as the synthesis method: zirconium oxychloride octahydrate ($ZrOCl_2.8H_2O$; **ZOC**, 99.5%, Sigma Aldrich), ethylene glycol (**EG**, 99.8%, Sigma Aldrich) and citric acid monohydrate (**CA**, 99.9%, Sigma Aldrich) were dissolved in distilled water under stirring until a clear solution was obtained.

In order to achieve different stoichiometries, the molar ratio of CA to ZOC was varied between 0.25 to 1.0 and 1.0 to 1.0 in 0.25 increments of moles of CA, while the molar ratio of ZOC to EG was kept at 1.0:1.0. Table 4.1 lists the mass of CA and ZOC dissolved in 10 mL distilled water to form zirconium citrate complexes (as shown in step 1 of Figure 4.1); after the CA and ZOC were dissolved, 1.12 mL EG was added to each solution and the solutions stirred at room temperature for 10 min to form the polymeric precursor (sol). (Each batch type is named based on the molar ratio of CA to ZOC used to prepare each batch.)

Table 4.1: **Amounts of reagent used in a typical reaction in 10 mL water to obtain batch type S0.25, S0.50, S0,75 and S1.00**

Batch type*	Molar ratio CA:ZOC	Citric acid (CA) (g)	Ethylene glycol (EG) (mL)	Zirconium oxychloride (ZOC) (g)
S0.25	0.25:1.0	1.0507	1.12	6.4450
S0.50	0.50:1.0	2.1014	1.12	6.4450
S0.75	0.75:1.0	3.1521	1.12	6.4450
S1.00	1.00:1.0	4.2028	1.12	6.4450

** The batch type is based on the molar ratio of CA to ZOC used to prepare each batch.*

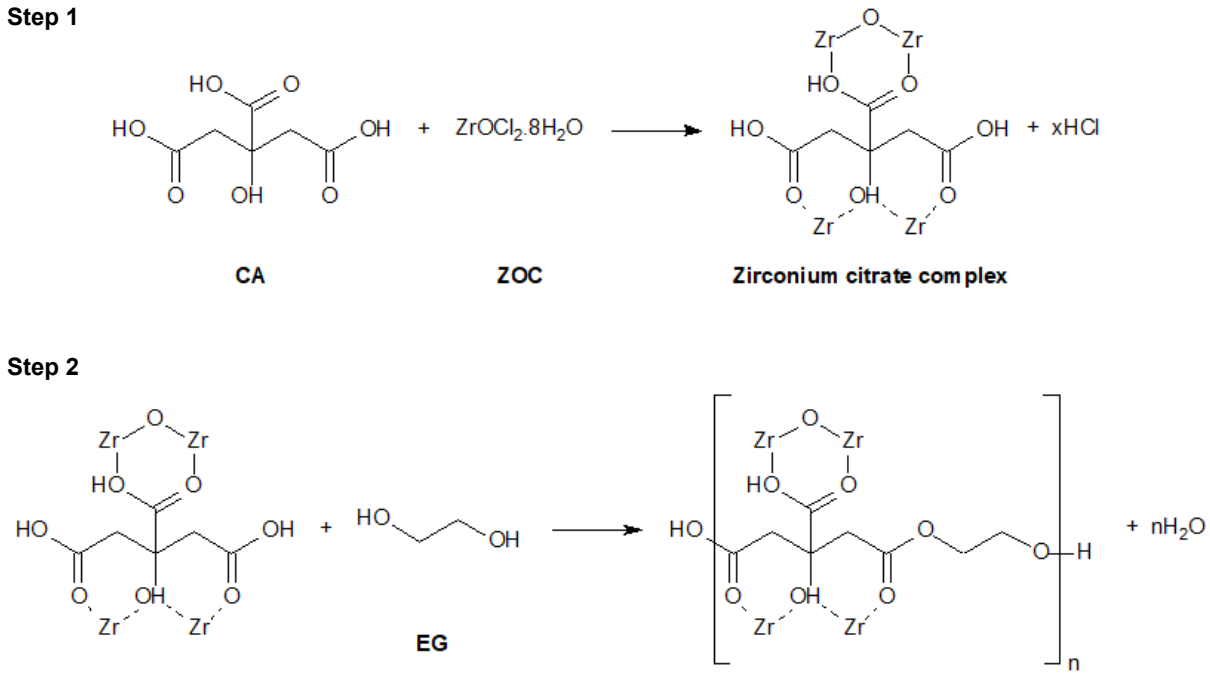

Figure 4.1: **Schematic of the formation of the polymeric precursor**

After stirring, the sols were transferred in 100 mL alumina crucibles and placed in a preheated furnace at 150 °C for heat treatment (6 hours). During heat treatment the polyesterification reactions are completed and due to the temperature used (i.e. 150 °C) the small molecules such as HCl and H_2O are thereby removed from the gels, *via* evaporation. The solvent (water)

is also removed during this heat treatment step to afford dried gels. The dried gels were left in the furnace (which was switched off after 6 hours) to cool to room temperature overnight[d].

Carbothermal reduction

The carbothermal reduction reaction was carried out as follows: A set of the dried gels (of S0.25, S0.50, S0.75 and S1.00, in alumina crucibles) were placed in a water-cooled, vacuum graphite sintering furnace (HGB Series, model HZA 2300-200) and the furnace was closed (or sealed). In order to remove the atmospheric oxygen in the reaction chamber of the furnace, vacuum was applied to the reaction chamber and followed by refilling the reaction chamber with argon. This "vacuum and argon refilling procedure" was repeated to ensure that the atmospheric oxygen was removed from the reaction chamber of the furnace. Thereafter, the reaction chamber of the furnace was kept under an argon atmosphere while being heated at 6 °C/min to a temperature of 1300 °C. When the temperature in the reaction chamber reached 1300 °C, the samples were kept at this temperature for 2 hours[e] and vacuum was applied to the reaction chamber, approaching a pressure of 600 Pa. (Due to off-gasses forming during the pyrolysis an absolute value for the applied vacuum could not be determined.) After 2 hours the applied vacuum on the reaction chamber was maintained while cooling the samples (S0.25-1300, S0.50-1300, S0.75-1300 and S1.00-1300) to room temperature.

The carbothermal reduction procedure was repeated using new batches (of S0.25, S0.50, S0.75 and S1.00) and pyrolysing the batches at 1400 °C and 1500 °C to obtain the samples listed in Table 4.2. The samples listed in Table 4.2 were characterized using X-ray powder diffraction (XRD) and Inert Gas Fusion analysis (IGF) and the results were used to determine the stoichiometry of each batch type after carbothermal reduction at 1300 °C, 1400 °C and 1500 °C.

Sample names are given according to the batch type used followed by the reaction temperature used to prepare each sample; for example, S1.00-1300 refers to a sample prepared from batch type S1.00 and pyrolysing the sample at 1300 °C.

---

[d] It was necessary to use dry gels in the furnace used for carbothermal reduction, as moisture causes damage to the graphite electrodes and lining of the furnace.

[e] Most solution-based synthesis experiments only pyrolyse the samples for 2 hours. Longer reaction times could not be used due to the water-cooling system of the furnace that could not be left to operate overnight (facility limitation).

Table 4.2: Pyrolysis profiles of the samples synthesized to determine the stoichiometry of each batch type after carbothermal reduction at 1300 °C, 1400 °C and 1500 °C

Sample name	Batch type*	Pyrolysis profile (°C x h)
S0.25-1300	S0.25	1300 x 2
S0.50-1300	S0.50	1300 x 2
S0.75-1300	S0.75	1300 x 2
S1.00-1300	S1.00	1300 x 2
S0.25-1400	S0.25	1400 x 2
S0.50-1400	S0.50	1400 x 2
S0.75-1400	S0.75	1400 x 2
S1.00-1400	S1.00	1400 x 2
S0.25-1500	S0.25	1500 x 2
S0.50-1500	S0.50	1500 x 2
S0.75-1500	S0.75	1500 x 2
S1.00-1500	S1.00	1500 x 2

** A batch of each batch type was synthesized for each sample.*

4.2.2 Characterization

Before the stoichiometry in each batch type was determined, the conversion of the dried gel of S1.00 to the carbothermal reduction product was investigated using thermogravimetric (TG/DSC) and XRD analysis.

A 10 mg sample of the dried gel of S1.00 was heated from 25 °C to 1400 °C at a heating rate of 10 °C/min under flowing argon (100 mL/min, 99.999 %, Afrox) to determine the mass loss during thermal reaction of the dried gel of S1.00 using simultaneous thermal gravimetric and differential scanning calorimetry (TG/DSC, TA Instruments SDT Q600, Necsa)

A single batch of S1.00 was divided into 6 portions and each portion, was carbothermally reduced at a different temperature between 1000 °C and 1500 °C (as described above). The pyrolysis profiles for this investigation are listed in Table 4.3. The samples listed in Table 4.3 were analysed using XRD.

Table 4.3: Pyrolysis profiles for the carbothermal reduction investigation of S1.00

Sample number*	Batch type	Pyrolysis profile (°C x h)
S1.00-1000	S1.00	1000 x 2
S1.00-1100	S1.00	1100 x 2
S1.00-1200	S1.00	1200 x 2
S1.00-1300	S1.00	1300 x 2
S1.00-1400	S1.00	1400 x 2
S1.00-1500	S1.00	1500 x 2

** A single batch of S1.00 was synthesized and divided into 6 portions; each portion was heated at a different temperature between 1000 °C and 1500 °C.*

The XRD patterns of the samples listed in Table 4.3 were collected using a Bruker D8 Advance diffractometer (Necsa) with CuK_α (λ = 0.154060 nm) radiation for angles (2θ) ranging between 15° and 125°. A step scan size of 0.04° (2θ) and acquisition time of 2.0 s per step were used. The Rietveld refinements were performed using the TOPAS V4.2 (Bruker, 2009) software package to determine the weight percentage of each phase in the synthesized samples listed in Table 4.3.

The binding energies of the surface electrons (depth of 2 to 5 nm) of S1.00-1400, S1.00-1500 and a ZrC reference sample were determined by X-ray photoelectron spectroscopy (XPS) using a Thermo ESCAlab 250Xi analyser (NMISA, CSIR) with monochromatic AlK_α (1486.7 eV) radiation. Survey scans were conducted with a 100 eV pass energy while high resolution scans were conducted with 20 eV pass energy under 1 x 10^{-6} Pa pressure and a spot size of 900 µm. The detection limit of XPS is approximately 0.1 at. %.

Quantitative phase analysis as well as cell parameter measurements were performed using XRD and utilizing the Rietveld method to determine the fraction of each phase in each batch type after carbothermal reduction at 1300 °C, 1400 °C and 1500 °C (Table 4.2): A Malvern Panalytical Empyrean diffractometer with Cu K_α (λ = 0.154060 nm) radiation for angles (2θ) ranging between 15° and 120° (step: 0.0130°, step scan time: 16.32 s) was used to obtain the XRD patterns of these samples (Table 4.2). In order to minimise errors that can affect the cell parameter values, an internal standard was also used to correct for sample positioning errors. Alumina (Al_2O_3) with the corundum crystal structure was used as internal standard, as the Al_2O_3 diffraction pattern has minimal overlap with the investigated XRD patterns of ZrC samples. The Al_2O_3 was mixed with the sample powders in a weight ratio of 20%. Rietveld refinements were performed using the PANalytical HighScore Plus analytical software package to fit the

experimental XRD patterns (Figure 4.5). The phases that were considered during the refinements were ZrC (1/1), Al_2O_3 (corundum) and (depending on the presence) monoclinic ZrO_2 (baddeleyite). The weight percentage of all the phases in each of these samples were refined as well as the lattice parameters of the ZrC (1/1) and ZrO_2 phases, the line profile shape parameters and the sample positioning error parameter. (The weight percentage of all the phases in each of these samples as well as their peak positions and d-spacing values are reported in Appendix C.)

The total carbon and oxygen present in the prepared samples containing ZrC were determined by elemental chemical analysis by means of Inert Gas Fusion analysis (IGF) using the Eltra CS 800 (for carbon) and the Eltra ONH 2000 (for oxygen) combustion analysers (Pelindaba Analytical Laboratories, Necsa). The determination of the total weight percent of carbon in the powdered sample was based on the combustion of the sample in an alumina crucible under an oxygen (O_2) atmosphere in an induction furnace (temperatures above 2000 °C). The carbon was converted to CO_2 and then quantified by an infrared detector. The weight percentage of oxygen in each sample was determined by combustion of the sample in a resistance furnace under a helium atmosphere. In order to carry out this analysis, the sample was heated in a carbon crucible to temperatures up to 3000 °C. The oxygen in the sample was converted to CO by reaction with the carbon from the crucible and the amount of CO is determined by infrared detection.

Microstructures of the samples were investigated using Scanning Electron Microscopy (SEM), equipped with energy dispersive spectrometer (EDS) for elemental analysis in the Laboratory for Electron Microscopy at the North-West University. The prepared samples were cast in an epoxy resin and polished to obtain a cross-section of samples of the powders to determine the elemental distribution of zirconium, carbon and oxygen inside the particles.

ZrC reference sample

ZrC powder from Sigma Aldrich (Sigma Aldrich batch no.: 336351) was used as ZrC reference sample. This sample was used as a “check standard” during characterization of the synthesized samples. The XPS, XRD and IGF data of the synthesized samples were also compared to the XPS, XRD and IGF data of the ZrC powder from Sigma Aldrich. The ZrC reference sample is referred to as *ZrC ref* or *ZrC reference sample* throughout this chapter.

4.3 Results

The TG/DSC curves obtained during the conversion of the dried gel of S1.00 to ZrC are given in Figure 4.2. Mass losses are observed in the TG curve (blue curve) throughout the temperature range taking place at varying rates in the following temperature regions: between 80 to 200 °C, 250 to 500 °C and 600 to 1400 °C. An exothermic peak is observed in the DSC curve at approximately 490 °C and at approximately 1210 °C the onset of an exothermic peak is also observed.

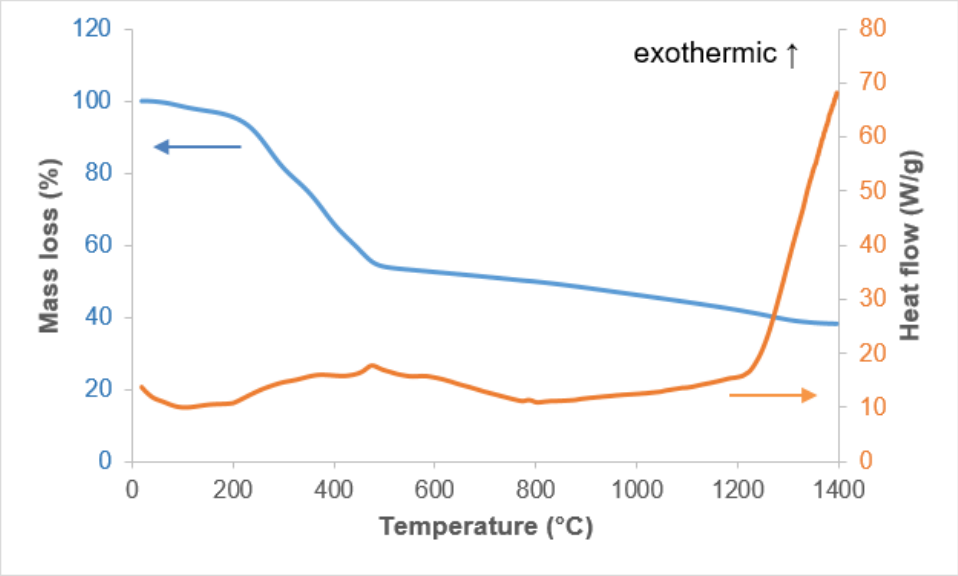

Figure 4.2: **TG/DSC curves of S1.00 during pyrolysis (10 °C/min) under flowing argon to investigate the conversion of the dried gel of S1.00 to form ZrC powders**

Figure 4.3 shows the XRD patterns of S1.00 pyrolysed at different pyrolysis temperatures as listed in Table 4.3. In Figure 4.3 at 1000 and 1100 °C, the 2θ positions of the diffraction peaks of tetragonal ZrO_2 (*t*-ZrO_2, JCPDS 01-079-1771) are marked with black dot labels and at 1100 °C, 1200 °C and 1300 °C, the positions of the diffraction peaks of monoclinic ZrO_2 (*m*-ZrO_2, JCPDS 01-078-0047) are marked with black triangle labels. The position of the ZrC diffraction peaks, at 1200 °C, are marked with black star labels and the indexing of the ZrC phase with the diffraction data file JCPDS 00-035-0784, is given in the XRD pattern of S1.00 at 1500 °C (Figure 4.3). The ZrC phase is observed in the XRD patterns of S1.00 pyrolysed at 1200 °C, 1300 °C, 1400 °C and 1500 °C.

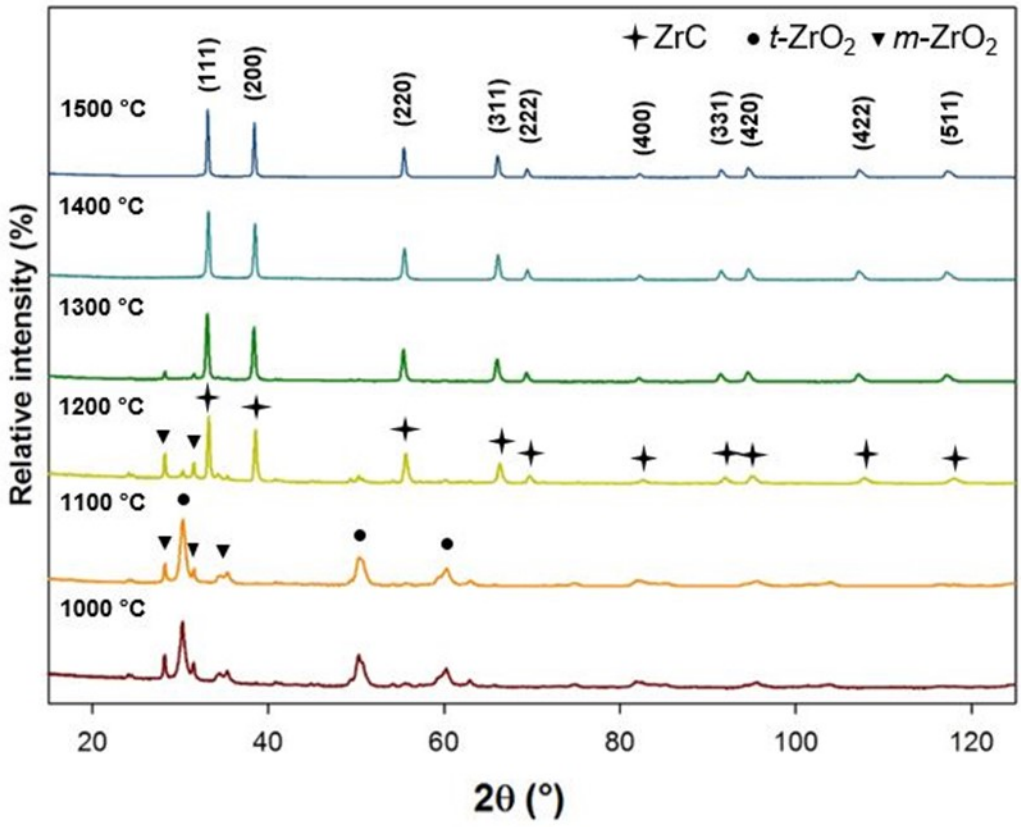

Figure 4.3: **XRD patterns of S1.00, which was pyrolysed at different pyrolysis temperatures between 1000 °C and 1500 °C showing ZrO_2 phase at 1000 °C to 1200 °C and ZrC phase at 1200 °C to 1500 °C**

The energy bands of interest in X-ray photoelectron spectroscopy (XPS) of ZrC type samples are the Zr $3d_{5/2}$, O 1s and C 1s energy bands[f] (Brenier *et al.*, 1999). Given in Figure 4.4, are the enlargements of the energy bands of interest (Zr $3d_{5/2}$, C 1s and O 1s) of the ZrC reference sample, S1.00-1400 and S1.00-1500 as well as a deconvolution of the peaks of S1.00-1500 shown on the right hand side figures (Figure 4.4b, Figure 4.4d and Figure 4.4f) [g].

[f] Notation of the XPS energy bands are described in Appendix C.

[g] Appendix C also contain the deconvoluted peaks of the ZrC reference sample, S1.00-1400 and S1.00-1500 at each energy band investigated.

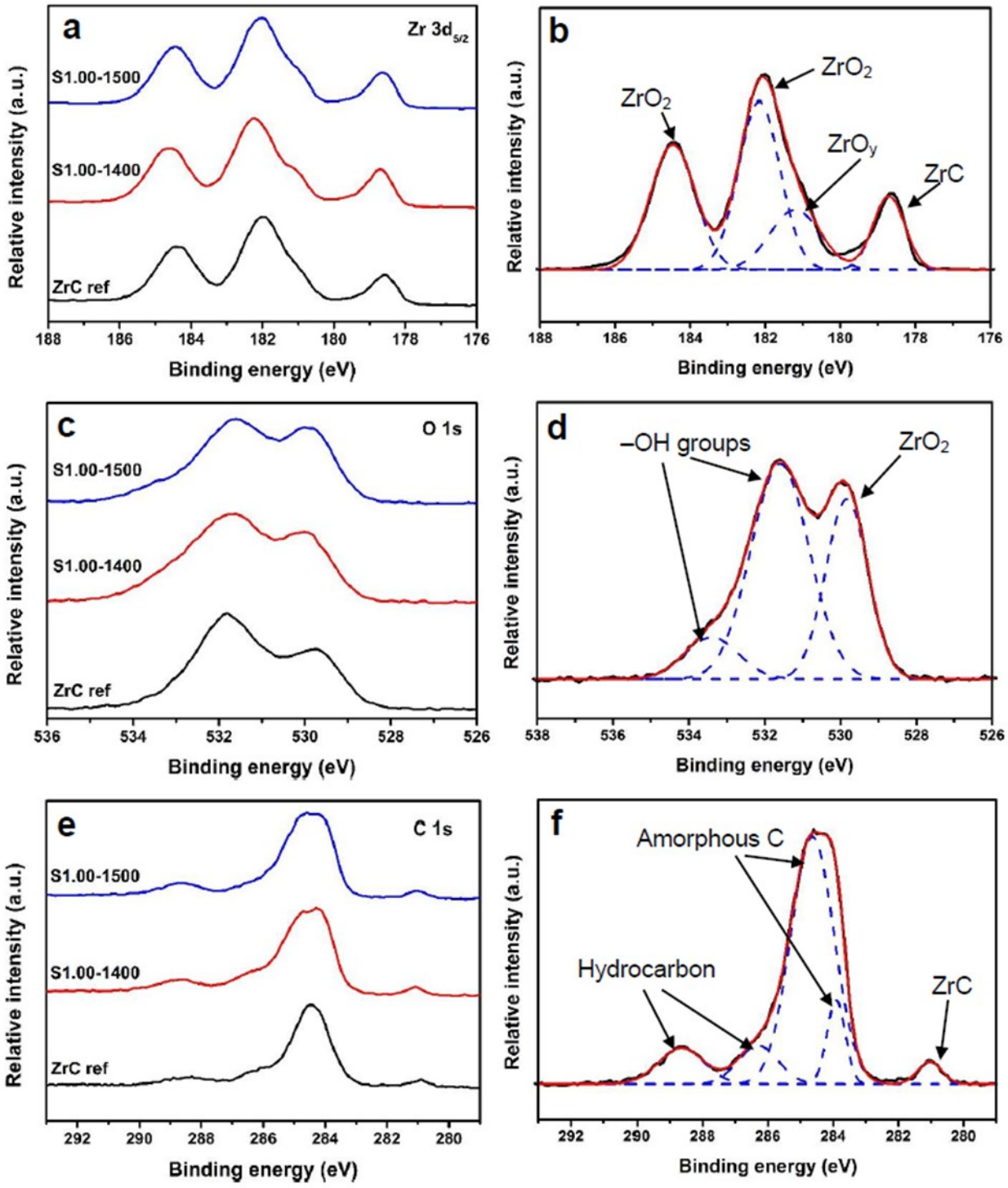

Figure 4.4: **The XPS narrow scan spectra of S1.00-1400 (red), S1.00-1500 (blue) and ZrC reference sample (black) in the region of binding energies of (a) Zr $3d_{5/2}$, (c) O 1s and (e) C 1s core levels. Deconvoluted spectra of each region of binding energies (b) Zr $3d_{5/2}$, (d) O 1s and (f) C 1s core levels of sample S1.00-1500 are given on the right-hand side and labelled with possible compounds contributing to each peak.**

The Zr $3d_{5/2}$ band (Figure 4.4a) of Zr consists of four peaks as shown in the deconvoluted spectra of S1.00-1500 (Figure 4.4b) and centred at the values listed in Table 4.4 for the ZrC reference sample, S1.00-1400 and S1.00-1500.

Table 4.4: The peak positions of the Zr $3d_{5/2}$ energy band (as shown in Figure 4.4a) of S1.00-1400, S1.00-1500 and ZrC reference

Sample	Peak positions (eV)			
ZrC reference	178.7	181.0	182.0	184.6
S1.00-1400	178.8	181.1	182.2	184.8
S1.00-1500	178.7	181.0	182.1	184.7

Three O 1s binding energy peaks centred at the values listed in Table 4.5 are observed for S1.00-1400 and S1.00-1500 as shown in Figure 4.4d, while two binding energy peaks centred at 529.7 eV and 531.8 eV are observed for the ZrC reference sample (black profile in Figure 4.4c).

Table 4.5: The peak positions of the O 1s energy band (as shown in Figure 4.4c) of S1.00-1400, S1.00-1500 and ZrC reference

Sample	Peak positions (eV)		
ZrC reference	529.7	531.8	
S1.00-1400	529.9	531.6	532.7
S1.00-1500	529.8	531.6	533.5

Considering the peak positions of the 1s orbital of C for the ZrC reference sample, S1.00-1400 and S1.00-1500 as listed in Table 4.6 and the observed C 1s spectra of these samples in Figure 4.4e and Figure 4.4f, five binding energy peaks are observed for S1.00-1400 and S1.00-1500, while the ZrC reference sample has four peaks.

Table 4.6: The peak positions of the C 1s energy band (as shown in Figure 4.4e) of S1.00-1400, S1.00-1500 and ZrC reference

Sample	Peak positions (eV)				
ZrC reference	281.1	284.4		286.1	288.4
S1.00-1400	281.1	284.1	285.0	286.2	288.7
S1.00-1500	281.1	284.0	284.8	285.9	288.7

The results presented thus far, are used to determine and identify the formation of ZrC using the Pechini method. The results presented hereafter are used to determine the stoichiometry of each batch type as listed in Table 4.2.

Figure 4.5 illustrates the XRD patterns of samples listed in Table 4.2 pyrolysed at 1300 °C, 1400 °C and 1500 °C. All the XRD patterns presented in Figure 4.5 contain ZrC and Al_2O_3 phases, while all the samples synthesized from batch type S0.25 and S0.50 also show a ZrO_2 phase. The diffraction peak positions of Al_2O_3, indicated by black squares labels, were used as calibration basis to calibrate the 2θ positions of the other peaks (carbide and ZrO_2 phases) that were observed. The carbide phase of all the XRD patterns (in Figure 4.5) was indexed with the JCPDS 00-035-0784 usual diffraction data file of zirconium carbide (1/1) with *Fm3m* space group. Indexation of the carbide peaks is given in the first XRD pattern given in Figure 4.5; this pattern corresponds to the ZrC reference sample (ZrC ref) purchased from Sigma Aldrich. Furthermore, the peak positions of the carbide phase are indicated by black star labels for the patterns at 1400 °C and 1500 °C. The observed zirconia peaks are indicated by black dot labels.

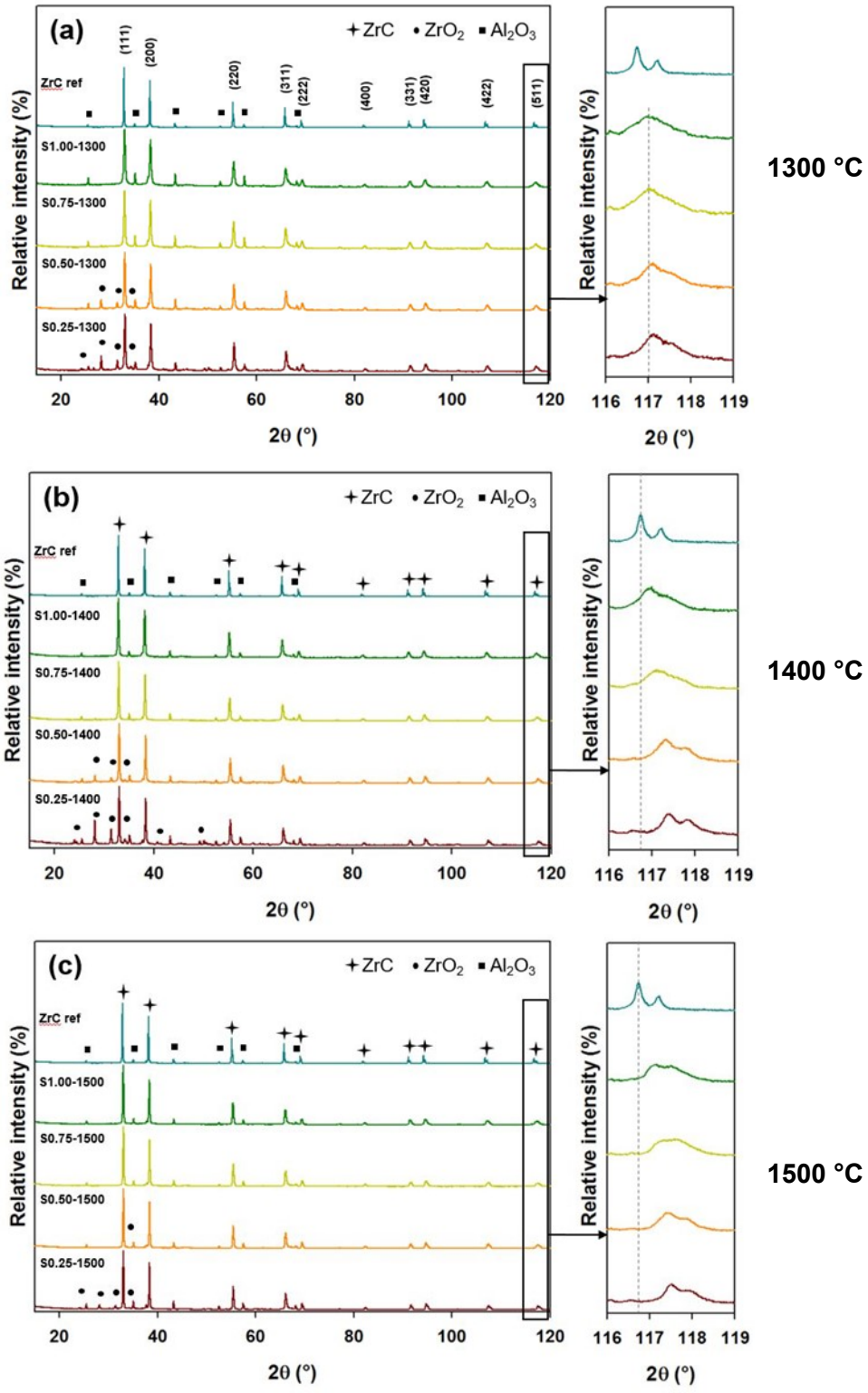

Figure 4.5: **XRD patterns obtained of S0.25, S0.50, S0.75 and S1.00 pyrolysed at different synthesis temperatures (a) 1300 °C, (b) 1400 °C and (c) 1500 °C. The enlargement on the right, shows the peak shift of the (511) diffraction peaks of the synthesized samples in comparison to that of ZrC ref.**

Utilizing Rietveld refinement, the amount of each phase present in the XRD patterns presented in Figure 4.5 were determined and these results are listed in Table 4.7. The lattice parameter of the carbide was also determined *via* Rietveld refinement using the d-spacing and intensities of the ZrC peaks (Table 4.7).

Table 4.7: Rietveld refinement results of S0.25, S0.50, S0.75 and S1.00 pyrolysed at 1300 °C, 1400 °C and 1500 °C and ZrC reference

Sample	ZrC (wt. %)	ZrO_2 (wt. %)	Al_2O_3 (wt. %)	Lattice parameter (nm)
S0.25-1300	45.2	21.4	33.4	0.46928
S0.50-1300	45.9	13.0	41.0	0.46928
S0.75-1300	50.7	1.2	48.0	0.46937
S1.00-1300	52.5	0.0	47.4	0.46943
S0.25-1400	33.0	33.2	33.6	0.46847
S0.50-1400	50.4	13.0	36.6	0.46869
S0.75-1400	57.8	1.8	40.3	0.46909
S1.00-1400	61.2	0.0	38.8	0.46933
S0.25-1500	42.5	10.0	47.2	0.46800
S0.50-1500	58.9	0.8	40.3	0.46831
S0.75-1500	60.7	0.0	39.0	0.46863
S1.00-1500	62.5	0.0	37.4	0.46912
ZrC reference	60.0	0.0	39.8	0.46974

The total carbon and total oxygen content of each sample was determined by IGF analysis and the results are listed in Table 4.8.

Table 4.8: **The total carbon and oxygen present in samples of S0.25, S0.50, S0.75 and S1.00 pyrolysed at 1300 °C, 1400 °C and 1500 °C and ZrC ref**

Sample	C (wt. %)	O (wt. %)
S0.25-1300	7.58	9.81
S0.50-1300	9.01	6.35
S0.75-1300	12.89	3.59
S1.00-1300	16.99	2.01
S0.25-1400	5.41	10.23
S0.50-1400	7.60	6.65
S0.75-1400	9.97	4.39
S1.00-1400	13.56	3.91
S0.25-1500	5.69	8.43
S0.50-1500	8.27	6.91
S0.75-1500	9.15	3.39
S1.00-1500	11.21	3.09
ZrC reference	11.02	0.48

The cross-section of a particle of S1.00-1500 (Figure 4.6), shows that the grains exhibit zoning. The inner area of the grain appears denser than the outer ring of the grain where more pores (the black spots) are present. The centre of the particles is also more homogeneous (in terms of the observed grey area) than the outer edge of the particles.

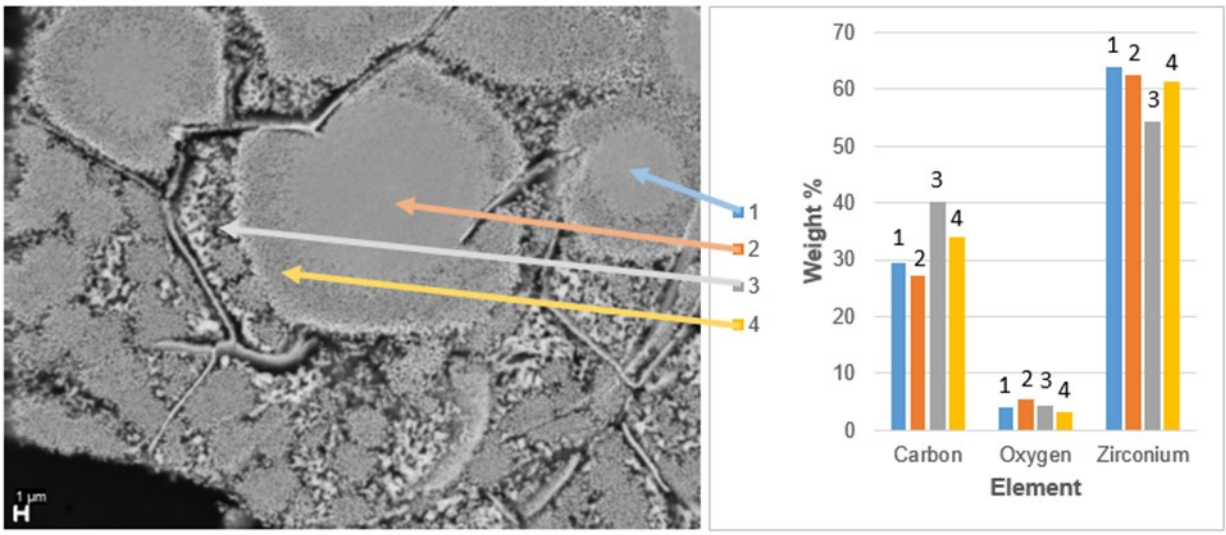

Figure 4.6: **Micrograph of the cross-section of S1.00-1500 and the elemental analysis at each point indicated in the image**

4.4 Discussion

The conversion of the dried gel of S1.00[h] to ZrC was determined by TG/DSC analysis (Figure 4.2). The mass loss in the first region in the TG curve (Figure 4.2), between 80 – 200 °C, is ascribed to the loss of absorbed water. The mass loss in the second region (Figure 4.**2**), between 250 – 500 °C, as well as the exothermic peak of the DSC curve, at approximately 490 °C, is ascribed to the intramolecular dehydration and decarboxylation as well as further carbonisation of the polymeric precursor and the crystallisation of amorphous zirconia with the release of CO_2. Considering the DSC curve (Figure 4.2), the onset of an exothermic peak is observed at approximately 1210 °C, which may be attributed to the carbothermal reduction between the zirconia and carbon to produce ZrC products with the further release of CO_2.

The conversion of the dried gel of S1.00 to ZrC was also determined by pyrolysis of batches of S1.00 at different pyrolysis temperatures and characterizing the powders *via* XRD analysis and the results presented in Figure 4.3. When the pyrolysis temperature was at or below 1000 °C, the main crystalline phase is found to be *t*-ZrO_2. As the temperature increases from 1100 °C to 1200 °C (Figure 4.3), the intensity of the *t*-ZrO_2 peaks decrease with an increase in the intensity of the *m*-ZrO_2 peaks. New diffraction peaks appear in the XRD pattern of S1.00 at a pyrolysis temperature of 1200 °C (Figure 4.3), which can be attributed to the crystal phase of face-centered cubic ZrC, as indexed by the ZrC diffraction data file JCPDS 00-035-0784. The observation that the ZrC phase begins to occur at 1200 °C correlates with the exothermic reaction observed in the DSC analysis shown in Figure 4.2 at roughly the same temperature (1210 °C).

It is thought that the carbothermal reduction of ZrO_2 and carbon thus begins at 1200 °C (as shown in Figure 4.2 and Figure 4.3), owing to the intimate contact of the ZrO_2 and carbon being mixed at a molecular level and the high reaction activity of the (*in-situ* formed) pyrolytic carbon. This onset temperature of 1200 °C obtained using the Pechini method, is significantly lower in comparison to the temperature of 1800 °C needed during traditional solid-state reactions as reported by Maitre and Lefort (1997) and Jain (2004).

As the temperature further increases, the intensity of the ZrO_2 diffraction peaks decreases significantly as the diffraction peaks of the ZrC become more predominant (Figure 4.3). At a pyrolysis temperature of 1400 °C and above, ZrC is the only observed crystalline phase in

[h] Batch type S1.00 was chosen as representative of the other batch types (S0.25, S0.50 and S0.75) during these analyses, because the results of the other batch types follow a similar trend to the results reported of S1.00.

Figure 4.3. Based on the XRD analysis in Figure 4.3, ZrO_2 is as an intermediate product in the formation of ZrC through the depletion of oxygen during the carbothermal reduction reaction.

The Zr $3d_{5/2}$ peak at 178.7 eV (Figure 4.4a) is typical for ZrC, while the Zr $3d_{5/2}$ peaks at 182.1 eV and 184.7 eV (Figure 4.4a) are attributed to stoichiometric ZrO_2 (Matsuoka *et al.*, 2008, Morant *et al.*, 1989). An oxygen-deficient zirconia phase (ZrO_y, $y < 2$) (sub-stoichiometric cubic or tetragonal zirconia) is thought to be the cause of the binding energy signal observed as humps at 181.0 eV in samples S1.00-1400 and S1.00-1500 in Figure 4.4a (Morant *et al.*, 1989). Considering Table 4.4, the peak at 181.0 eV is also observed in the ZrC reference sample.

Corresponding to the observation of a ZrO_2 binding energy peak in the Zr $3d_{5/2}$ spectra (Figure 4.4a), a binding energy peak occurring at 529.8 eV in the O 1s spectra (Figure 4.4c and Figure 4.4d) is also thought to be caused by the presence of stoichiometric ZrO_2 in the samples (ZrC reference sample and S1.00-1400 and S1.00-1500). The O 1s binding energy peaks occurring at 531.6 eV and 533.5 eV (Figure 4.4d) are attributed to hydroxyl species (–OH groups) formed through partial dissociation of adsorbed water (Barreca *et al.*, 2000, Chu *et al.*, 2013).

Considering the peak positions of the 1s orbital of C for the ZrC reference sample, S1.00-1400 and S1.00-1500, the peak occurring at 281.1 eV in Figure 4.4f is ascribed to ZrC (Matsuoka *et al.*, 2008), the peaks occurring at 284.0 eV and 284.8 eV in Figure 4.4f (and 284.4 eV for ZrC reference sample (Table 4.6)) are ascribed to amorphous carbon (Matsuoka *et al.*, 2008), while the peaks occurring at 285.9 eV and 288.7 eV in Figure 4.4f (and 286.1 eV and 288.4 eV for the ZrC reference sample (Table 4.6)) are ascribed to hydrocarbon (Barreca *et al.*, 2000). The presence of hydrocarbons in the samples (ZrC reference sample, S1.00-1400 and S1.00-1500) is attributed to the dissociation of adsorbed water from the atmosphere (Barreca *et al.*, 2000).

Considering the XPS results presented of S1.00-1400, S1.00-1500 and the ZrC reference sample, these samples contain ZrC, ZrO_2 and amorphous carbon. XPS peaks corresponding to zirconium oxycarbide were not observed. The synthesized ZrC powders are thus in close agreement to ZrC powders available commercially.

XPS analysis is a surface analysis technique, which makes it oversensitive to surface groups. The oxygen components observed in the XPS results may be ascribed to surface oxidation of the samples, because particles of ZrC are prone to surface oxidation by atmospheric oxygen, causing ZrO_y, ($y < 2$) to occur.

When the XRD patterns (Figure 4.5) of the samples listed in Table 4.2 are compared to the XRD pattern of the ZrC reference sample, the (511) diffraction peaks of the XRD patterns in Figure 4**.5** is shifted to slightly higher 2θ values, indicating a smaller lattice parameter of the samples as listed in Table 4.7. The smaller lattice parameter is characteristic of the oxycarbide, where some of the carbon atoms are substituted by oxygen atoms (Réjasse *et al.*, 2016). Réjasse *et al.* (2016) further reported that the peak shift ends at the maximum limit of the solid solution of oxygen with the zirconium oxycarbide, which also coincides with the observation of ZrO_2 peaks in the XRD patterns. The (511) peak shift of each XRD pattern is shown in the enlargement on the right hand size in Figure 4.5 and the dashed line in the enlargement serves as a reference basis to indicate the peak shift of the (511) peaks.

The XRD patterns presented in Figure 4.5 indicate that samples prepared from batch type S1.00 and S0.75 that were pyrolysed at 1300 °C, 1400 °C and 1500 °C (Figure 4.5) show single-phase XRD patterns that correlate with the diffraction peaks of the ZrC data file JCPDS 00-035-0784. The XRD patterns of the samples prepared from batch type S0.50 and S0.25 that were pyrolysed at 1300 °C, 1400 °C and 1500 °C (Figure 4.5) also show the diffraction peaks that correlate with the diffraction peaks of the ZrC data file JCPDS 00-035-0784, but a ZrO_2 phase is also present in these XRD patterns. The peak intensity of the ZrO_2 peaks increase as the carbon content of each batch type (S0.50 and S0.25) decreases. The peak intensity of the ZrO_2 peaks also appears to decrease with a rise in pyrolysis temperature.

The Rietveld refinement results (Table 4.7) indicate that only the S1.00-1300 and S1.00-1400 samples showed single-phased XRD patterns without residual ZrO_2 for the samples synthesized at a pyrolysis temperature of 1300 °C and 1400 °C (Figure 4.5a and Figure 4.5b), while samples S1.00-1500 and S0.75-1500 (Figure 4.5c) showed single-phased XRD patterns without residual ZrO_2 after synthesis at a pyrolysis temperature of 1500 °C. The amount of the ZrO_2 phase increases as the carbon content of each batch type (S0.75, S0.50 and S0.25) decreases (Table 4.7). These results indicate that a rise in the pyrolysis temperature results in a higher solubility of oxygen within the lattice of the ZrC powders and is a confirmation of the observation of Réjasse *et al.* (2016).

The oxygen content measured by elemental analysis for each sample (Table 4.8) is the total amount of oxygen present in each sample, i.e. the amount of oxygen in the observed ZrO_2 and possibly the amount of oxygen in the lattice of the prepared ZrC powders. In order to derive the stoichiometry of the prepared ZrC powders, the amount of oxygen in the ZrC lattice needs to be determined. The amount of oxygen in each sample listed in Table 4.8 thus needs to be

recalculated. Subtracting the contribution of ZrO_2 (from Rietveld refinement as listed in Table 4.7) from the elemental analysis results (Table 4.8) the oxygen contribution in each sample could be obtained to be able to derive the stoichiometry for each sample as shown in Table 4.9. The total carbon content for each sample listed in Table 4.2 and the ZrC reference sample was also determined by IGF as presented in Table 4.8. The amount of excess carbon could not be determined analytically. A carbon content close to that of the ZrC reference was used in order to obtain more reliable stoichiometries, while assuming any value higher than 11.1±0.1[i] will be excess C. The recalculated oxygen and carbon content values were used in a formula derived from the stoichiometry calculation work of Gendre *et al.* (2011)[j], to derive the stoichiometries of the prepared samples (Table 4.2) and the ZrC reference sample (Table 4.9).

Table 4.9: The derived stoichiometry of the prepared samples and ZrC ref

Sample	Derived Stoichiometry
S1.00-1300	$ZrC_{0.96}O_{0.04}$
S0.75-1300	$ZrC_{0.95}O_{0.05}$
S0.50-1300	$ZrC_{0.77}O_{0.23}$
S0.25-1300	$ZrC_{0.65}O_{0.35}$
S1.00-1400	$ZrC_{0.94}O_{0.06}$
S0.75-1400	$ZrC_{0.86}O_{0.14}$
S0.50-1400	$ZrC_{0.65}O_{0.35}$
S0.25-1400	$ZrC_{0.46}O_{0.54}$
S1.00-1500	$ZrC_{0.96}O_{0.04}$
S0.75-1500	$ZrC_{0.79}O_{0.21}$
S0.50-1500	$ZrC_{0.71}O_{0.29}$
S0.25-1500	$ZrC_{0.49}O_{0.51}$
ZrC reference	$ZrC_{0.98}O_{0.02}$

Table 4.9 lists the stoichiometries for samples S1.00-1300, S1.00-1400 and S1.00-1500 to be $ZrC_{0.96}O_{0.04}$, $ZrC_{0.94}O_{0.06}$ and $ZrC_{0.96}O_{0.04}$ respectively, which were obtained after pyrolysis of S1.00 at 1300 °C, 1400 °C and 1500 °C respectively. Although samples S1.00-1300, S1.00-1400, S1.00-1500 and S0.75-1500 show a single-phase XRD pattern (Figure 4.5), elemental analysis results show that these samples still contain oxygen. The stoichiometry for batch type

[i] Stoichiometric ZrC contains a carbon content of 11.63 wt%

[j] The Zr content was calculated by subtracting the C and O contributions from 100 wt% like Gendre *et al.* (2011) used in their work.

S1.00 across the temperature range (1300 °C, 1400 °C and 1500 °C) are all close to the same stoichiometry of $ZrC_{0.96}O_{0.04}$ and thus thought to be considered as the upper boundary of the solid solution for O in ZrC.

Considering samples S0.75-1300, S0.75-1400 and S0.75-1500, it can be observed that the amount of dissolved oxygen in the ZrC lattice increases with an increase in pyrolysis temperature, due to the decrease of residual ZrO_2 (Table 4.7) and the increase of oxygen in the ZrC powders (Table 4.9).

The relationship of the lattice parameter (Table 4.7) and carbon content of the pyrolysed samples listed in Table 4.9 are shown in Figure 4.7. Figure 4.7 shows that the lattice parameter increases with an increase in the carbon content of the zirconium oxycarbide powders. Figure 4**.7** further shows that the lattice parameter increases as the pyrolysis temperature decreases, with a maximum lattice parameter of 0.4694 nm for S1.00-1300, which was obtained by pyrolysing S1.00 at 1300 °C. Based on the results in Figure 4.7, a pyrolysis temperature of 1300 °C for carbothermal reduction for 2 hours is the optimum temperature to use for the carbothermal reduction of dried gels synthesized by the Pechini method; as at this temperature the maximum lattice parameter and stoichiometry of $ZrC_{0.96}O_{0.04}$ is achieved. The carbon content in each batch type has a stronger influence on the lattice parameter when the pyrolysis temperature is increased to 1400 °C and 1500 °C.

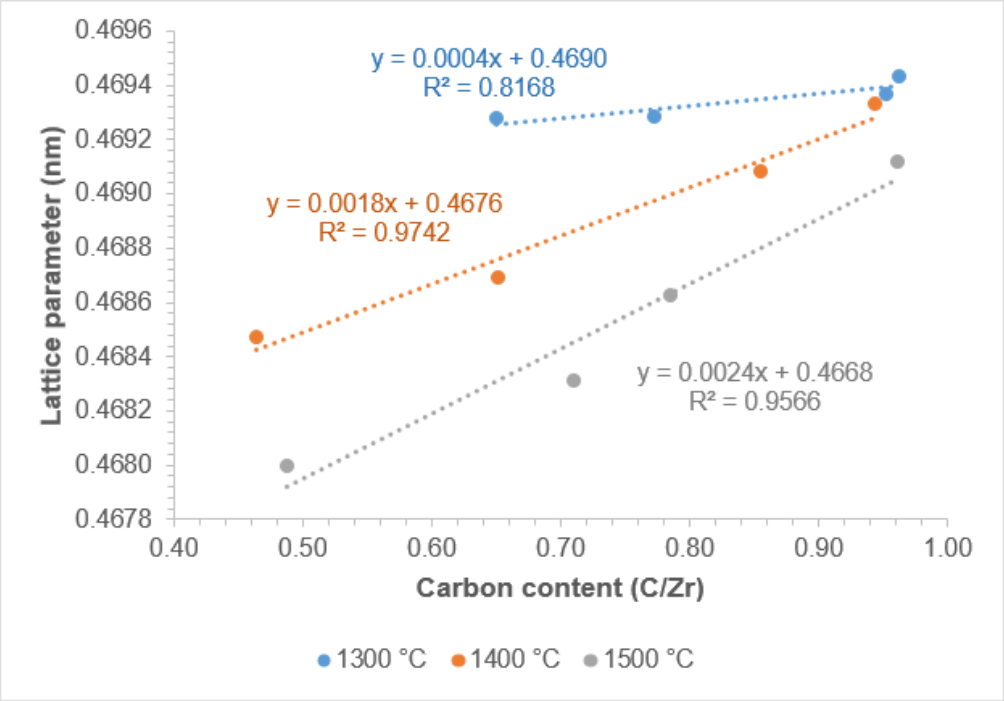

Figure 4.7: **The lattice parameter of ZrC powders with respect to the determined stoichiometric carbon content**

Considering the results discussed in this chapter, the mechanism of the carbothermal reduction reaction used for the synthesis of ZrC, needs to be reviewed as it is important in understanding the equilibrium of the residual ZrO_2 and the stoichiometry of the ZrC powders and understanding this equilibrium, may lead to a basis for modifications in terms of brittleness of ZrC.

4.4.1 Mechanism of carbothermal reduction

The formation of zirconium oxycarbides can be explained by mechanisms of carbothermal reduction of zirconia which have been studied by a number of authors (Maitre and Lefort, 1997, Berger *et al.*, 1999, David *et al.*, 2013, Gruner *et al.*, 2000) and are summarised in essence in the scheme illustrated in Figure 4.8. The formation of ZrC begins with the formation of CO from the solid state reactions of ZrO_2 which is reduced by C at the onset of carbothermal reduction (Maitre and Lefort, 1997, Berger *et al.*, 1999, Gruner *et al.*, 2000, David *et al.*, 2013).

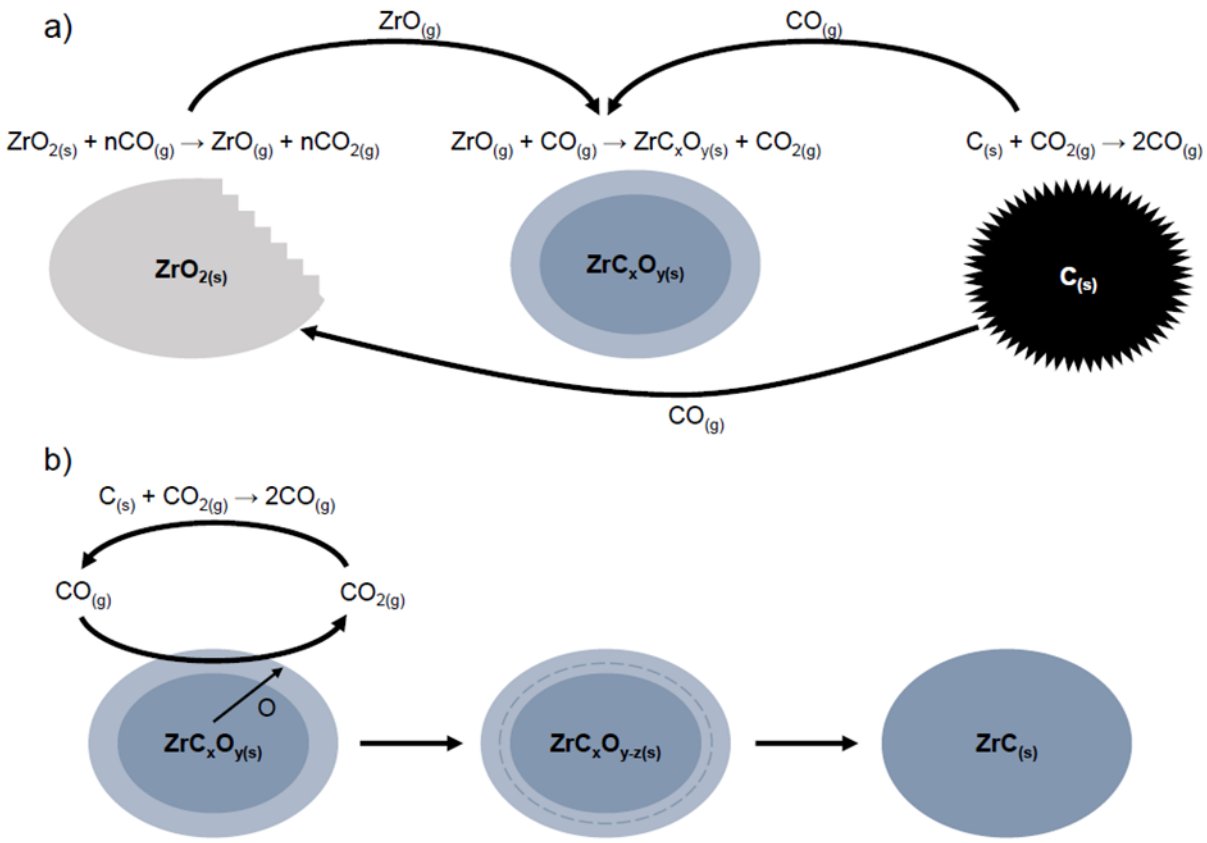

Figure 4.8: **Schematic representation of the reaction schemes involved in (a) the first step and (b) the second step of the carbothermal reduction of ZrO_2, after David *et al.* (2013)**

Gruner *et al.* (2000) postulated the formation of CO with a small amount of CO_2 present at starting temperatures of about 900 °C. The amount of CO and CO_2 formed are controlled by the Boudouard reaction equilibrium in Equation (4.1)

$$C_{(s)} + CO_{2(g)} \rightleftharpoons 2CO_{(g)} \quad (4.1)$$

ZrO_2 is then reduced according to the mechanism suggested in Equation 4.2

$$ZrO_{2(s)} + nCO_{(g)} \rightarrow ZrO_{2-n(s)} + nCO_{2(g)} \quad (4.2)$$

and

$$ZrO_{2-n(s)} + CO_{(g)} \rightarrow ZrC_xO_{y(s)} + CO_{2(g)} \quad (4.3)$$

with fast local regeneration of CO according to Equation 4.1 at high temperatures (Berger *et al.*, 1999). The lattice defects increase with the formation of the sub-stoichiometric $ZrO_{2-n(s)}$ which allows the incorporation of carbon into the vacancies, leading to the $ZrC_xO_{y(s)}$ phase. The reaction rates of formation of the carbide and oxygen loss is not the same and the difference in reaction rates causes sub-stoichiometric $ZrC_xO_{y(s)}$ to form (Harrison and Lee, 2016). The formation of ZrC powders with a residual oxygen content of 0.06% were observed in this study, as shown in Table 4.9.

The mechanism (schematically represented in Figure 4.8) begins with the destabilisation of carbon black and zirconia (zipper-like mechanism), with the formation of sub-stoichiometric $ZrO_{2-n(s)}$ through the removal of oxygen from the zirconia and the oxidation of carbon leading to $CO_{(g)}$ through the Boudouard reaction equilibrium (David *et al.*, 2013). Destabilisation of the zirconia continues until a zirconium layer exists under a Zr-O phase, which can exist as gaseous $ZrO_{(g)}$ and $Zr_{(g)}$ according to David *et al.* (2013). The heterogeneous nucleation and growth of the ZrC_xO_y occur within carbon black agglomerates, which may arise from the co-condensation of $ZrO_{(g)}$ and $CO_{(g)}$ species, followed by solid state diffusion to $ZrC_xO_{y(s)}$. In the second step of the mechanism, the $ZrC_xO_{y(s)}$ is further reduced by contact with $CO_{(g)}$, until the carbide (on the right of the scheme) is eventually formed.

The first step of the mechanism in Figure 4.8, is proven by the observation that the ZrO_2 phase (Figure 4.3) is depleted during the formation of the ZrC phase (Figure 4.3) in the XRD patterns of S1.00 being pyrolysed at varying temperatures between 1000 °C and 1500 °C

The observation of grains showing zoning of varying ZrC_xO_y stoichiometries in Figure 4.6, is similar to step b of the mechanism presented in Figure 4.8. Considering the elemental analysis of the centre of the grains (Figure 4.6), the ratio of the carbon and zirconium (29.58 wt. % C to 63.99 wt. % Zr) is closer to the theoretical stoichiometry of ZrC, (88.4 wt. % Zr and 11.6 wt. % C) while the ratio of the carbon, oxygen and zirconium in the outer layer is closer to zirconium oxycarbide (61.45 wt. % Zr, 33.96 wt. % C and 3.18 wt. % O). The reduction of the oxygen content observed in Figure 4.6, is due to the reduction of the oxycarbide outer layer by the extraction of carbon and oxygen as CO_2, as shown in the first schematic of step b in Figure 4.8.

When the lower lattice parameter values for samples pyrolysed at 1500 °C, as shown in Figure 4.7, is considered and step b in Figure 4.8 is taken into account, the reduction of the oxygen in $ZrC_xO_{y(s)}$ can only be further reduced by contact with $CO_{(g)}$, Thereby it is concluded that the carbothermal reduction reaction of the dried gel of the Pechini method at 1500 °C is not fully equilibrated. This results in ZrC powders with higher oxygen content, because the smaller

lattice parameter values are due to more oxygen atoms in the ZrC lattice, having atomic radii of 0.064 nm in comparison to the larger atomic radii of carbon (0.077 nm).

4.4.2 Comparison of the d-spacing of JCPDS 00-035-0784, ZrC reference and S1.00-1500

After Rietveld refinements were performed to fit the experimental XRD patterns shown in Figure 4.5, the d-spacing values of the ZrC data file (JCPDS 00-035-0784), the ZrC reference and sample S1.00-1500 were compared. Table 4.10 and Table 4.11 serve as comparison tables to compare the d-spacing values of the ZrC data file (JCPDS 00-035-0784) with the d-spacing values of the ZrC reference (Table 4.10) and in Table 4.11 the d-spacing values of the ZrC data file (JCPDS 00-035-0784) and the d-spacing values of sample S1.00-1500 are compared.

The difference in the d-spacing of each Miller plane is listed in the last columns of Table 4.10 and Table 4.11. This difference is ten times smaller when the ZrC data file and S1.00-1500 are compared in comparison to the difference in the d-spacing of each Miller plane for the ZrC data file and the ZrC reference showing that the stoichiometry of the ZrC sample used to generate the ZrC data file is closer to the stoichiometry of S1.00-1500.

Table 4.10: Comparison between the d-spacing values of the ZrC reference sample and the d-spacing values of JCPDS 00-035-0784

			ZrC reference (Sigma Aldrich)			JCPDS 00-035-0784 ZrC file			
h	k	l	Pos. (°2θ)	Rel. Int. (%)	d-spacing (Å)	Pos. (°2θ)	Rel. Int. (%)	d-spacing (Å)	Δd_{hkl}
1	1	1	32.95	100.00	2.71623	33.04	100.00	2.70890	0.007
2	0	0	38.24	77.73	2.35179	38.34	82.00	2.34593	0.006
2	2	0	55.22	46.86	1.66222	55.32	62.00	1.65919	0.003
3	1	1	65.84	35.46	1.41731	65.97	50.00	1.41492	0.002
2	2	2	69.18	14.01	1.35691	69.30	19.00	1.35472	0.002
4	0	0	81.93	5.82	1.17495	82.05	10.00	1.17353	0.001
3	3	1	91.20	11.97	1.07813	91.34	20.00	1.07685	0.001
4	2	0	94.29	15.07	1.0508	94.45	23.00	1.04937	0.001
4	2	2	106.85	11.11	0.95917	107.06	17.00	0.957877	0.001
5	1	1	116.83	6.84	0.90426	117.06	15.00	0.903119	0.001

Table 4.11: Comparison between the d-spacing values of S1.00-1500 and the d-spacing values of JCPDS 00 035 0784

			S1.00-1500			JCPDS 00-035-0784 ZrC file			
h	k	l	Pos. (°2θ)	Rel. Int. (%)	d-spacing (Å)	Pos. (°2θ)	Rel. Int. (%)	d-spacing (Å)	Δd_{hkl}
1	1	1	33.03	100.00	2.70982	33.04	100.00	2.70890	0.0009
2	0	0	38.33	75.78	2.34660	38.34	82.00	2.34593	0.0007
2	2	0	55.33	41.17	1.65906	55.32	62.00	1.65919	-0.0001
3	1	1	65.98	28.96	1.41477	65.97	50.00	1.41492	-0.0001
2	2	2	69.32	11.20	1.35452	69.30	19.00	1.35472	-0.0002
4	0	0	82.10	4.36	1.17300	82.05	10.00	1.17353	-0.0005
3	3	1	91.39	8.76	1.07639	91.34	20.00	1.07685	-0.0005
4	2	0	94.48	11.00	1.04913	94.45	23.00	1.04937	-0.0002
4	2	2	107.09	8.18	0.95769	107.06	17.00	0.957877	-0.0002
5	1	1	117.11	5.13	0.90290	117.06	15.00	0.903119	-0.0002

4.5 Conclusions

In this chapter, a soluble polymeric precursor has been synthesized *via* the Pechini method and the formation of ZrC powders *via* the carbothermal reduction reaction of the dried gels was investigated. The pyrolysis of the precursor (S1.00) was investigated using XRD analysis after various heat treatments between 1000 °C and 1500 °C. It can be concluded that the formation of ZrC starts at temperatures around 1200 °C and is substantially completed by 1500 °C, according to XRD analysis. Afterwards XPS analysis showed that the synthesized ZrC powders are in close agreement to ZrC powders available commercially.

A SEM image of the cross-section of the 1500 °C sample shows that the ZrC particles grow according to the synthesis mechanism discussed. The mechanism also shows that the formation of ZrC is not fully equilibrated after 2 hours at 1500 °C.

The stoichiometries of the synthesized ZrC powders, using the Pechini method and carbothermal reduction, were determined by considering the XRD and IGF analyses results. The amounts of carbon and oxygen in each sample revealed that even samples with an excess amount of initial carbon (more than the required 3 moles carbon, according to Equation 3.1) formed ZrC powders with a stoichiometry of $ZrC_{0.96}O_{0.04}$. The amount of carbon in the

stoichiometry of the ZrC powders does not change with variation in temperature, while the maximum solubility of oxygen in the ZrC powders decreases with a decrease in temperature.

The Pechini method was chosen as synthesis method due to oxygen not being reported in the ZrC powders synthesized from this method, but like all of the other solution-based synthesis methods using carbothermal reduction to synthesize ZrC, the Pechini method also forms oxygen containing ZrC powders. However, the best results for ZrC synthesis *via* the Pechini method, is achieved after carbothermal reduction at 1300 °C for 2 hours.

The stoichiometry of the ZrC used to generate the ZrC data file JCPDS 00 035 0784, is closer to the stoichiometry of S1.00-1500, which was shown in this chapter to be $ZrC_{0.96}O_{0.04.}$

4.6 References

BARRECA, D., BATTISTON, G.A., GERBASI, R., TONDELLO, E. and ZANELLA, P. 2000. Zirconium dioxide thin films characterized by XPS. *Surface Science Spectra,* 7**,** 303-309.

BERGER, L.M., GRUNER, W., LANGHOLF, E. and STOLLE, S. 1999. On the mechanism of carbothermal reduction processes of TiO_2 and ZrO_2. *International Journal of Refractory Metals and Hard Materials,* 17**,** 235-243.

BRENIER, R., MUGNIER, J. and MIRICA, E. 1999. XPS study of amorphous zirconium oxide films prepared by sol–gel. *Applied Surface Science,* 143**,** 85-91.

BRUKER, A.X.S. 2009. TOPAS, Version 4.2. Karlsruhe, Germany,: Bruker AXS.

CHU, A., QIN, M., RAFI UD, D., ZHANG, L., LU, H., JIA, B. and QU, X. 2013. Carbothermal synthesis of ZrC powders using a combustion synthesis precursor. *International Journal of Refractory Metals and Hard Materials,* 36**,** 204-210.

DAVID, J., TROLLIARD, G., GENDRE, M. and MAÎTRE, A. 2013. TEM study of the reaction mechanisms involved in the carbothermal reduction of zirconia. *Journal of the European Ceramic Society,* 33**,** 165-179.

GENDRE, M., MAÎTRE, A. and TROLLIARD, G. 2011. Synthesis of zirconium oxycarbide (ZrC_xO_y) powders: Influence of stoichiometry on densification kinetics during spark plasma sintering and on mechanical properties. *Journal of the European Ceramic Society,* 31**,** 2377-2385.

GRUNER, W., STOLLE, S. and WETZIG, K. 2000. Formation of CO_x species during the carbothermal reduction of oxides of Zr, Si, Ti, Cr, W, and Mo. *International Journal of Refractory Metals and Hard Materials,* 18**,** 137-145.

HARRISON, R.W. and LEE, W.E. 2016. Processing and properties of ZrC, ZrN and ZrCN ceramics: a review. *Advances in Applied Ceramics,* 115**,** 294-307.

JAIN, A. 2004. *Synthesis and processing of nanocrystalline zirconium carbide formed by carbothermal reduction.* Master of Science Thesis, Georgia Institute of Technology.

MAITRE, A. and LEFORT, P. 1997. Solid state reaction of zirconia with carbon. *Solid State Ionics,* 104**,** 109-122.

MATSUOKA, M., ISOTANI, S., SUCASAIRE, W., KURATANI, N. and OGATA, K. 2008. X-ray photoelectron spectroscopy analysis of zirconium nitride-like films prepared on Si(100) substrates by ion beam assisted deposition. *Surface and Coatings Technology,* 202**,** 3129-3135.

MORANT, C., SANZ, J., GALAN, L., SORIANO, L. and RUEDA, F. 1989. An XPS study of the interaction of oxygen with zirconium. *Surface Science,* 218**,** 331-345.

PECHINI, M. and ADAMS, N. 1967. Method of preparing lead and alkaline earth titanates and niobates and coating method using the same to form a capacitor. US Patent 3330697.

RÉJASSE, F., RAPAUD, O., TROLLIARD, G., MASSON, O. and MAÎTRE, A. 2016. Experimental investigation and thermodynamic evaluation of the C–O–Zr ternary system. *RSC Advances,* 6**,** 100122-100135.

YAN, C., LIU, R., ZHANG, C. and CAO, Y. 2015. Zirconium carbide, hafnium carbide and their ternary carbide nanoparticles by an in situ polymerization route. *RSC Advances,* 5**,** 36520-36529.

CHAPTER 5 ZIRCONIUM CARBIDE SYNTHESIS USING MAGNESIOTHERMIC REDUCTION

5.1 Introduction

In this chapter, ZrC powders are synthesized *via* magnesiothermic reduction of zirconia (that was one of the products formed by pyrolysing the dried gels of the Pechini method at 900 °C in an argon atmosphere). The effects of processing parameters such as temperature and time on the synthesis of ZrC were investigated.

According to the results in the previous chapter, ZrC powders synthesized *via* the Pechini method still contain oxygen. The oxygen in the ZrC powders are due to the, *in situ* formed, ZrO_2 that was not completely reduced during carbothermal reduction as shown in Figure 4.8. It is thus necessary to find a process that removes the oxygen during the synthesis of ZrC powders when using the Pechini sol-gel method with carbothermal reduction.

In an effort to find an element with a higher affinity to oxygen than zirconium, the Ellingham Diagram is used to identify metals with a Gibbs free energy of metal oxide formation smaller than that of zirconium; as these metals will rather favour the oxidation of themselves rather than oxidizing zirconium. With this in mind magnesium was chosen as “oxygen-getter” during the subsequent re-synthesis of ZrC_x (*via* carbothermal reduction). This chapter endeavours to present these efforts and outcomes.

The following reactions might take place during magnesiothermic reduction of ZrO_2 according to Khangkhamano (2014), Li *et al.* (2010), Kobayashi *et al.* (1993) and Davoodi *et al.* (2015):

$ZrO_2 + 2Mg \rightarrow Zr + 2MgO$ (5.1); ΔH_{298K} = -103.21 kJ/mol

$Zr + C \rightarrow ZrC$ (5.2); ΔH_{298K} = -196.38 kJ/mol

$ZrO_2 + C \rightarrow Zr + CO_2$ (5.3); ΔH_{298K} = 706.51 kJ/mol

$ZrO_2 + 2C \rightarrow ZrC + CO_2$ (5.4); ΔH_{298K} = 510.13 kJ/mol

$2Mg + 3C \rightarrow Mg_2C_3$ (5.5); ΔH_{298K} = 80.97 kJ/mol

$C + 2MgO \rightarrow 2Mg + CO_2$ (5.6); ΔH_{298K} = 809.71 kJ/mol

$ZrO_2 + 3C \rightarrow ZrC + 2CO$ (5.7); ΔH_{298K} = 677 kJ/mol

Figure 5.1 shows the Gibbs free energy changes (ΔG) of reactions 5.1 to 5.7, calculated as a function of temperature. Only reactions 5.1 and 5.2 have negative ΔG values over the calculated temperature range and are thus thermodynamically favourable reactions to occur during the magnesiothermic reduction of ZrO_2.

Three possible sub-reactions can be predicted from the results in Figure 5.1:

(a) ZrO_2 could be reduced by Mg according to reaction 5.1 rather than by carbon as described by reaction 5.3.

(b) The formation of ZrC occurs according to reaction 5.2 rather than the direct reduction reaction of ZrO_2 with carbon as described by reactions 5.4 and 5.7. However, it was reported by Chu *et al.* (2013) and Yan *et al.* (2007) that reaction 5.3 becomes favourable at temperatures above 1500 °C during the method of carbothermal reduction.

(c) The presence of the intermediate reaction 5.5 is unlikely to occur, due to the positive value of ΔG in the experimental temperature range.

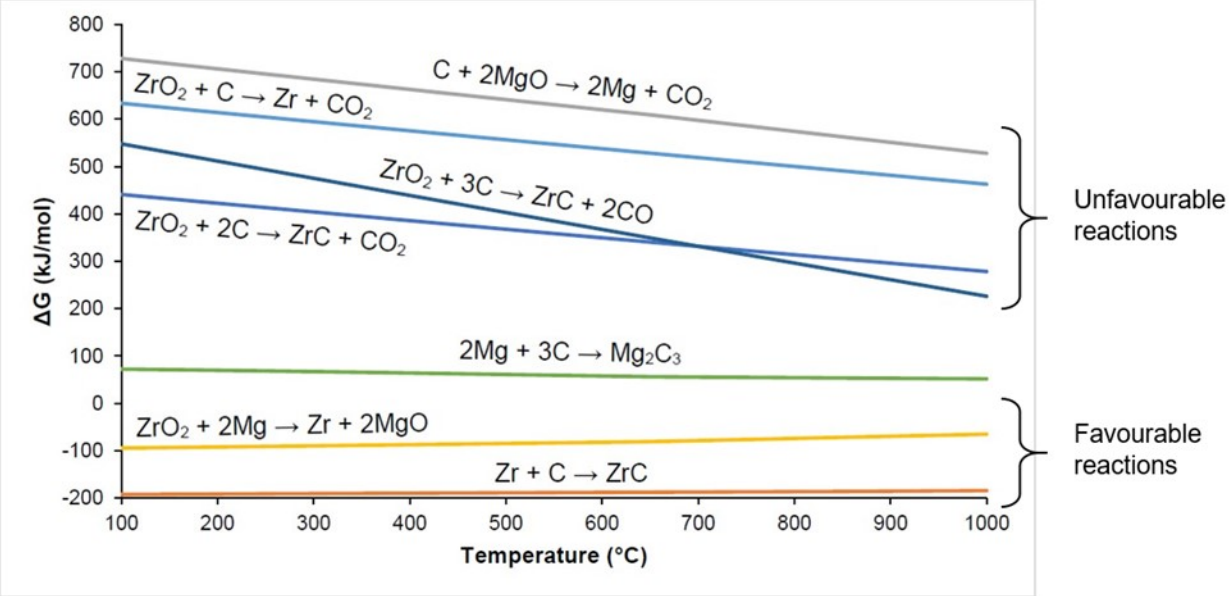

Figure 5.1: Gibbs free energy changes (ΔG) as a function of temperature of possible reactions during magnesiothermic reduction of ZrO_2

5.2 Experimental

5.2.1 Synthesis procedure

The dried gel of batch type S1.00 (described in Chapter 4) was pyrolysed at 900 °C for 1 h in stainless steel crucibles in a quartz tube furnace under argon flow with a ramping rate of 10 °C/min to produce a mixture of ZrO_2 and C as reaction products. This ZrO_2+C mixture (0.5 g) and magnesium powder (≥99%, Sigma Aldrich) were mixed in a stainless steel crucible and heated to temperatures between 700 – 900 °C under flowing argon in a sealed quartz tube furnace (ramp rate of 5 °C/min with a holding time ranging between 1 to 8 hours).

The temperature range and holding time for the magnesiothermic reduction of the ZrO_2 in the ZrO_2+C mixture was chosen based on the work of Khangkhamano (2014) and Ji *et al.* (2012). While the mass of the Mg powder added to the ZrO_2+C mixture was determined by calculating the mass for a 2.2 molar ratio of Mg (Kobayashi *et al.*, 1993) to the ZrO_2 that is in the ZrO_2+C mixture. The percentage of ZrO_2 in the ZrO_2+C mixture was experimentally determined by TG analysis to be 70.78 wt. % (Figure 5.2). Using 0.5 g of the ZrO_2+C mixture, approximately 0.35 g is ZrO_2 and thus 0.15 g Mg powder is needed for a 2.2 molar ratio. However, the experimental set-up used in this study, uses an open crucible in comparison to the closed reaction vessels used by Khangkhamano (2014) and Ji *et al.* (2012). To compensate for possible Mg losses, it was decided to use 0.2 g instead of 0.15 g Mg powder as a “close to stoichiometrical” mass for the magnesiothermic reduction of the ZrO_2+C mixture. Ji *et al.* (2012) reported the synthesis of ZrC/C nanocomposite through magnesiothermic reduction by reacting a weight to weight mixture of a ZrO_2 and C mixture and Mg powder; a weight to weight mixture of ZrO_2+C mixture and Mg powder was thus also investigated.

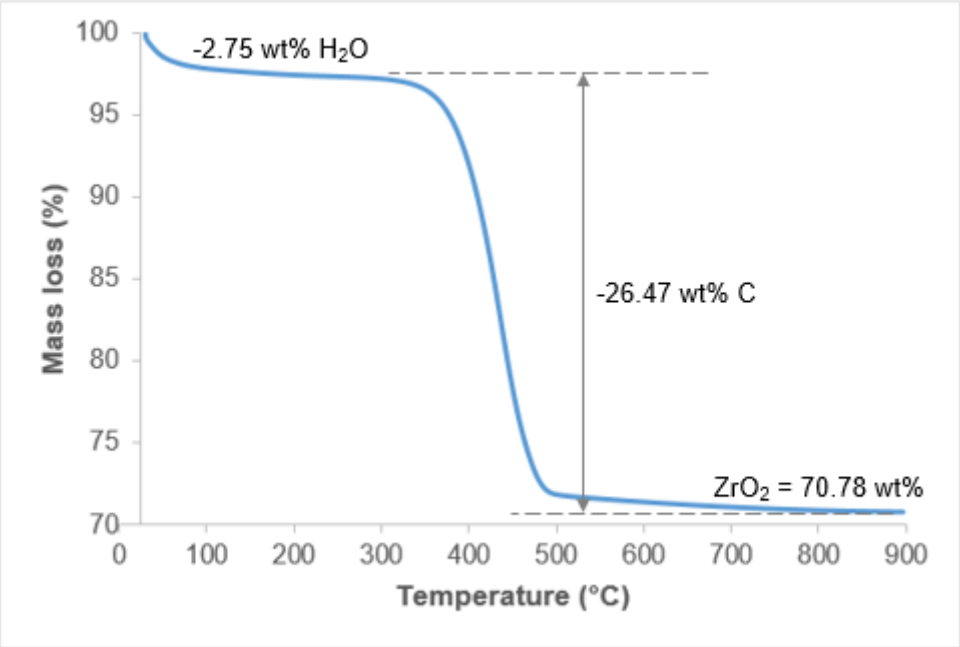

Figure 5.2: **TG curve of the ZrO_2+C mixture heated to 900 °C under an air atmosphere, showing the mass loss due to the oxidation of the carbon in the ZrO_2+C mixture. Mass losses between 25 and 100 °C and between 350 and 700 °C, are attributed to the loss of water and carbon respectively.**

Magnesiothermic reduction reactions to synthesize ZrC were conducted as shown in Table 5.1, with the variations in parameters as discussed above to determine whether the Mg acted as an “oxygen-getter”.

Table 5.1: Parameters for the synthesis of ZrC *via* magnesiothermic reduction reactions

Sample name*	Temperature (°C)	Holding time (hours)	Added Mg (g)
S700-1h-2	700	1	0.2
S700-8h-2	700	8	0.2
S700-1h-5	700	1	0.5
S700-8h-5	700	8	0.5
S800-1h-2	800	1	0.2
S800-8h-2	800	8	0.2
S800-1h-5	800	1	0.5
S800-8h-5	800	8	0.5
S900-1h-2	900	1	0.2
S900-8h-2	900	8	0.2
S900-1h-5	900	1	0.5
S900-8h-5	900	8	0.5

* The sample name is constructed from the reaction temperature, time and the mass of Mg powder added to 0.5 g of ZrO_2+C mixture.

5.2.2 Chracterization

The amount of carbon in the ZrO_2+C mixture was determined by heating a sample of the ZrO_2+C mixture (10 mg) from 25 °C to 900 °C at a heating rate of 5 °C/min using TG/DSC (TA Instruments SDT Q600, Necsa) under an air atmosphere (100 mL/min, 99.995 %, Afrox).

A weight to weight powder mixture of magnesium powder and ZrO_2+C mixture was also subjected to TG/DSC analysis to study the reaction mechanism during heating. This mixture was heated from room temperature to 1200 °C at a heating rate of 1 °C/min under an argon atmosphere.

The phase composition of the samples listed in Table 5.1 were identified by X-ray diffraction (XRD) using a Bruker D8 Advance Diffractometer with Cu K_α (λ = 0.15418 nm) radiation for angles (2θ) ranging between 15° and 120° (scan step: 0.04°, step time: 2.0 s). Rietveld refinement using the TOPAS V4.2 (Bruker, 2009) software package was used to quantify each crystalline phase in the XRD patterns. (The weight percentage of all the phases in these samples as well as their peak lists are reported in Appendix C.)

5.3 Results

The TG/DSC curves of a weight to weight powder mixture of magnesium powder and ZrO_2+C mixture heated to 1200 °C are given in Figure 5.3. The TG curve exhibits a mass loss between 25 and 650 °C and a mass gain between 650 to 700 °C, while the DSC curve exhibits a major exothermic peak at approximately 650 °C. The TG and the DSC curves show a decrease in mass from 750 °C up to 1000 °C (TG) and a decrease in the heat flow (DSC) from 750 °C up to 1200 °C.

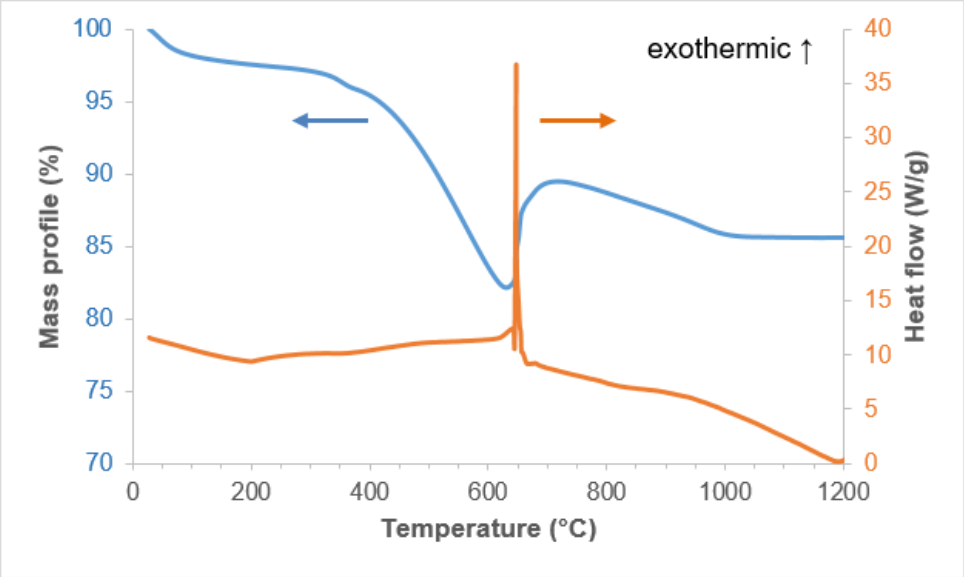

Figure 5.3: Magnesiothermic reaction TG/DSC curves

The XRD patterns of S700-1h-2, S800-1h-2 and S900-1h-2 are given in Figure 5.4. The following crystalline phases were detected in the XRD patterns in Figure 5.4: ZrC (JCPDS 00-035-0784) labelled by black star labels, ZrO_2 (JCPDS 00-024-1165 and 01-083-0809) labelled by black dot labels and MgO (JCPDS 01-078-0430) labelled by black moon labels. ZrC is observed as the main crystalline phase in each XRD pattern in Figure 5.4. The intensity of the ZrO_2 peaks decrease with the rise in temperature and ZrO_2 peaks could not be observed in the XRD pattern of the sample heated at 900 °C.

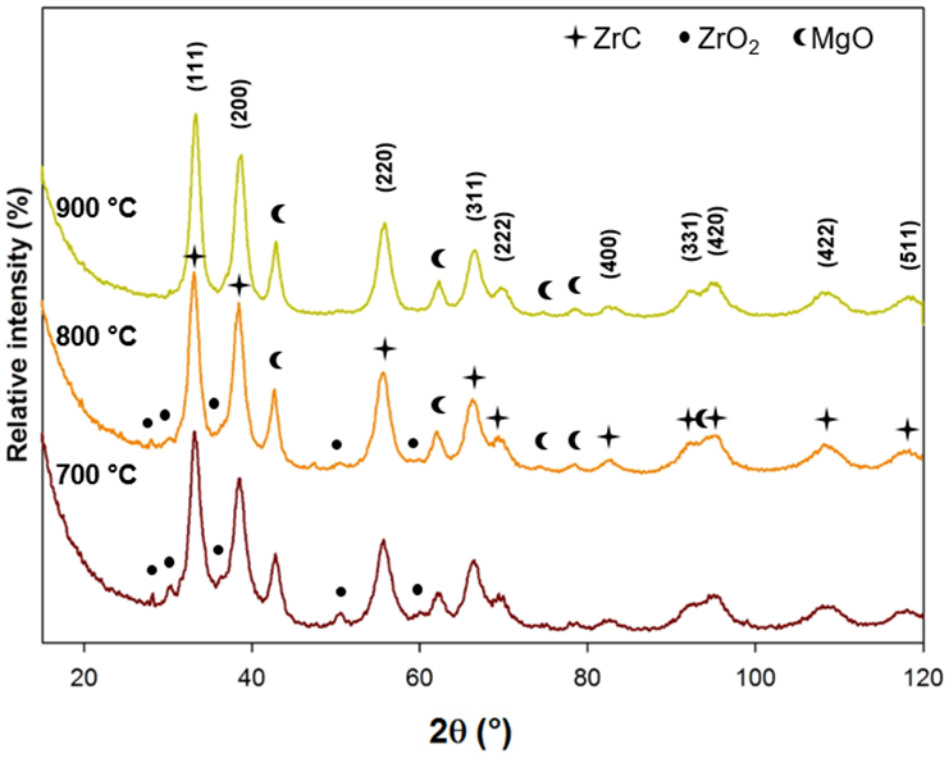

Figure 5.4: **XRD patterns after heating at 700 °C, 800 °C and 900 °C respectively, samples contained 0.2 g Mg and were kept at temperature for 1 hour**

The XRD patterns of S700-8h-2, S800-8h-2 and S900-8h-2 are given in Figure 5.5. The following crystalline phases were detected in the XRD patterns (Figure 5.5): ZrC (JCPDS 00-035-0784), ZrO_2 (JCPDS 00-024-1165) and MgO (JCPDS 01-078-0430) labelled by black star, dot and moon labels respectively. ZrC is observed as the main crystalline phase in the XRD patterns of each temperature investigated in Figure 5.5. The intensity of the ZrO_2 peaks decrease with the rise in temperature and ZrO_2 peaks could not be observed in the XRD pattern of the sample heated at 900 °C.

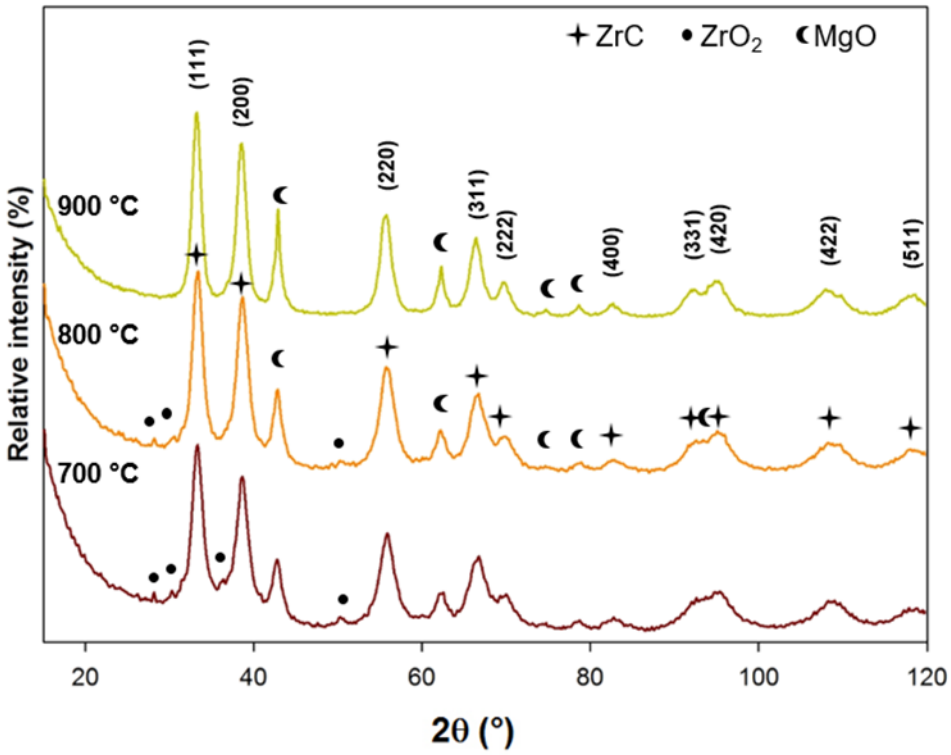

Figure 5.5: **XRD patterns after heating at 700 °C, 800 °C and 900 °C respectively, samples contained 0.2 g Mg and were kept at temperature for 8 hours**

The XRD patterns of S700-1h-5, S800-1h-5 and S900-1h-5 are given in Figure 5.6. The following crystalline phases were detected in the XRD patterns given in Figure 5.6: ZrC (JCPDS 00-035-0784) labelled by black star labels, ZrO_2 (JCPDS 00-024-1165) labelled by black dot labels, MgO (JCPDS 01-078-0430) labelled by black moon labels and in the sample heated at 700 °C, Mg (JCPDS 00-035-0821) labelled by black diamond labels. ZrC is observed as the main crystalline phase in the XRD patterns of the samples heated at 800 °C and 900 °C in Figure 5.6, while Mg is the main crystalline phase in the XRD pattern of the sample heated at 700 °C. The intensity of the ZrO_2 peaks decrease with the rise in temperature and ZrO_2 peaks could not be observed in the XRD patterns of the samples heated at 800 °C and 900 °C.

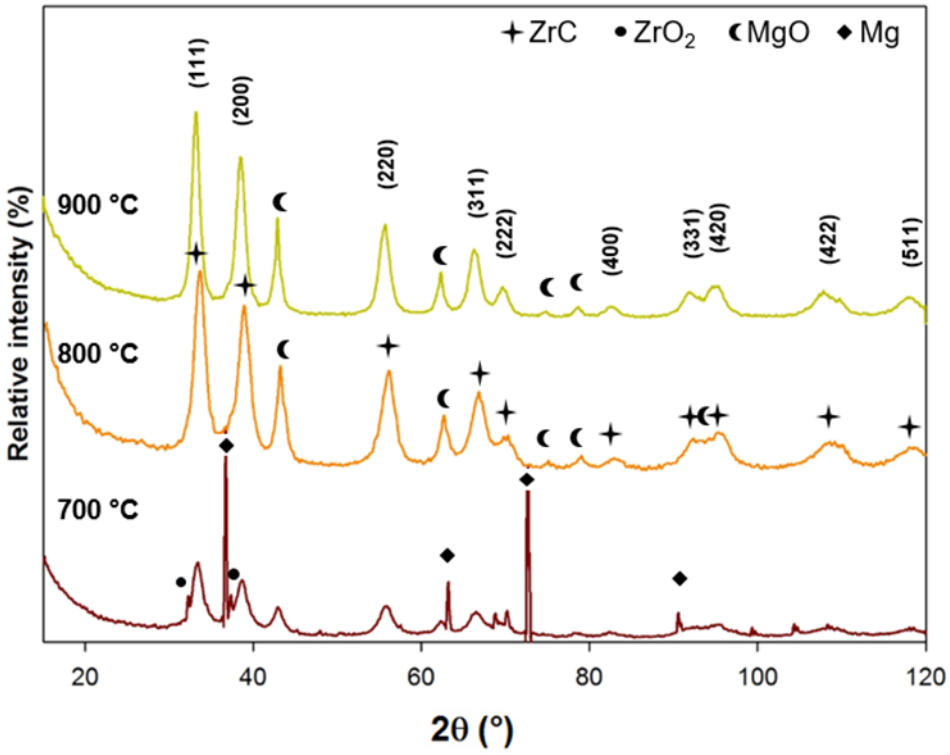

Figure 5.6: **XRD patterns after heating at 700 °C, 800 °C and 900 °C respectively, samples contained 0.5 g Mg and were kept at temperature for 1 hour**

The XRD patterns of S700-8h-5, S800-8h-5 and S900-8h-5 are given in Figure 5.7. The following crystalline phases were detected in the XRD patterns (Figure 5.7): ZrC (JCPDS 00-035-0784) and MgO (JCPDS 01-078-0430) labelled with black star and black moon labels respectively. ZrC is observed as the main crystalline phase in each XRD pattern in Figure 5.7 and no ZrO_2 peaks were observed in the XRD patterns for all the temperatures investigated in Figure 5.7.

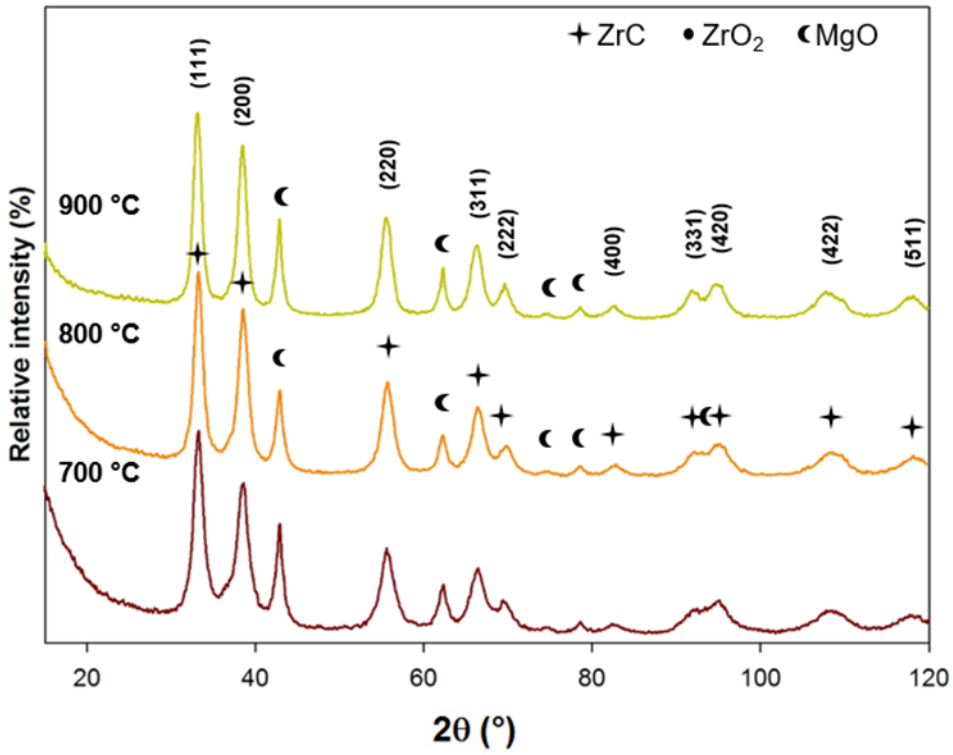

Figure 5.7: **XRD patterns after heating at 700 °C, 800 °C and 900 °C respectively, samples contained 0.5 g Mg and were kept at temperature for 8 hours**

The Rietveld refinement results of each phase present in the XRD patterns from Figure 5.4 to Figure 5.7 are given in Figure 5.8. The two straight lines are calculated from Equation 5.8 to show the theoretical yields of ZrC (56.15 wt. %) and MgO (43.85 wt. %):

$$ZrO_2 + 2Mg + C \rightarrow ZrC + 2MgO \quad (5.8)$$

Samples S900-1h-5, S700-8h-5, S880-8h-5 and S900-8h-5 show ZrC and MgO results similar to the theoretical yields of ZrC and MgO respectively.

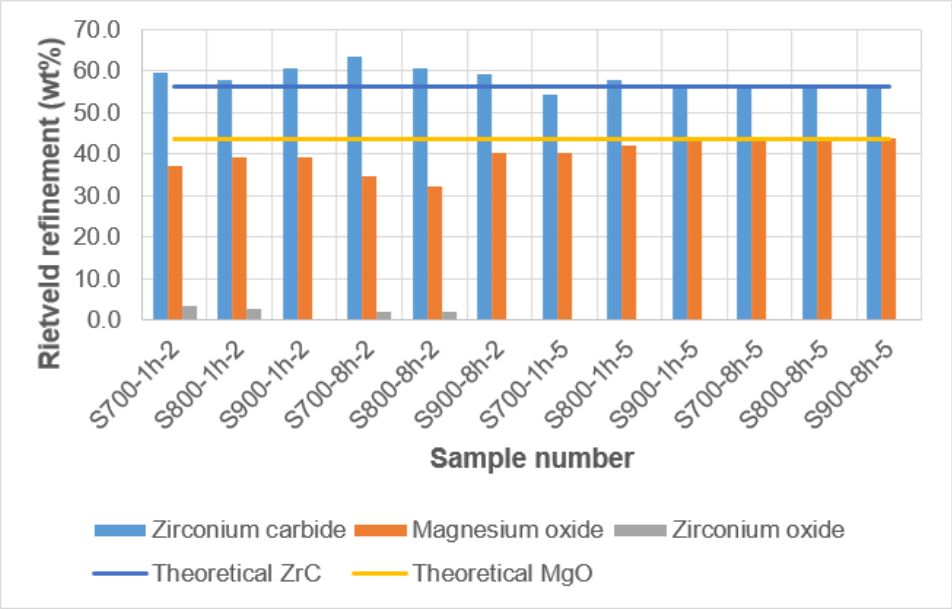

Figure 5.8: The amount of ZrC, ZrO_2 and MgO per sample according to Rietveld

5.4 Discussion

Considering the results in Figure 5.3, a sharp exothermic peak appears at 650 °C, indicating the magnesiothermic reduction taking place between the magnesium and the zirconium oxide and the reaction of the zirconium with the carbon to form zirconium carbide. It is thought that a mass gain in the TG curve also observed at 650 °C is due to the formation of magnesium oxide and zirconium carbide. By comparison of the Mass profile curve of Figure 5.3 with the Mass loss curve in Figure 4.2, the mass loss observed in the TG curve (Figure 5.3) between 25 °C and 650 °C, is thought to be due to the loss of adsorbed atmospheric water and the evaporation of some residual carbon and oxygen complexes that formed during the pyrolysis of the dried gel of S1.00 at 900 °C that might still be present in the ZrO_2+C mixture.

In terms of the XRD patterns in Figure 5.4 and Figure 5.5, the intensity of the ZrO_2 peaks decreases with the increase in synthesis temperature and ZrO_2 peaks could not be observed for the samples pyrolysed at 900 °C. This observation shows the advantage of the magnesiothermic reduction method to synthesise ZrC at lower temperatures, compared to carbothermal reduction which only starts to form ZrC at 1200 °C (discussed in the previous chapter). The peak intensity of the observed ZrO_2 peaks in Figure 5.5 are lower in comparison

to the observed ZrO_2 peaks in Figure 5.4, showing that an increase in the reaction time decreases the ZrO_2 phase present in the samples. The peak shape of the XRD patterns in Figure 5.5 also appears sharper than the peak shape of the XRD patterns in Figure 5.4; an increase in the holding time thus improve the crystallinity and ordering of the crystal structure of ZrC.

Due to the ZrO_2 peaks still being present in the samples heated to 700 °C and 800 °C (Figure 5.5), the amount of Mg powder was increased to investigate the effect of additional Mg powder on the reactions. Figure 5.6 shows Mg peaks in the XRD pattern of sample S700-1h-5, indicating the existence of excess Mg in S700-1h-5, while the XRD pattern of S800-1h-5 show an increase in the ZrC and MgO peaks, thus by increasing the amount of Mg powder added to the reaction mixture, the results presented in Figure 5.4 and Figure 5.5 could be improved upon. The peaks of the XRD patterns of Figure 5.7 are the sharpest in comparison with the peaks in the XRD patterns of Figure 5.4, Figure 5.5 and Figure 5.6 indicating that a larger amount of excess Mg powder also improves the crystallinity of the powders synthesised at a holding time of 8 hours. These results differ from the work of Khangkhamano (2014), who still observed ZrO_2 in the samples heated at 950 °C for 8 hours, while a higher crystallinity of the ZrC phase was also observed (Figure 5.7) in comparison to XRD patterns reported by Ji et al. (2012).

Figure 5.8 shows that all the samples synthesised with 0.2 g Mg powder show results of more than the theoretical value for ZrC (56.15 wt. %), while the values for MgO are less than the theoretical value of MgO (43.85 wt. %). After the synthesis of each sample, silver-white crystals were observed on the inner wall of the quartz tube, that is thought to be due to the evaporation of Mg (vapour pressure of 1.3×10^3 Pa at 743 °C and 1.3×10^4 Pa at 909 °C (Kobayashi *et al.*, 1993)). ZrO_2 is also observed for all the samples synthesised with 0.2 g Mg powder except for S900-1h-2, for which no ZrO_2 phase was observed. Along with the evaporation of the Mg powder, the activation temperature and time of the reaction was not effective. Increasing the Mg powder to 0.5 g leads to 5% excess Mg (not shown in Figure 5.8) being observed for the sample heated at 700 °C for 1 hour (Figure 5.6), while the values for ZrC and MgO of the other samples are all close to the theoretical values for ZrC and MgO. Rietveld refinement and XRD analysis shows the optimal reaction conditions to synthesize ZrC is a weight to weight mixture of ZrO_2+C mixture and Mg powder, heated to 900 °C with a holding time of 1 hour.

Following this observation, a sample (S900-1h-5) was subjected to SEM and EDS analysis[k]. A back-scattered electron micrograph of the cross-section of particles of S900-1h-5 is shown on the left in Figure 5.9. The image (Figure 5.9) shows light particles around a darker particle. The elemental maps shown in Figure 5.9 for Mg (middle) and Zr (right), show that Mg can be found in all the particles shown. However, the darker particle shown in the middle of the back-scattered micrograph on the left (Figure 5.9), has a higher concentration of Mg in comparison to the particles surrounding it. The elemental map of Zr (on the right in Figure 5.9) shows that Zr can only be observed in the light particles as shown in the back-scattered electron micrograph on the left (Figure 5.9). The particles surrounding the particle in the centre, thus contain both Mg and Zr, while the particle in the centre does not contain Zr. This fact is confirmed by the back-scattered SEM image where the darker-coloured particle is typical of a lack of heavier element such as Zr>Mg.

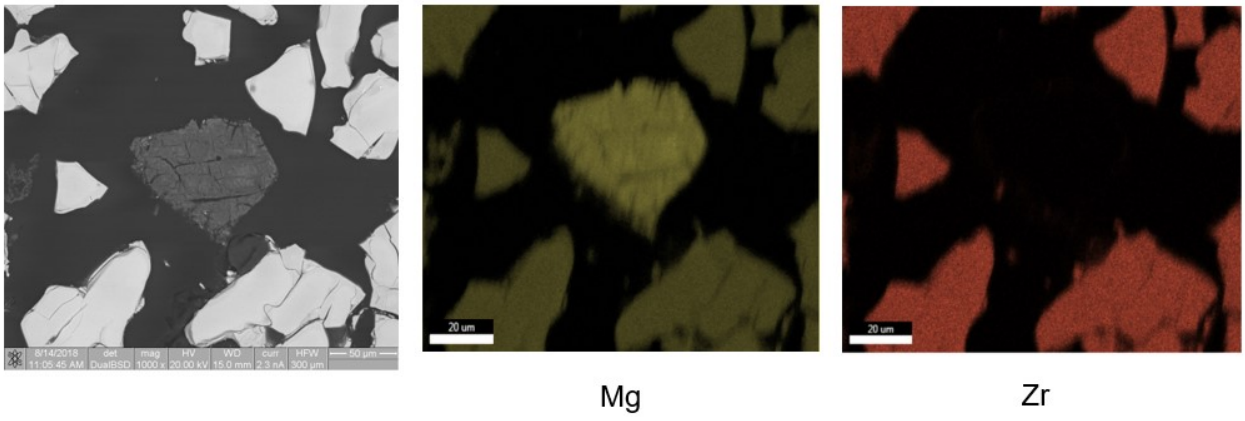

Figure 5.9: Back-scattered electron micrograph of the cross-section of S900-1h-5 (left), with elemental mapping of Mg (middle) and Zr (right)

XRD analysis indicated that the only phases present in the XRD pattern of S900-1h-5 are ZrC and MgO, it is thus thought that the Zr observed in Figure 5.9 is attributed to ZrC, while the Mg observed in Figure 5.9 is attributed to MgO. Correlating the XRD results to the EDS results, the particles in Figure 5.9 are thus thought to be MgO as the centre particle[l] with a solid solution of ZrC and MgO in the particles surrounding the centre particle, confirming that the Mg acted as an

[k] The sample preparation for this sample was the same as the sample preparation for SEM analysis described in Chapter 4.

[l] Crystallites on the inside of the tube furnace were observed after each reaction and the crystallites were more when more Mg was used during the reaction. Due to the volatility of Mg at the reaction temperatures used, the crystallites are believed to be MgO. It is also possible that the observed MgO particle in Figure 5.9 could be a piece of a crystallite that accidentally fell into the open crucible when the crucible was removed from the tube furnace.

“oxygen-getter” during magnesiothermic reduction of the ZrO_2 in the pyrolysis product (900 °C) of the Pechini method.

5.5 Conclusions

The synthesis of ZrC powders *via* magnesiothermic reduction of zirconia was achieved at lower temperatures compared to the temperatures needed for carbothermal reduction. XRD investigations showed a weight to weight mixture of ZrO_2+C mixture and Mg powder heated to 900 °C yields 56.0% ZrC and 44.0% MgO after a holding time of 1 hour and by increasing the holding time the crystallinity of the ZrC and MgO is also improved. Magnesium acts as an “oxygen-getter” during the synthesis of ZrC *via* magnesiothermic reduction reaction. The Pechini method should thus be used in conjunction with magnesiothermic reduction to obtain ZrC.

5.6 References

BRUKER, A.X.S. 2009. TOPAS, Version 4.2. Karlsruhe, Germany,: Bruker AXS.

CHU, A., QIN, M., RAFI UD, D., ZHANG, L., LU, H., JIA, B. and QU, X. 2013. Carbothermal synthesis of ZrC powders using a combustion synthesis precursor. *International Journal of Refractory Metals and Hard Materials,* 36**,** 204-210.

DAVOODI, D., HASSANZADEH-TABRIZI, S., EMAMI, A.H. and SALAHSHOUR, S. 2015. A low temperature mechanochemical synthesis of nanostructured ZrC powder by a magnesiothermic reaction. *Ceramics International,* 41**,** 8397-8401.

JI, Z., YE, L., TAO, X., LI, H., QIU, W., CAI, T., JIANG, Y. and ZHAO, T. 2012. Synthesis of ordered mesoporous ZrC/C nanocomposite via magnesiothermic reduction at low temperature. *Materials Letters,* 71**,** 88-90.

KHANGKHAMANO, M. 2014. *Novel Molten Salt Synthesis of ZrB_2 and ZrC powders and Molten Salt Synthesis of Novel TiC.* Doctor of Philosophy in Engineering Thesis, University of Exeter.

KOBAYASHI, H., SHIMOSAKA, K., SAITOH, M. and MITAMURA, T. 1993. Low-Temperature Synthesis of ZrC Powder by Cyclic Reaction of Mg in ZrO_2–Mg–CH_4. *Journal of the American Ceramic Society,* 76**,** 2389-2392.

LI, J., FU, Z.Y., WANG, W.M., WANG, H., LEE, S.H. and NIIHARA, K. 2010. Preparation of ZrC by self-propagating high-temperature synthesis. *Ceramics International,* 36**,** 1681-1686.

YAN, Y., HUANG, Z., LIU, X. and JIANG, D. 2007. Carbothermal synthesis of ultra-fine zirconium carbide powders using inorganic precursors via sol–gel method. *Journal of Sol-Gel Science and Technology,* 44**,** 81-85.

CHAPTER 6 CONCLUSIONS AND RECOMMENDATIONS

6.1 Conclusions

This thesis reviewed the crystal chemistry and phase chemistry of ZrC in an effort to gain insight into the modern understanding of the atomic structure of ZrC and the fundamental parameters of formation. Standard fabrication methods were reviewed in order to *find and apply* a method to synthesize and characterize *stoichiometric* and *non-stoichiometric* ZrC powders. Solution-based processing method i.e. the Pechini method was chosen on the grounds that this method offered the best way to synthesize stoichiometric and non-stoichiometric ZrC for the subsequent study of the physical properties.

An overview of some of the properties of ZrC was presented in Chapter 2. The crystal structure and phase chemistry as well as the mechanical and thermal properties of ZrC, as a function of the stoichiometry of ZrC, were summarised. It was found that the stoichiometry of ZrC greatly influences these parameters. The review found that a thorough understanding of the thermodynamic, mechanical, and heat transport properties of ZrC is limited and that a careful and systematic detailed characterization of ZrC, as a function of stoichiometry, with emphasis on resulting microstructures, is required. Furthermore, the optimum ZrC to be used for the coating of fuel rods, should have fracture toughness and hardness close to 1.40 to 2.74 MPa $m^{1/2}$ and 27 to 35 GPa respectively.

Chapter 3 reviewed the various synthesis routes of the formation of a well ordered ZrC that can be used in the nuclear industry and the following conclusions have been made:

1. The solid state reaction route uses long processing times and high reaction temperatures which results in this process to be not economical due to the high cost of running facilities at high temperature for extended periods. The particles are also more likely to be contaminated with oxygen and possible contamination from milling media used to create fine particles. Another drawback is that an additional processing method is needed to apply the ZrC powder to the fuel rods.

2. Vapour phase synthesis of ZrC through the CVD process does fabricate the purest phase ZrC, but the processing method uses complicated reagents and processing set-ups. The scale of a fuel rod is also orders of magnitude larger than the TRISO fuel kernels being coated *via* this process.

3. The literature shows solution-based synthesis routes to hold the greatest advantage regarding control of the stoichiometry of ZrC. The literature review showed that synthesis

of ZrC (with various stoichiometries) was achieved at temperatures from 1200 °C up to 1800 °C, but these ZrC powders were always contaminated with small amounts of oxygen, leading to the formation of zirconium oxycarbides.

However, the Pechini method does not consider the probable oxygen impurity which is one of the drawbacks of the solution-based methods with subsequent carbothermal reduction to synthesize ZrC. The Pechini method is a simple and benign method for precursor preparation *via* the formation of an *in situ* polymerizable complex, *in situ* charring and *in situ* reaction at 1300 °C.

In Chapter 4, a soluble polymeric precursor was synthesized *via* the Pechini method and the formation of ZrC powders *via* the carbothermal reduction reaction of the dried gels of this method was investigated. The pyrolysis of the precursor in an argon atmosphere under reduced pressure converts to intimately mixed *t*-ZrO_2 and amorphous carbon. The formation of ZrC starts at temperatures around 1200 °C and nears completion at 1500 °C, according to XRD analysis. Afterwards, XPS analysis showed that the synthesized ZrC powders fabricated by this study are in close agreement to ZrC powders available commercially.

The stoichiometries of the synthesized ZrC powders were determined by coupling XRD and IGF analyses. The amounts of carbon and oxygen in each sample revealed that even samples with an excess amount of initial carbon formed ZrC powders with a stoichiometry of $ZrC_{0.96}O_{0.04}$. The best results for ZrC synthesis *via* the Pechini method, were achieved after carbothermal reduction at 1300 °C for 2 hours resulting in ZrC powders with a stoichiometry of $ZrC_{0.96}O_{0.04}$.

A SEM image of the cross-section of the 1500 °C sample showed that the ZrC particles grow according to the mechanism of carbothermal reduction discussed. The mechanism also shows that the formation of ZrC is not fully equilibrated after 2 hours at 1500 °C.

Based on the stoichiometry results and the mechanism of carbothermal reduction presented in Chapter 4, a process to remove the oxygen from the ZrC powders was investigated. Magnesiothermic reduction of zirconia and carbon results in ZrC and MgO at lower temperatures, between 700 °C to 900 °C, compared to the higher temperatures needed for carbothermal reduction. XRD investigations showed a weight to weight mixture of ZrO_2+C mixture and Mg powder heated to 900 °C yields 56.0 wt. % ZrC and 44.0 wt. % MgO after a holding time of 1 hour and by increasing the holding time the crystallinity of the ZrC and MgO also improves. Magnesium acts as an “oxygen-getter” during the synthesis of ZrC *via* magnesiothermic reduction reaction. These weight percentages when compared to the theoretical weight percentages calculated for ZrC and MgO (56.15 wt. % ZrC and 43.85 wt. %

MgO) shows a near complete conversion into ZrC and MgO. The Pechini method should thus be used in conjunction with magnesiothermic reduction, instead of carbothermal reduction to obtain ZrC.

Although the aim of this thesis was to synthesise ZrC powders to be used in subsequent studies of the properties of ZrC, pure ZrC powders could not be synthesised due to the high affinity of zirconium to attract oxygen and the resulting formation of zirconium oxycarbide. Experimental work showed after comparison of the d-spacing values of the ZrC data file JCPDS 00-035-0784, with the d-spacing values of S1.00-1500 (as described in Chapter 4), that the stoichiometry of the ZrC used to generate the ZrC data file JCPDS 00 035 0784, is closer to the stoichiometry of S1.00-1500, which was shown in Chapter 4 to be $ZrC_{0.96}O_{0.04}$.

The discrepancy between the known JCPDS entry, JCPDS 00-035-0784, for ZrC and the experiments conducted within this thesis shows a clear gap in the existing XRD data for ZrC and the work presented in this thesis. This work concluded by showing the presence of ZrC_xO_y in the accepted XRD data for ZrC and that the existence of pure ZrC is not likely to occur.

6.2 Recommendations

- The magnesiothermic reduction of ZrO_2 in the pyrolysed gels of the Pechini method should be further investigated with regards to the quantitative chemical analysis of the resulting ZrC powders to determine the stoichiometry of these ZrC powders.

- When the d-spacing values in the XRD patterns of the synthesized samples obtained in Chapter 4 and the d-spacing values of the ZrC JCPDS 00-035-0784 data file are compared (comparison tables are available in Chapter 4), it is recommended that JCPDS 00-035-0784, should rather be considered as a XRD reference for zirconium oxycarbide instead of ZrC (1/1).

APPENDIX A ZIRCONIUM-CARBON PHASE DIAGRAM

Enlargement of Figure 2.2

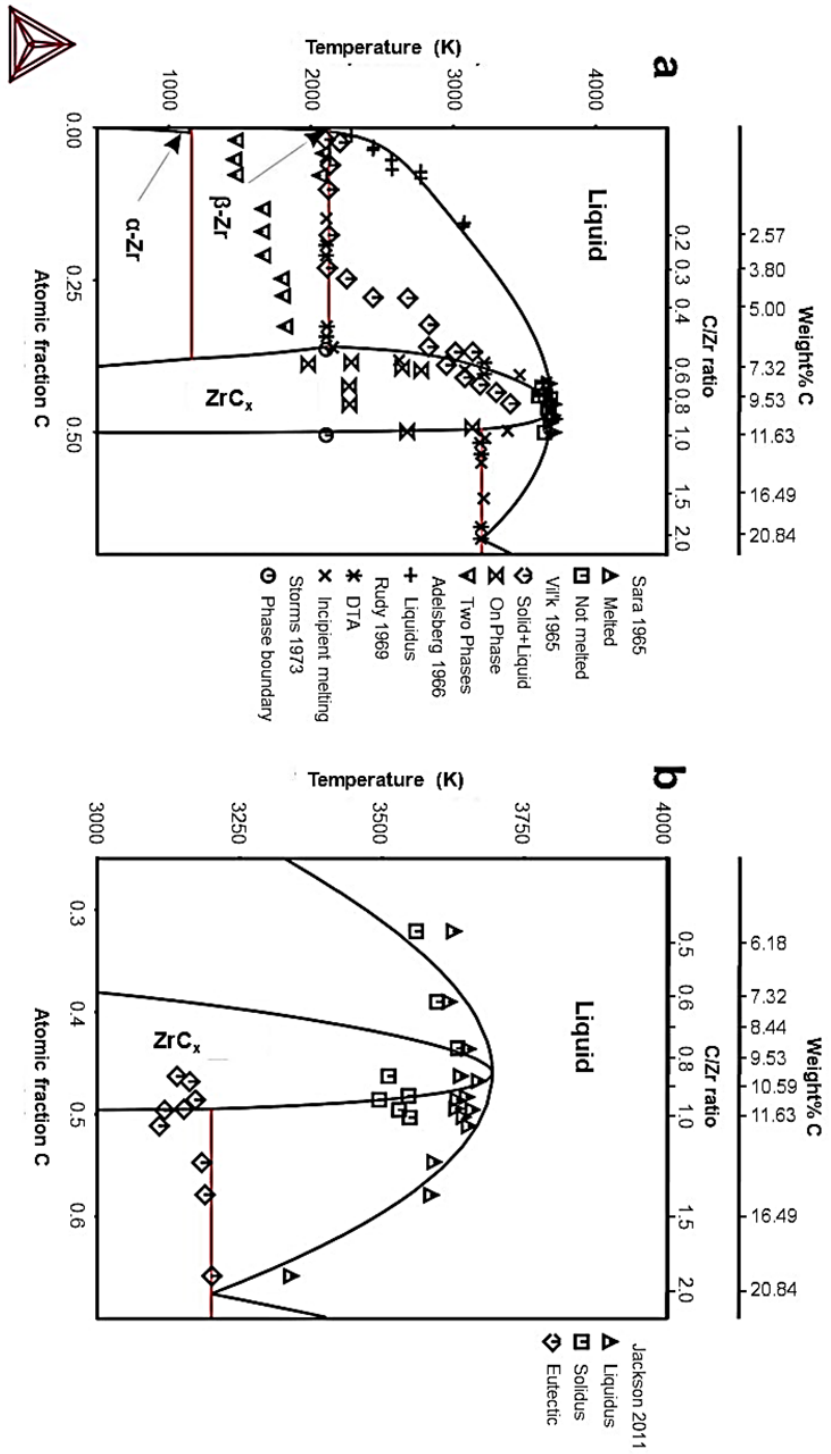

APPENDIX B BASICS OF SOLUTION-BASED TECHNIQUES

B.1 Introduction

Since the solution-based synthesis of ZrC was identified as the optimal synthesis route for the control of the stoichiometry of ZrC_x during synthesis and the application of ZrC coating on nuclear fuel rods, it would be advisable to get a better understanding of the solution-based technique.

In this section, the basic principles of the sol-gel technique will be briefly discussed along with some of the modifications to the traditional sol-gel technique implemented to improve the handling of precursors and including other metallic species. The discussion will mainly focus on the synthesis of silica and other metal oxides to describe the chemistry involved of each technique, but by changing the metal, the pyrolysis atmosphere and addition of carbon, nitrogen or sulphur to the sol-gel, carbide, nitride or sulphide ceramics can also be synthesized using these techniques.

B.2 Fundamentals of the sol-gel process

The sol-gel process fundamentally used in the production of ceramic materials or inorganic polymers from a liquid phase through the transformation of liquid precursors to a “sol” and thereafter to a network structure, namely a “gel” (Brinker and Scherer, 1990, Danks *et al.*, 2016). The sol-gel process is traditionally referred to as the hydrolysis and condensation of metal alkoxide-based precursors, especially $Si(OC_2H_5)_4$ (tetraethyl orthosilicate) (Cushing *et al.*, 2004), but colloidal or polymeric precursors can also be used to form the sol (Schmidt, 1992). Depending on the precursors, composition and heat-treatment, either amorphous or polycrystalline materials can be obtained from this processing technique. There are three approaches to making sol-gel derived materials (i) destabilisation of a colloidal sol, (ii) hydrolysis and polycondensation of alkoxides, and (iii) coordination of metal cations to an organic polymer network.

B.2.1 “Sol” and “Gel”

Sol: A sol forms during the hydrolysis and condensation of metal alkoxide precursors. More generalised it is a suspension of small but discrete particles remaining dispersed in a liquid

phase (colloidal suspension) to include the *in situ* formation of inorganic polymer particles *via* covalent bonds and also the solvation and ionic crosslinking of biopolymers (Danks *et al.*, 2016).

Gel: This is generally defined as a non-fluid three dimensional network structure that extends through a fluid phase (with a viscosity other than water) with no precipitate (Danks *et al.*, 2016). Gels can be formed in a variety of ways, which can result in different structures from the same set of precursors with only small changes to the manufacturing conditions. Flory (1974) grouped gels into four types according to their structure: (i) ordered lamellar gels e.g. surfactant mesophases or clays, (ii) covalent polymer networks, (iii) networks of physically aggregated polymers e.g. hydrogels formed *via* helical junctions, and (iv) particulate disordered gels e.g. aggregated globular proteins, fibrillar or reticular precipitates. However, the different types of gels used for the preparation of inorganic solids from sol-gel chemistry, were classified in a more useful manner by Kakihana (1996). The five types of gel found in sol-gel chemistry are listed in Table B.1, focusing on the type of gel or the structure of the solid network, the bonding nature of the precursors to form the network and the most common precursor type to prepare each network (Kakihana, 1996, Danks *et al.*, 2016).

The gel type in (1) differs from the other gel types in that the solid network is not made from polymerisation but colloidal sol particles. A colloidal gel is not a precipitate of solid particles. Gel type (2) is often considered as the counterpart of gel type (1), because it includes an infinite three dimensional network of metal-oxygen inorganic polymers instead of colloidal particles. The gel derived from colloidal particles is called a “colloidal gel”, whereas the gel derived through the hydrolysis and condensation of metal alkoxides is called a “polymeric gel” (Zelinski and Uhlmann, 1984). Although the gel type (3) forms a viscous liquid of one continuous phase rather than a gel, it is worth mention because processing of this gel type leads to the formation of glassy solids and resins, instead of precipitates, through the control of the hydrolysis equilibria. Gel type (4) involves an organic polymer instead of an inorganic polymer such as gel type (2). The organic polymer used in gel type (4) is a coordinating polymer with an affinity to metal ions. Lastly, gel type (5) combines the process of metal-complex formation and *in situ* formation of an organic polymer.

Table B.1: The five types of gel found in sol-gel chemistry, after Danks *et al.* (2016)

Type of gel	Bonding	Source	Illustration
Type (1): Colloidal (Sen and Chakravorty, 1986)	*Particles* are connected by hydrogen or Van der Waals bonding	Metal oxide or hydroxide sols	
Type (2): Metaloxane polymer (Brinker and Scherer, 1990)	*Inorganic polymers* interconnected *via* covalent or intermolecular bonding	Hydrolysis and condensation of metal alkoxides	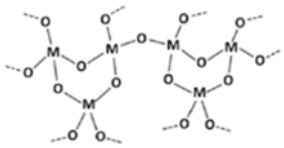
Type (3): Metal complex (Haijun *et al.*, 2004)	*Associated* weakly interconnected *via* Van der Waals or hydrogen bonding	Concentrated metal complex solutions (e.g. amorphous citrate method)	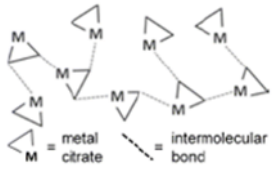
Type (4): Polymer complex I: Coordinating and crosslinking polymers (Sun and Oh, 1996)	*Organic polymers* interconnected *via* coordinate and intermolecular bonding	Coordinating polymer and metal salt solution (typically aqueous)	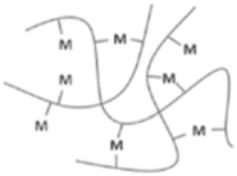
Type (5): Polymer complex II: *In situ* polymerising complex (Pechini method) (Pechini and Adams, 1967)	*Organic polymers* interconnected *via* covalent and coordinate bonding	Polyesterification of an α-hydroxy-carboxylic acid metal complex (e.g. metal citrate) and a polyhydroxy alcohol (e.g. ethylene glycol)	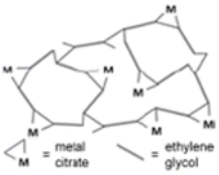

Aside from the precursor preparation to form the sol, the sol-gel process can be characterized by the following key steps:

Step 1: Synthesis of the sol through the formation of stable solutions of an alkoxide or solvated metal precursor. The stable solution forms through hydrolysis and partial condensation of the metal alkoxide.

Step 2: The formation of a gel through polycondensation or polyesterification reactions to form metal-hydroxy-metal or metal-oxo-metal bonds. This results in a dramatic increase in the viscosity of the sol.

Step 3: Syneresis (Aging of the gel), during which the polycondensation continues within the gel network. Contraction of the gel network occurs, resulting in expulsion of the solvent through the gel pores. During this step, Ostwald ripening and phase transformations may also occur. The aging process is critical to gels that have been cast to prevent cracking and this step can exceed seven days.

Step 4: Drying of the gel. Small molecules such as water and other volatile liquids are removed from the gel network. Fundamental changes in the structure of the gel takes place during this step. The gel can either form a xerogel through thermal evaporation of the solvent and the collapse of the porous network or an aerogel if the solvent is removed through supercritical or near supercritical extraction.

Step 5: Calcination of the gel at temperatures up to 800 °C to remove the surface-bound M-OH groups, thereby stabilising the gel against rehydration.

Step 6: Densification and decomposition of the gel at temperatures above 800 °C. During this step the remaining organic species are volatilized and the remaining pores of the gel are collapsed. Dense ceramics and glasses are normally prepared *via* this step.

In-depth descriptions of each step is discussed in the work of Hench and West (1990).

B.2.2 Precursors for the sol-gel process

Although the steps listed above are common to most sol-gel processes, the nature of the specific reactions during hydrolysis and condensation differ substantially between the different types of possible precursors used. Metal alkoxides are mostly used for sol-gel chemistry, but hydrated metal species as well as organometallic precursors can also be used during sol-gel chemistry's hydrolysis and condensation reactions. The suitability of the various precursors for sol-gel processes depends on (i) how the electronegativity differences between the metal and oxygen affect the M-O bond's ionic character, and (ii) the effect of the electron donating/ withdrawing ability of the alkyl/aryl chain on the stability of the alkoxy groups. These factors influence the relative rate of the hydrolysis and condensation reactions and ultimately direct the gel structure through the degree of polymerisation (Danks *et al.*, 2016).

The partial-charge model, developed by Livage *et al.* (1988), can be used to predict the ionic character of the M-O bond. The partial charge, δ, on an atom, *i*, is given by

$$\delta_i = \frac{(\bar{\chi}-\chi_i^0)}{k\sqrt{\chi_i^0}} \quad \text{(B.1)}$$

where $\bar{\chi}$ is the mean electronegativity of the system, χ_i^0 is the electronegativity of the atom and k is a constant (1.36 in the Pauling scale of electronegativity). $\bar{\chi}$ is given by

$$\bar{\chi} = \frac{\sum_i p_i\sqrt{\chi_i} + kz}{\sum_i\left(p_i/\sqrt{\chi_i}\right)} \quad \text{(B.2)}$$

where p_i is the stoichiometry of atom i, χ_i is the electronegativity of atom i, and z is the net charge of the ionic species.

Charge transfer occurs when two atoms combine, leading to each atom acquiring a partial positive, δ^+, or partial negative, δ^-, charge. The substituent with the largest partial negative charge, δ^-, will act as the nucleophile in nucleophilic substitution reactions (S_N) and nucleophilic addition reactions (A_N). The substituent with the largest partial positive charge, δ^+, will act as the leaving group during S_N reactions, which are common reaction mechanisms for hydrolysis and condensation reactions (Brinker and Scherer, 1990). When the nucleophile acquires a partial charge $\delta \geq 0$, the nucleophilic reactions will cease. The calculation of the charge-pH diagram (Figure B.1) can be achieved by using the partial-charge model to determine the magnitude of charge transfer between the water, hydroxo or oxo ligands and the metal, M^{z+} (Brinker and Scherer, 1990). The partial-charge model is also used to determine the mechanism (olation or oxolation) through which the polymer (gel) will form. The structure of the gel is controlled by the olation or oxolation mechanisms (Reynolds, 2007).

B.2.3 Hydrolysis reactions in aqueous solution

Metal salts, MX_n, with n the number of anions, X, which are linked to the metal, M, are the simplest type of precursors used in sol-gel processing. These precursors disperse in water to form solvated complexes $[M(H_2O)_N]^{z+}$, of charge $z+$ and N water molecules coordinated to the metal, M, *via* the electron transfer of the bonding orbitals of water to the empty d-orbitals of the transition metal. The electron transfer weakens the O-H interactions of the bound water, and various degrees of hydrolysis can be induced by varying the pH of the solution (Equation B.3). If the metal is highly reactive, the hydrolysis may take place in a non-aqueous solvent, by controlling the addition of water. Knowing the charge of the metal cation, $z+$, the extent of the hydrolysis reaction can be controlled by pH, as illustrated in Figure B.1. Acidic conditions will

force the equilibrium to the left and favour the formation of hydroxo-ligands or prevent hydrolysis, whereas basic conditions will favour the formation of oxo-ligands.

$$[M(OH_2)]^{z+} \rightleftharpoons [M\text{-}OH]^{(z-1)+} + H^+ \rightleftharpoons [M{=}O]^{(z-2)+} + 2H^+ \quad \text{(B.3)}$$

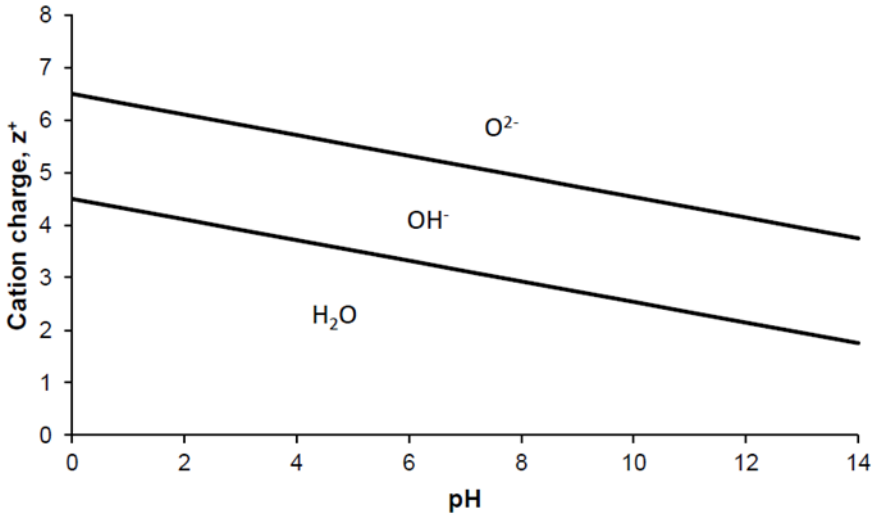

Figure B.1: The charge-pH diagram can be used to determine the extent of the hydrolysis reaction by controlling the pH (after Danks *et al.* (2016))

Destabilisation of a colloidal sol

The colloidal particles (such as metal oxides or hydroxides) in a colloidal sol are aggregated to achieve a colloidal gel. This approach requires a stable intermediate sol as precursor (Pete, 2001). Sols are made kinetically stable by an imposed energy barrier that prevents the particles in suspension from bonding together. A colloidal gel will form when the imposed energy barrier is overcome through temperature or chemical destabilisation of the stable sol.

Temperature destabilisation: When the temperature of the sol increases, the amount of suspending liquid is reduced and thermal agitation increases, resulting in an increase of collisions between particles. Increased collisions of the particles cause the surface hydroxyl groups to undergo condensation reactions, forming the colloidal gel (Pete, 2001). Coagulation also occurs when the sol is frozen. The particles are concentrated between ice crystals and squeezed together with interparticle bonds forming (Iler, 1955, Butcher and Simpson, 1972).

Chemical destabilisation: When the stabilising counter ion is neutralised by the addition of an electrolyte to reduce the electric repulsion between the particles, leading to cross-linking of the small particles to form a gel (Pete, 2001, Sen and Chakravorty, 1986).

B.2.4 Hydrolysis and condensation of alkoxides

The observation that an alkoxide synthesized from $SiCl_4$ started to form a gel when exposed to air by Ebelmen (1846) is the earliest example of the sol-gel process, but the method of preparing oxide films from sol-gel precursors by Geffcken and Berger (1945), Roy (1969) and Dislich (1971) drew the attention to sol-gel processing (Cushing *et al.*, 2004, Brinker and Scherer, 1990). The process of hydrolysis of the silicon alkoxide and then condensation thereof, have since been widely studied and can be carefully tuned to form gels with a variety of different structures. Early transition group metals (such as Ti and Zr) and early p-block elements (such as Al and Si) are the elements mostly used during alkoxide-based sol-gel chemistry (Danks *et al.*, 2016). The hydrolysis and condensation reaction mechanisms of $Si(OR)_4$ (where R = C_nH_{2n+1}, with n = 1,2,3,4) will be discussed as an illustrative example, as the reaction mechanisms are analogous to those for other metal alkoxides.

Depending on the nature of the metal, metal alkoxides can be prepared in different ways; by direct reaction of the metal (alkali metals or lanthanides) with alcohols or, traditionally, by reacting the metal chloride with alcohols (Mazdiyasni and Brown, 1970, Ebelmen, 1846). $Si(OR)_4$ is prepared by reacting $SiCl_4$ with the corresponding alcohol, as illustrated in Equation B.4:

$$SiCl_4 + 4ROH \rightarrow Si(OR)_4 + 4HCl \qquad (B.4)$$

Understanding the central hydrolysis and condensation reactions involved, is an important part of sol-gel chemistry of alkoxides. Process parameters such as the nature of the alkoxide R-group, the ratio of alkoxide to water and the presence and concentration of a catalyst strongly affect the hydrolysis and condensation reactions. The sol-gel chemistry of silica in the neutral reaction is very slow, thus the reactions are typically driven by either acid or base catalysis. This has important consequences for the structure of the resulting gel network, due to the relative rates of hydrolysis and condensation reactions. During hydrolysis an alkoxy group is replaced by a hydroxy group in both acid (Scheme B.1) and base (Scheme B.2) catalysed systems. These reactions are in both cases bimolecular nucleophilic substitution (S_N2) reactions with a pentacoordinate transition state of Si.

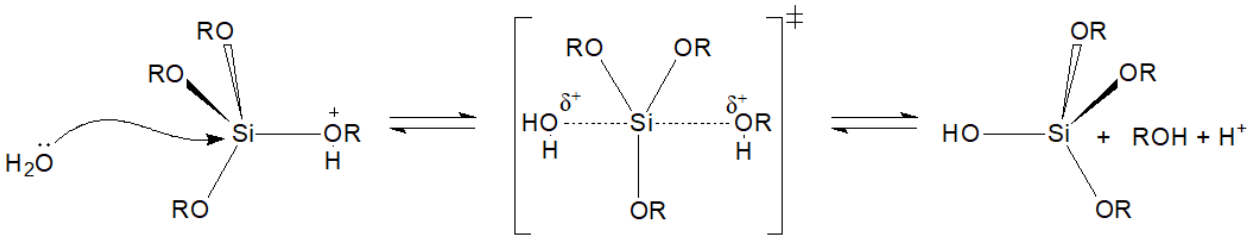

Scheme B.1: Acid catalysed hydrolysis of $Si(OR)_4$

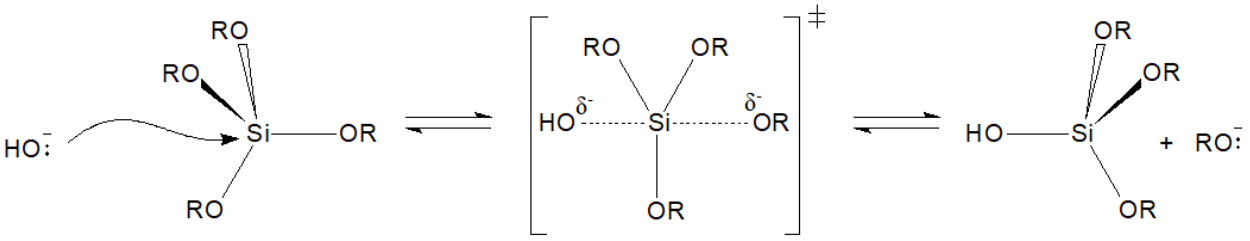

Scheme B.2: Base catalysed hydrolysis of $Si(OR)_4$

More than one alkoxy group may be substituted, depending on the conditions and the Si/H_2O ratio:

$$Si(OR)_4 + xH2O \rightarrow Si(OR)_{4-x}(OH)_x + xROH \qquad (B.5)$$

Variation and control of *x* in Equation B.5 leads to changes in the morphology and structure of the resulting gel (Brinker, 1988).

Condensation occurs when the O-H bonds are weakened by the relatively high electronegativity of Si. The condensation of $Si(OR)_{4-x}(OH)_x$ follows a similar pattern to hydrolysis, being either catalysed by an acid (Scheme B.3) or a base (Scheme B.4) resulting in siloxane (≡Si-O-Si≡) bonds (or for other metals, metaloxane bonds).

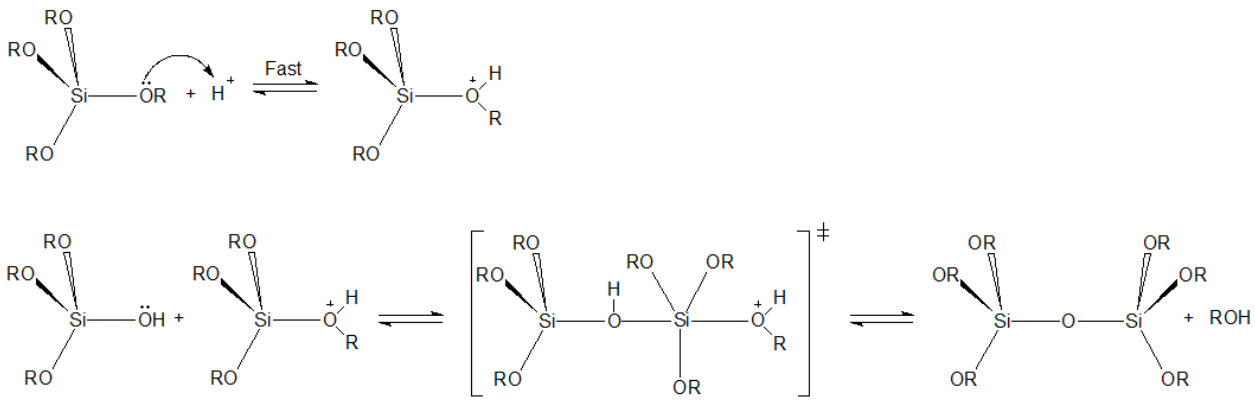

Scheme B.3: Schematic illustration of the acid catalysed condensation of $Si(OR)_{4-x}(OH)_x$ after Cushing *et al.* (2004)

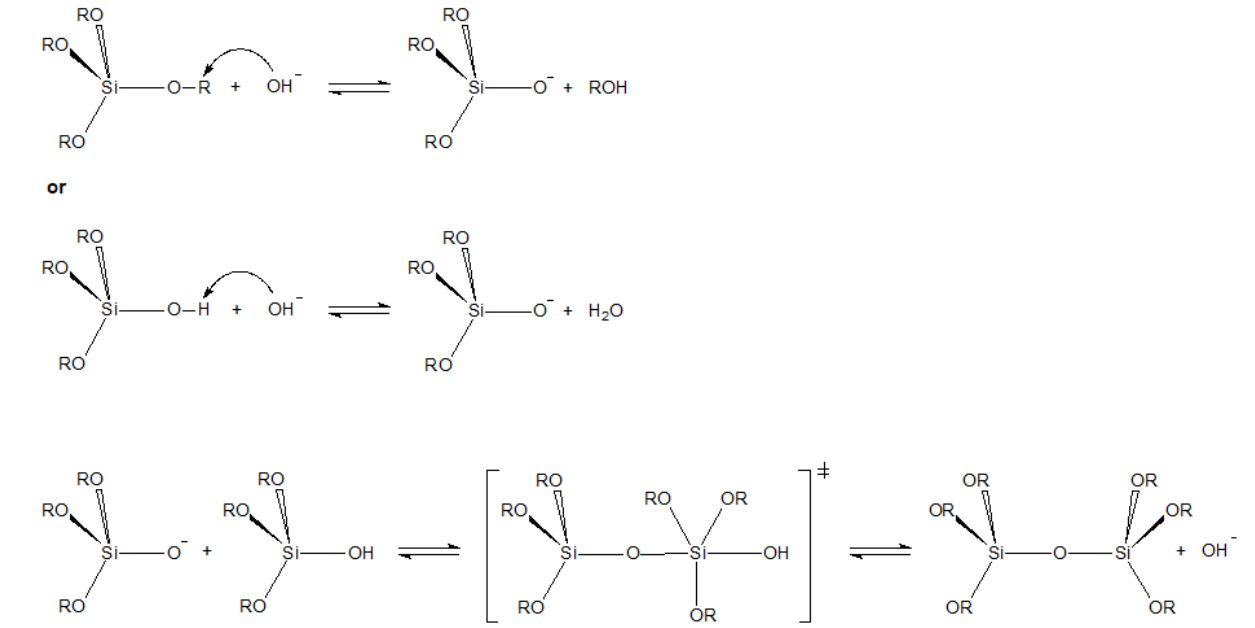

Scheme B.4: Schematic illustration of the base catalysed condensation of $Si(OR)_{4-x}(OH)_x$ after Cushing *et al.* (2004)

The progression of condensation depends on the degree of hydrolysis of the alkoxide precursor (x in $Si(OR)_{4-x}(OH)_x$), as a silanol group is required on at least one silicon centre. The condensation process can be tailored to form dimers, chains or three dimensional structures, because the OH^- group is a marginally better leaving group than the OR^- group during S_N2 reactions. The pH of the reaction mixture also affects the structure of the final gel network. Under acidic conditions (pH < 4), the hydrolysis step is faster than the rate of condensation due to the –OR groups that better stabilise the transition state in Scheme B.1. While the rate of

condensation will decrease with an increase in the –OH group, thus siloxane chains tend to form in the early stages of the polymerisation process and branching and cross-linking of the chains follows in the aging step. In basic conditions hydrolysis steps become progressively faster, leading to $(OH)_3Si\text{-}O\text{-}Si(OH)_3$ products with 6 condensation sites before the first steps of condensation occur. Condensation results in small, highly branched agglomerates in the sol, which crosslink to form a colloidal gel. The effect of pH on the morphology of a gel network is conceptually represented in Figure B.2.

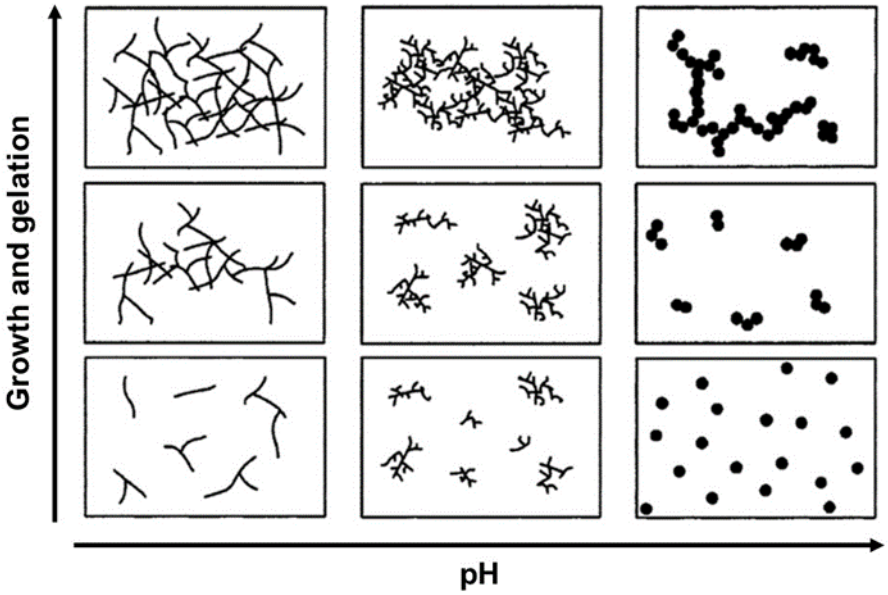

Figure B.2: The effect of pH on the morphology of a gel network, after Danks *et al.* (2016)

Apart from acid and base catalysed systems, the structure of the gel network can be controlled by the presence of solvents to enhance the miscibility of the reagents or to direct the interaction of the solvent with the metal centre. Tuning the water to alkoxide ratio may limit hydrolysis. The size of the alkoxide R-group may cause inductive and steric effects thus impacting the rate of hydrolysis.

The electronegativity of the other metal alkoxides is lower than silicon, especially early transition metals such as titanium and zirconium. The stability and reactivity of these metal alkoxides can be determined using the partial charge model. Partial charges on a $(M(OC_2H_5)_4)$ metal complex for Si, Ti and Zr has been calculated to be +0.32, +0.63 and +0.74 respectively (Cushing *et al.*, 2004). Due to their higher partial charge and the S_N2 nature of hydrolysis, the hydrolysis of Ti and Zr occur at substantially higher rates than Si. This can lead to phase separation during the

synthesis of ternary or quaternary products. Additives which are bidentate or multidentate ligands such as acetylacetone (acac) are added to the metal alkoxide to substitute some of the alkoxide groups and thus limit the hydrolysis reaction and can also lead to less crosslinking in the final gel.

B.2.5 Metal complexes

Hydrolysis and condensation of metal salts are usually rapid, leading to agglomeration of the hydrolysed metals followed by their precipitation as either amorphous oxides or hydroxides of the metal or otherwise the original metal salt forms after heat treatment of the metal salt solution. To avoid the uncontrolled formation of the metal oxide or metal salt, small molecules have been employed to create stable aqueous metal complexes and structures that resemble "gels" more closely. In the case of hydrated acidic salts dissolved in an organic solvent such as ethanol, an epoxide (propylene oxide or epichlorohydrin), acts as a slow proton scavenger, to slowly replace water ligands with hydroxo-ligands. Condensation reactions proceed slowly to form a gel monolith (Gash *et al.*, 2001, Pierre, 2007).

Small molecules such as carboxylic acids, chelate with the dissolved metals to form metal-chelates and change the hydrolysis equilibria by making hydrolysis less favourable. Removal of the solvent from metal-chelates results in resins or glassy solids rather than precipitates (Danks *et al.*, 2016). Heat treatment of these resins or glassy solids forms powders or nanostructures of a wide range of metal oxides/ nitrides/ carbides. One of the most used small molecules is citric acid. Citric acid has three carboxylic acid moieties that are able to dissociate in water. Depending on the pH of the solution, the homogeneity and stability of the metal citrate solution can be controlled. A viscous solution or gel forms upon heating the solution of citric acid and metal salts (mainly nitrates). Other small molecules with carboxylic acid moieties such as EDTA (ethylene-diaminetetraacetic acid), tartaric acid, glycolic acid and oxalic acid have also been employed in stabilising metal salts for sol-gel synthesis (Danks *et al.*, 2016).

B.2.6 Polymers

Considering the definition of a gel, and the formation and structure of polymers, it makes sense that polymers can also be used in sol-gel processes. Functional groups on many polymers can act as chelation sites to interact with metal ions. Synthetic polymers such as polyvinyl alcohol (Sun and Oh, 1996), polyethylene glycol (Lukić *et al.*, 2008), polyvinylpyrrolidone (Kandhasamy

et al., 2012), polyacrylonitrile (Garcia-Marquez *et al.*, 2011) and phenol formaldehyde resins (Sacks *et al.*, 2004, Yan *et al.*, 2012) can be used as polymers in sol-gel processes. Biopolymers which include agar, starch, cellulose, alginate, chitin and chitosan (Yan *et al.*, 2013, Danks *et al.*, 2016) are also used in sol-gel processes.

Metal salts (mostly metal nitrates) are dissolved in a suitable solvent and added to a solution of the polymer in the same solvent to form a homogeneous precursor. A gel is formed after heat treatment at moderate temperatures (approximately 80 °C). The metal oxide is obtained after drying of the gel and pyrolysis in a furnace. The polymer backbone also acts as a carbon and nitrogen source during the synthesis of metal carbides and metal nitrides when heated in an inert atmosphere. Polymers have the ability to form superstructures that can be used to control the morphology and particle size in ceramic synthesis. Thin films and fibres are more easily obtained using polymers in sol-gel processes.

B.2.7 Pechini method

The principles of the Pechini method are discussed in Chapter 3.

B.3 Summary

In this chapter the different types of sol-gel processes were reviewed based on the synthesis of metal oxides. However, this study aims to synthesize zirconium carbide. Synthesis of carbides using sol-gel processing, follows the same fundamental methods, but carbide synthesis must be carried out in an inert atmosphere and by addition of a carbon source.

The Pechini method bypasses the requirement that the metals used must form suitable hydroxo complexes, by forming stable complexes of a variety of metals over a wide pH range. The water-soluble metal salts used during the synthesis of a Pechini-type sol are more readily available and easier to work with than metal alkoxides. The Pechini method has the advantage over other sol-gel techniques, to synthesize complicated multicomponent oxides with a homogeneous distribution of elements.

B.4 References

BRINKER, C.J. 1988. Hydrolysis and condensation of silicates: effects on structure. *Journal of Non-Crystalline Solids,* 100**,** 31-50.

BRINKER, C.J. and SCHERER, G.W. 1990. *Sol-gel science: the physics and chemistry of sol-gel processing*, Academic Press.

BUTCHER, H.J. and SIMPSON, E.A. 1972. Platelet silica, its production and uses. US Patent 3681017.

CUSHING, B.L., KOLESNICHENKO, V.L. and O'CONNOR, C.J. 2004. Recent advances in the liquid-phase syntheses of inorganic nanoparticles. *Chemical reviews,* 104**,** 3893-3946.

DANKS, A., HALL, S. and SCHNEPP, Z. 2016. The evolution of 'sol–gel'chemistry as a technique for materials synthesis. *Materials Horizons,* 3**,** 91-112.

DISLICH, H. 1971. Neue wege zu mehrkomponentenoxidgläsern. *Angewandte Chemie,* 83**,** 428-435.

EBELMEN 1846. Untersuchungen über die Verbindungen der Borsäure und Kieselsäure mit Aether. *Justus Liebigs Annalen der Chemie,* 57**,** 319-355.

FLORY, P. 1974. Introductory lecture. *Faraday Discussions of the Chemical Society,* 57**,** 7-18.

GARCIA-MARQUEZ, A., PORTEHAULT, D. and GIORDANO, C. 2011. Chromium nitride and carbide nanofibers: from composites to mesostructures. *Journal of Materials Chemistry,* 21**,** 2136-2143.

GASH, A.E., TILLOTSON, T.M., SATCHER JR, J.H., HRUBESH, L.W. and SIMPSON, R.L. 2001. New sol–gel synthetic route to transition and main-group metal oxide aerogels using inorganic salt precursors. *Journal of Non-Crystalline Solids,* 285**,** 22-28.

GEFFCKEN, W. and BERGER, E. 1945. Method for producing layers on solid objects. US Patent 2366516.

HAIJUN, Z., XIAOLIN, J., YONGJIE, Y., ZHANJIE, L., DAOYUAN, Y. and ZHENZHEN, L. 2004. The effect of the concentration of citric acid and pH values on the preparation of $MgAl_2O_4$ ultrafine powder by citrate sol–gel process. *Materials Research Bulletin,* 39**,** 839-850.

HENCH, L.L. and WEST, J.K. 1990. The sol-gel process. *Chemical reviews,* 90**,** 33-72.

ILER, R.K. 1955. *The colloid chemistry of silica and silicates*, Cornell University Press.

KAKIHANA, M. 1996. Invited review “sol-gel” preparation of high temperature superconducting oxides. *Journal of Sol-Gel Science and Technology,* 6**,** 7-55.

KANDHASAMY, S., PANDEY, A. and MINAKSHI, M. 2012. Polyvinylpyrrolidone assisted sol–gel route LiCo1/3Mn1/3Ni1/3PO4 composite cathode for aqueous rechargeable battery. *Electrochimica Acta,* 60**,** 170-176.

LIVAGE, J., HENRY, M. and SANCHEZ, C. 1988. Sol-gel chemistry of transition metal oxides. *Progress in solid state chemistry,* 18**,** 259-341.

LUKIĆ, S.R., PETROVIĆ, D.M., DRAMIĆANIN, M.D., MITRIĆ, M. and ĐAČANIN, L. 2008. Optical and structural properties of Zn2SiO4:Mn2+ green phosphor nanoparticles obtained by a polymer-assisted sol–gel method. *Scripta Materialia,* 58**,** 655-658.

MAZDIYASNI, K.S. and BROWN, L.M. 1970. Synthesis and some properties of yttrium and lanthanide isopropoxides. *Inorganic Chemistry,* 9**,** 2783-2786.

PECHINI, M. and ADAMS, N. 1967. Method of preparing lead and alkaline earth titanates and niobates and coating method using the same to form a capacitor. US Patent 3330697.

PETE, T.P. 2001. *The processing of silica based ceramic matrix composites using a sol-gel based slurry method*, Potchefstroom University for Christian Higher Education.

PIERRE, A.C. 2007. Sol–Gel Technology. *Kirk-Othmer Encyclopedia of chemical technology.* John Wiley & Sons, Inc.

REYNOLDS, J.G. 2007. Thermodynamic evaluation of a partial charge model assumption for the dissolved silica system. *Silicon Chemistry,* 3**,** 267-269.

ROY, R. 1969. Gel route to homogeneous glass preparation. *Journal of the American Ceramic Society,* 52**,** 344-344.

SACKS, M.D., WANG, C.-A., YANG, Z. and JAIN, A. 2004. Carbothermal reduction synthesis of nanocrystalline zirconium carbide and hafnium carbide powders using solution-derived precursors. *Journal of Materials Science,* 39**,** 6057-6066.

SCHMIDT, H. 1992. Thin films, the chemical processing up to gelation. *Chemistry, Spectroscopy and Applications of Sol-Gel Glasses.* Springer.

SEN, A. and CHAKRAVORTY, D. 1986. Sol-gel route to inorganic material synthesis. *Proc. Ind. Nat. Sc. Acad.,* 52 A**,** 159-175.

SUN, Y.-K. and OH, I.-H. 1996. Preparation of Ultrafine YBa2Cu3O7-x Superconductor Powders by the Poly(vinyl alcohol)-Assisted Sol−Gel Method. *Industrial & Engineering Chemistry Research,* 35**,** 4296-4300.

YAN, C., LIU, R., CAO, Y., ZHANG, C. and ZHANG, D. 2012. Carbothermal Synthesis of Submicrometer Zirconium Carbide from Polyzirconoxane and Phenolic Resin by the Facile One-Pot Reaction. *Journal of the American Ceramic Society,* 95**,** 3366-3369.

YAN, C., LIU, R., CAO, Y., ZHANG, C. and ZHANG, D. 2013. Synthesis of zirconium carbide powders using chitosan as carbon source. *Ceramics International,* 39**,** 3409-3412.

ZELINSKI, B. and UHLMANN, D. 1984. Gel technology in ceramics. *Journal of Physics and Chemistry of Solids,* 45**,** 1069-1090.

APPENDIX C SUPPLEMENTARY DATA

C.1 XPS notations

The observed photoelectrons in XPS are described by means of their quantum numbers. The notation of each energy band is labelled according to the scheme: nl_j, with ***n*** the principal quantum number, ***l*** the quantum number which describes the orbital angular moment of the electron, usually ***l*** is given a letter as shown in the Table C.1:

Table C.1: Notation given to the quantum numbers which describe orbital angular momentum

Value of *l*	Notation
0	s
1	p
2	d
3	f

The XPS peaks of orbitals with an angular momentum quantum number that is greater than 0 (p, d, f), are usually split into two. This is a result of the interaction of the electron angular momentum due to its spin with its orbital angular momentum. The value of spin, ***s***, can be either +1/2 or -1/2. The two angular momenta are added vectorially to produce the quantity ***j*** in the expression nl_j, i.e.,

$$j = |1 + s|.$$

For example: An electron from p orbital can have ***j*** value of 1/2 (1 - s) or 3/2 (1 + s) and electrons from d orbital can have ***j*** values of either 3/2 or 5/2.

Table C.2 gives the relationship between the quantum numbers and XPS notation:

Table C.2: The relationship between the quantum numbers and XPS notation

Quantum numbers				XPS
n	*l*	*s*	*j*	notation
1	0	+1/2, -1/2	1/2	1s
2	0	+1/2, -1/2	1/2	2s
2	1	-1/2	1/2	$2p_{1/2}$
2	1	+1/2	3/2	$2p_{3/2}$
3	0	+1/2, -1/2	1/2	3s
3	1	-1/2	1/2	$3p_{1/2}$
3	1	+1/2	3/2	$3p_{3/2}$
3	2	-1/2	3/2	$3d_{3/2}$
3	2	+1/2	5/2	$3d_{5/2}$

C.2 XPS deconvolutions of ZrC reference sample, S1.00-1400 and S1.00-1500 discussed in Chapter 4.

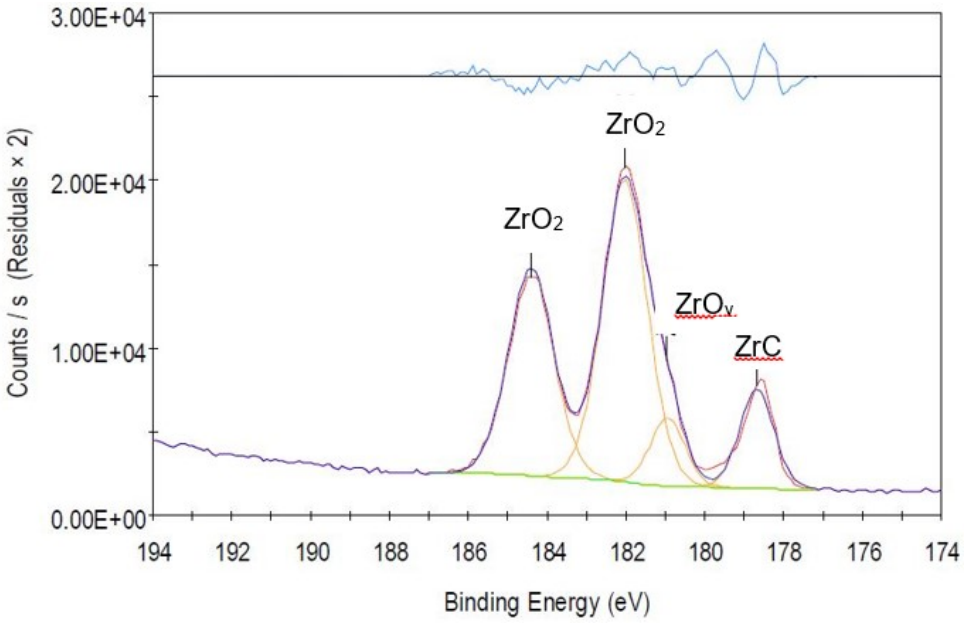

Figure C.1: Deconvolutions of the Zr $3d_{5/2}$ energy band of ZrC reference sample

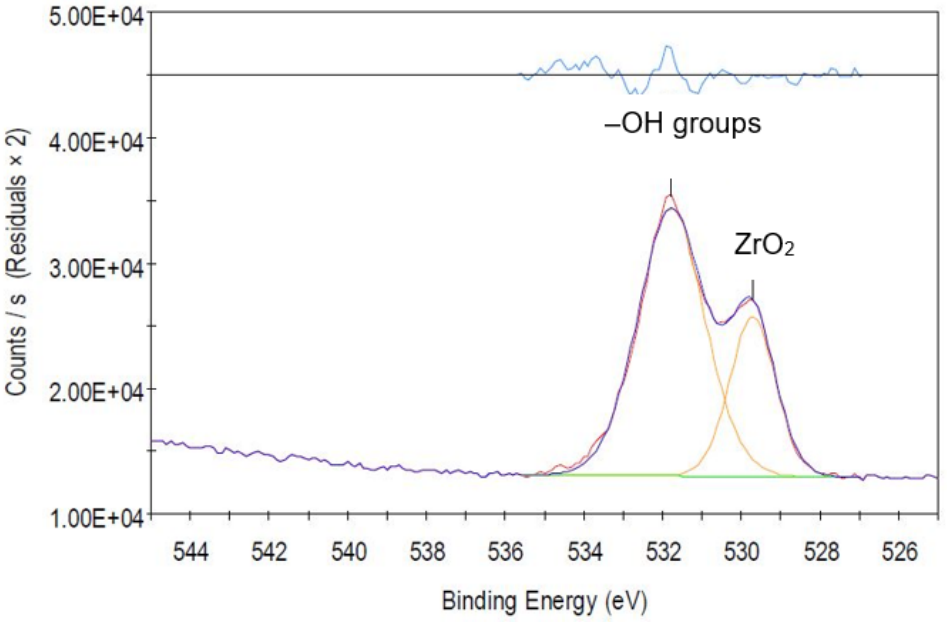

Figure C.2: Deconvolutions of the O 1s energy band of ZrC reference sample

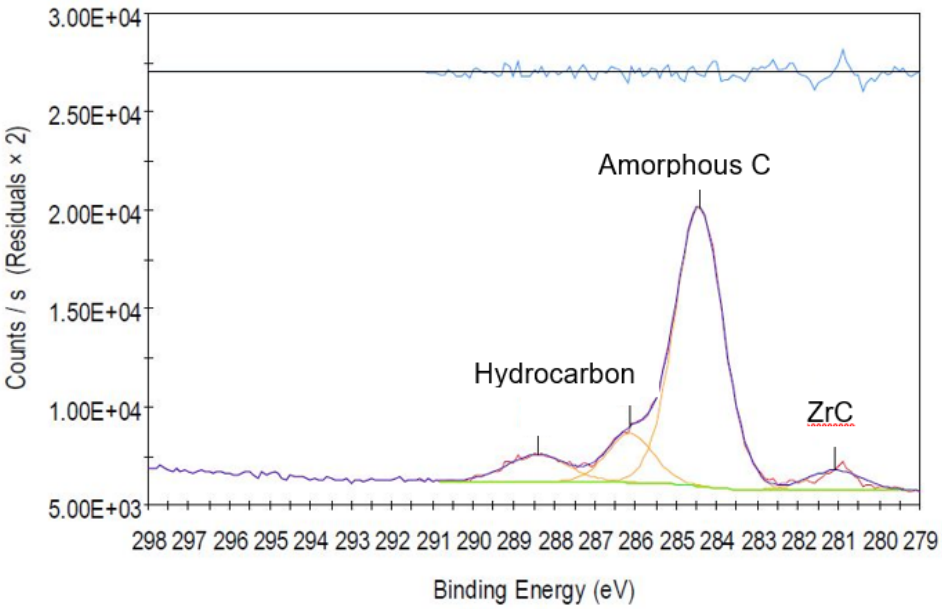

Figure C.3: Deconvolutions of the C 1s energy band of ZrC reference sample

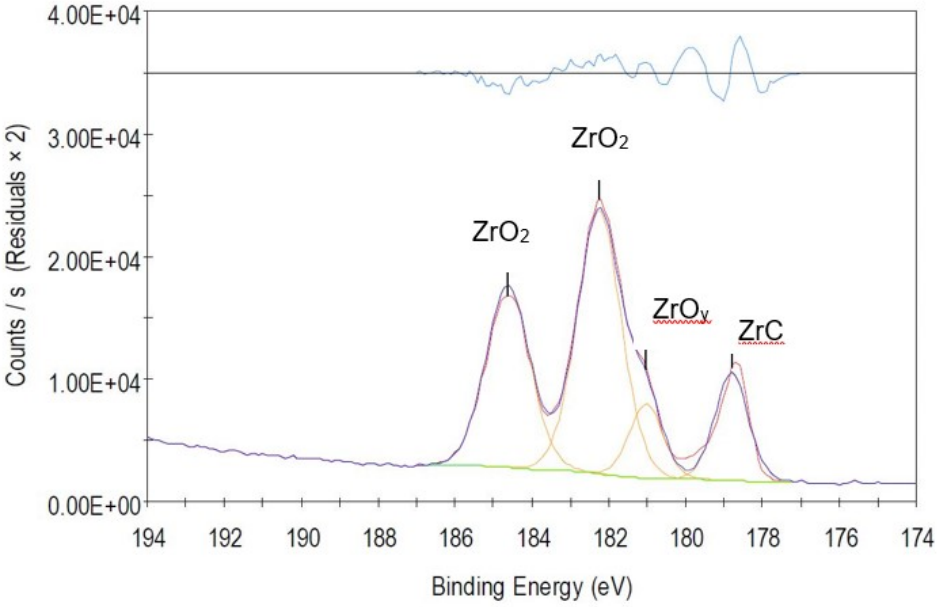

Figure C.4: Deconvolutions of the Zr $3d_{5/2}$ energy band of S1.00-1400

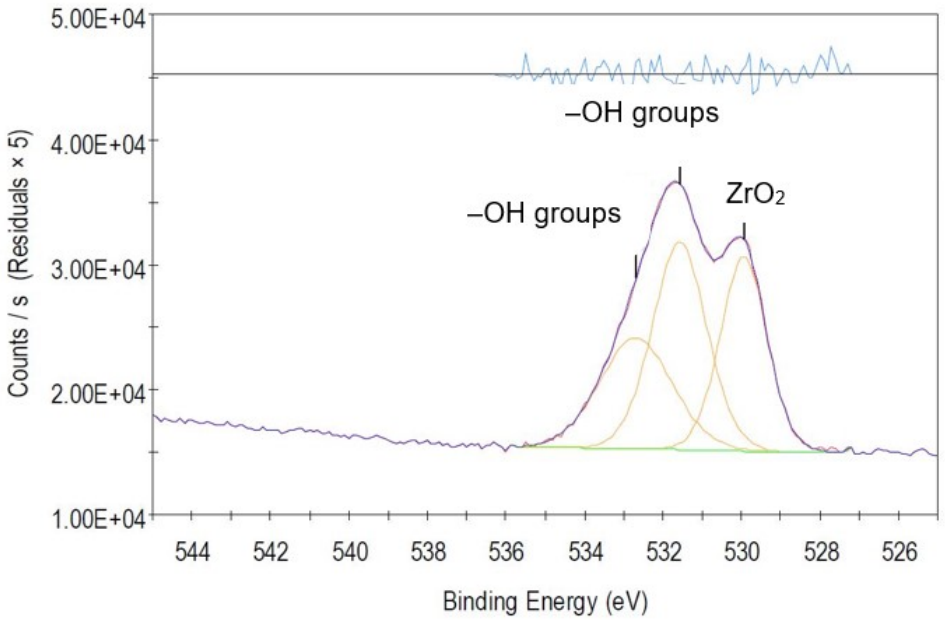

Figure C.5: Deconvolutions of the O 1s energy band of S1.00-1400

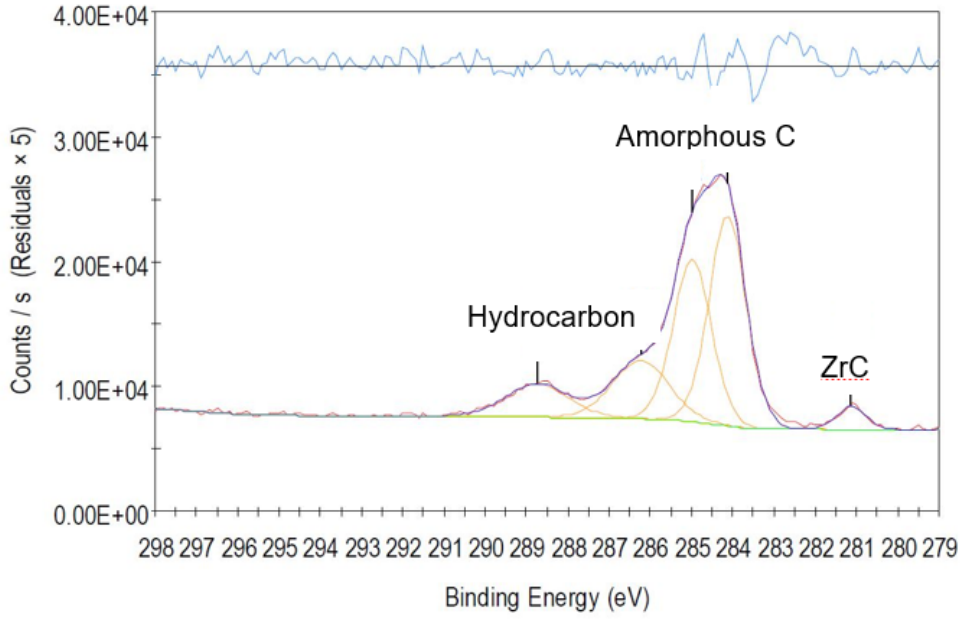

Figure C.6: Deconvolutions of the C 1s energy band of S1.00-1400

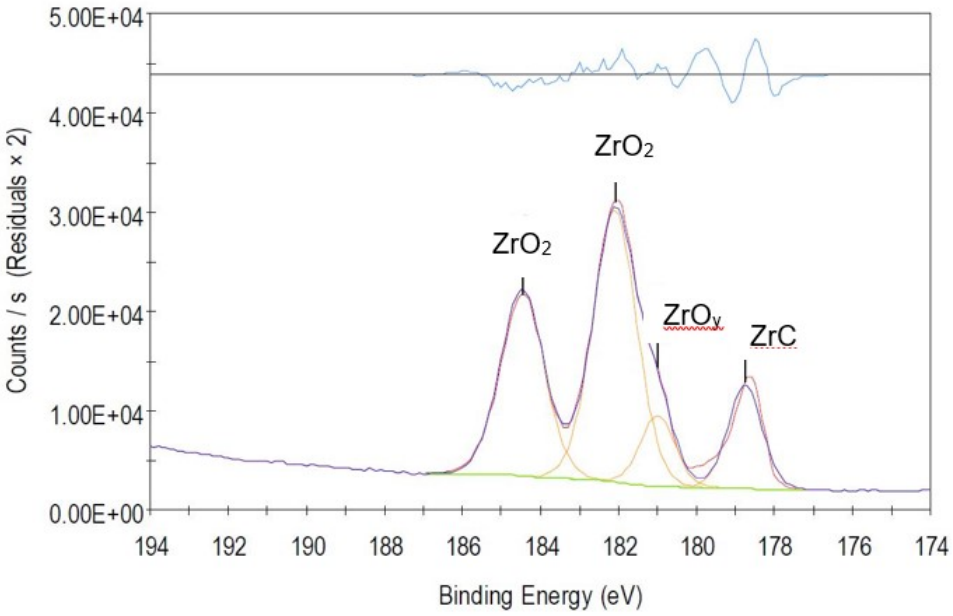

Figure C.7: Deconvolutions of the Zr $3d_{5/2}$ energy band of S1.00-1500

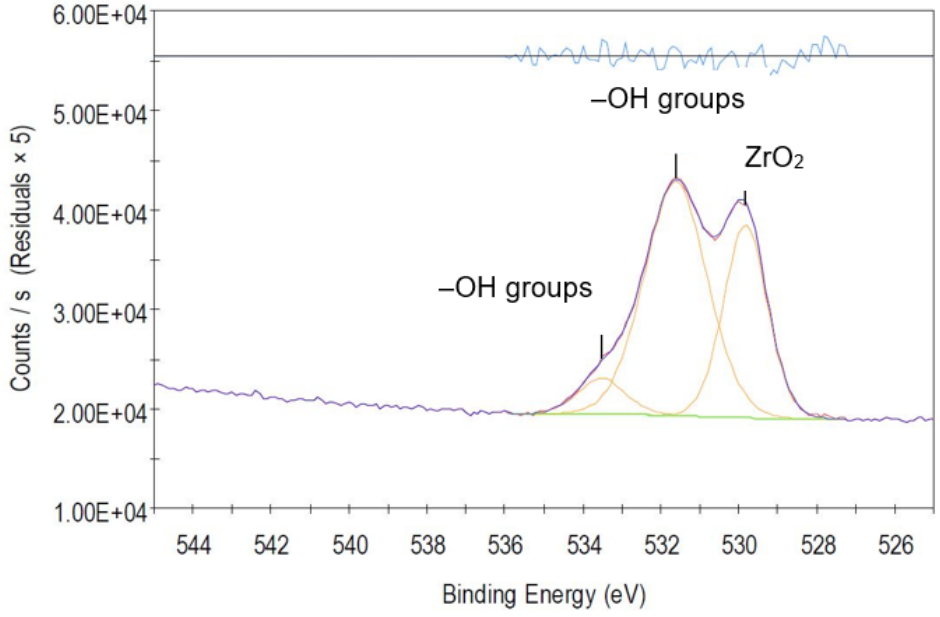

Figure C.8: Deconvolutions of the O 1s energy band of S1.00-1500

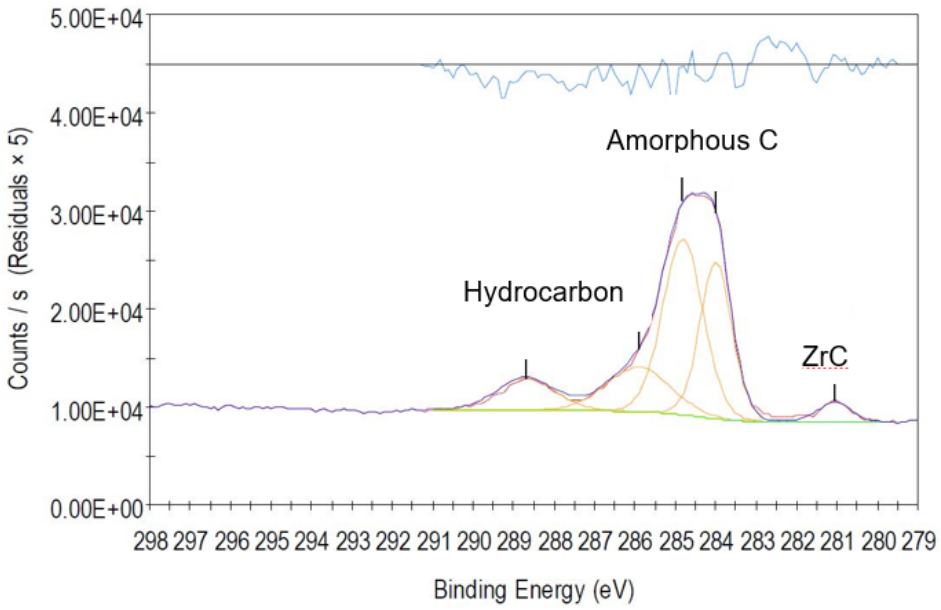

Figure C.9: Deconvolutions of the C 1s energy band of S1.00-1500

C.3 XRD peak lists

The XRD peak lists of the refined XRD patterns of the samples listed in Table 4.2 and discussed in Chapter 4 and an example of the XRD patterns obtained in Chapter 5 are listed hereafter. While all the ZrC peaks are listed, only the 10 most prominent peaks of Al_2O_3 (Corrundum) are listed, while the relative intensity cut off for ZrO_2 (Baddeleyite) was chosen at 1.00 %.

S0.25 – 1300

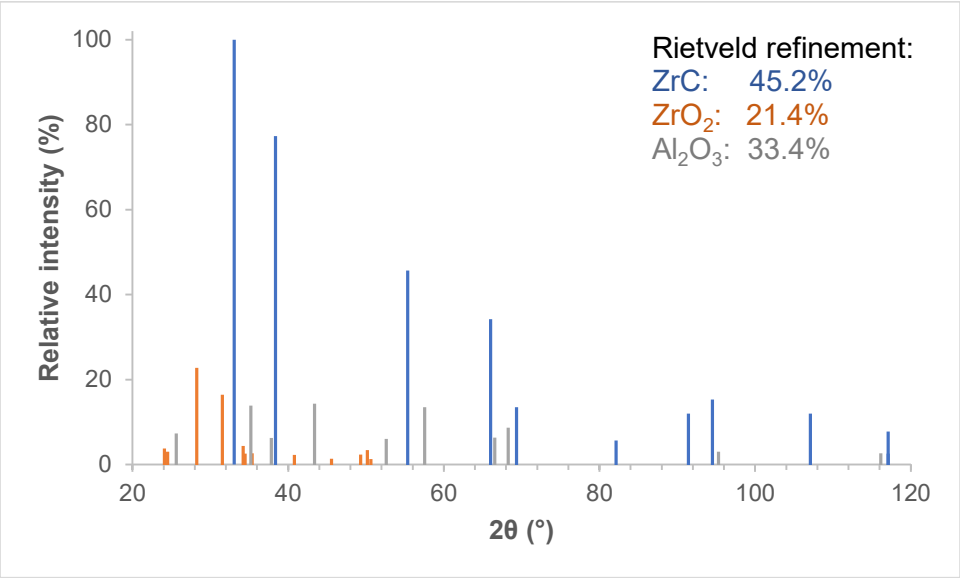

Pos. (°2θ)	Rel. Int. (%)	d-spacing (Å)	h	k	l	Phase Assignment
17.49	1.26	5.06576	0	0	1	Baddeleyite
24.11	3.83	3.68822	1	1	0	Baddeleyite
24.51	3.05	3.62955	1	0	1	Baddeleyite
25.62	7.34	3.47375	0	-2	1	Corundum
28.24	22.80	3.15771	1	1	-1	Baddeleyite
31.53	16.45	2.83544	1	1	1	Baddeleyite
33.08	100.00	2.70564	1	1	1	Zirconium Carbide
34.22	4.40	2.61833	0	2	0	Baddeleyite
34.46	2.56	2.60079	2	0	0	Baddeleyite
35.20	13.92	2.54762	0	4	1	Corundum
35.36	2.68	2.53638	0	0	2	Baddeleyite
37.82	6.30	2.37667	1	0	1	Corundum
38.38	77.32	2.34363	2	0	0	Zirconium Carbide
40.79	2.27	2.21043	1	1	-2	Baddeleyite
43.40	14.34	2.08326	1	3	1	Corundum

Pos. (°2θ)	Rel. Int. (%)	d-spacing (Å)	h	k	l	Phase Assignment
45.58	1.40	1.98852	0	2	-2	Baddeleyite
49.33	2.37	1.84601	2	2	0	Baddeleyite
50.18	3.44	1.81662	2	0	2	Baddeleyite
50.63	1.34	1.80141	2	2	-1	Baddeleyite
52.60	6.06	1.73857	0	-4	2	Corundum
55.37	45.66	1.65786	2	2	0	Zirconium Carbide
57.55	13.52	1.60024	1	6	1	Corundum
66.02	34.24	1.41404	3	1	1	Zirconium Carbide
66.57	6.34	1.40368	1	4	2	Corundum
68.26	8.72	1.37298	0	0	3	Corundum
69.35	13.52	1.35389	2	2	2	Zirconium Carbide
82.13	5.68	1.17265	4	0	0	Zirconium Carbide
91.41	12.00	1.07617	3	3	1	Zirconium Carbide
94.51	15.30	1.04895	4	2	0	Zirconium Carbide
95.30	3.07	1.04232	2	6	2	Corundum
107.10	12.01	0.95763	4	2	2	Zirconium Carbide
116.14	2.68	0.9076	2	4	3	Corundum
117.11	7.80	0.90291	5	1	1	Zirconium Carbide

S0.50 – 1300

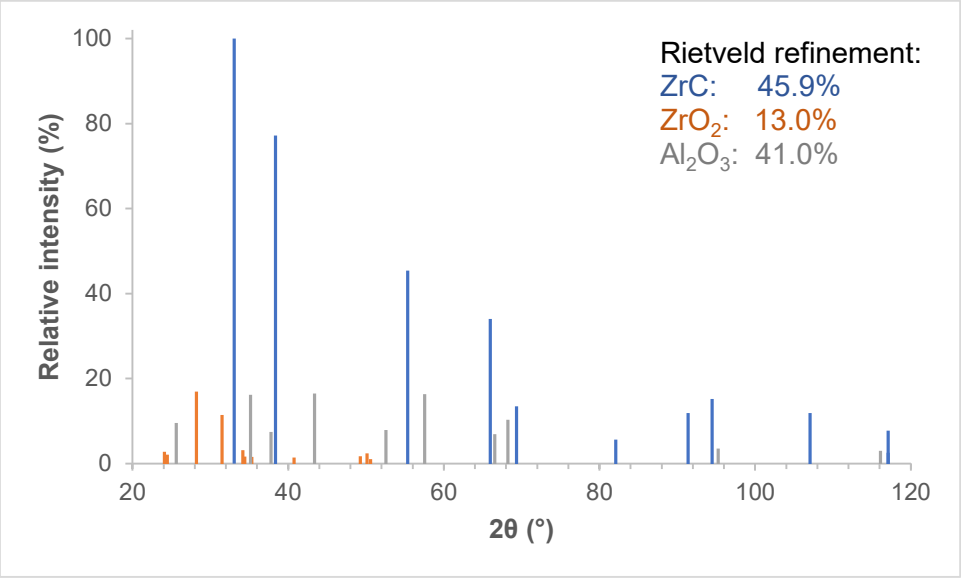

Pos. (°2θ)	Rel. Int. (%)	d-spacing (Å)	h	k	l	Phase Assignment
24.08	2.79	3.69274	1	1	0	Baddeleyite
24.47	2.11	3.63412	1	0	1	Baddeleyite
25.60	9.56	3.47665	0	-2	1	Corundum
28.21	16.93	3.16135	1	1	-1	Baddeleyite
31.50	11.47	2.83802	1	1	1	Baddeleyite
33.06	100.00	2.70753	1	1	1	Zirconium Carbide
34.19	3.16	2.62037	0	2	0	Baddeleyite
34.42	1.65	2.60366	2	0	0	Baddeleyite
35.18	16.15	2.54908	0	4	1	Corundum
35.33	1.60	2.53857	0	0	2	Baddeleyite
37.80	7.42	2.37801	1	0	1	Corundum
38.35	77.20	2.34504	2	0	0	Zirconium Carbide
40.75	1.44	2.21237	1	1	-2	Baddeleyite
43.38	16.45	2.08425	1	3	1	Corundum
49.29	1.72	1.84737	2	2	0	Baddeleyite
50.14	2.38	1.81803	2	0	2	Baddeleyite
50.59	1.05	1.80281	2	2	-1	Baddeleyite
52.58	7.88	1.73922	0	-4	2	Corundum
55.35	45.42	1.65855	2	2	0	Zirconium Carbide
57.53	16.35	1.60076	1	6	1	Corundum
65.99	34.03	1.41453	3	1	1	Zirconium Carbide
66.54	6.88	1.40408	1	4	2	Corundum

Pos. (°2θ)	Rel. Int. (%)	d-spacing (Å)	h	k	l	Phase Assignment
68.23	10.27	1.37338	0	0	3	Corundum
69.33	13.43	1.35434	2	2	2	Zirconium Carbide
82.10	5.64	1.17297	4	0	0	Zirconium Carbide
91.39	11.91	1.07643	3	3	1	Zirconium Carbide
94.48	15.19	1.04919	4	2	0	Zirconium Carbide
95.28	3.52	1.04249	2	6	2	Corundum
107.07	11.90	0.95781	4	2	2	Zirconium Carbide
116.12	3.02	0.90771	2	4	3	Corundum
117.08	7.71	0.90306	5	1	1	Zirconium Carbide

S0.75 – 1300

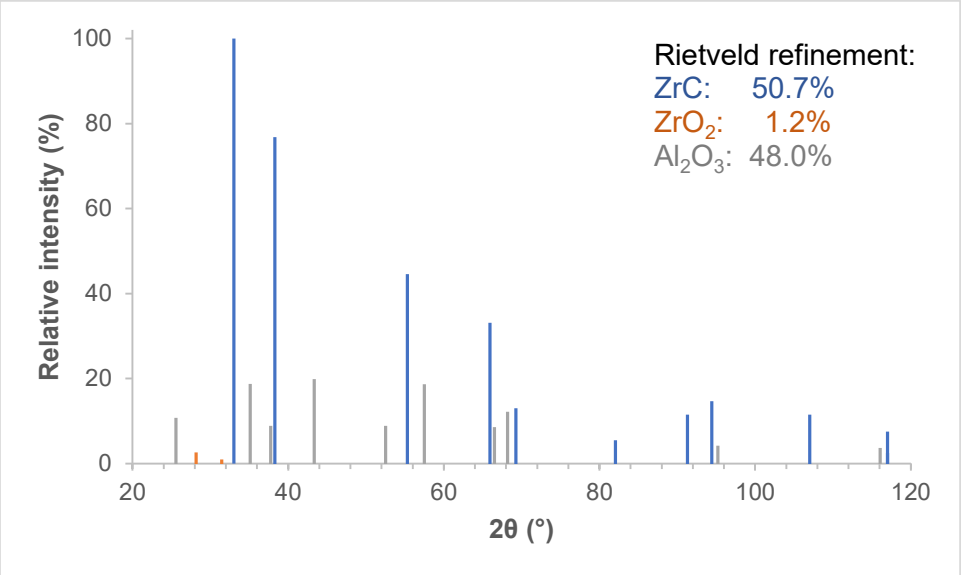

Pos. (°2θ)	Rel. Int. (%)	d-spacing (Å)	h	k	l	Phase Assignment
25.56	10.75	3.48248	0	-2	1	Corundum
28.17	2.61	3.16506	1	1	-1	Baddeleyite
31.45	1.00	2.84202	1	1	1	Baddeleyite
33.01	100.00	2.71137	1	1	1	Zirconium Carbide
35.13	18.73	2.5522	0	4	1	Corundum
37.76	8.84	2.38062	1	0	1	Corundum
38.30	76.81	2.34793	2	0	0	Zirconium Carbide
43.34	19.85	2.08624	1	3	1	Corundum
52.53	8.85	1.74057	0	-4	2	Corundum
55.30	44.54	1.65998	2	2	0	Zirconium Carbide
57.48	18.66	1.6019	1	6	1	Corundum
65.94	33.12	1.41555	3	1	1	Zirconium Carbide
66.50	8.57	1.40489	1	4	2	Corundum
68.19	12.22	1.37413	0	0	3	Corundum
69.27	13.04	1.35527	2	2	2	Zirconium Carbide
82.04	5.45	1.17364	4	0	0	Zirconium Carbide
91.33	11.50	1.07697	3	3	1	Zirconium Carbide
94.42	14.66	1.0497	4	2	0	Zirconium Carbide
95.23	4.24	1.04285	2	6	2	Corundum
107.01	11.52	0.95821	4	2	2	Zirconium Carbide
116.08	3.68	0.90792	2	4	3	Corundum
117.01	7.51	0.90339	5	1	1	Zirconium Carbide

S1.00 – 1300

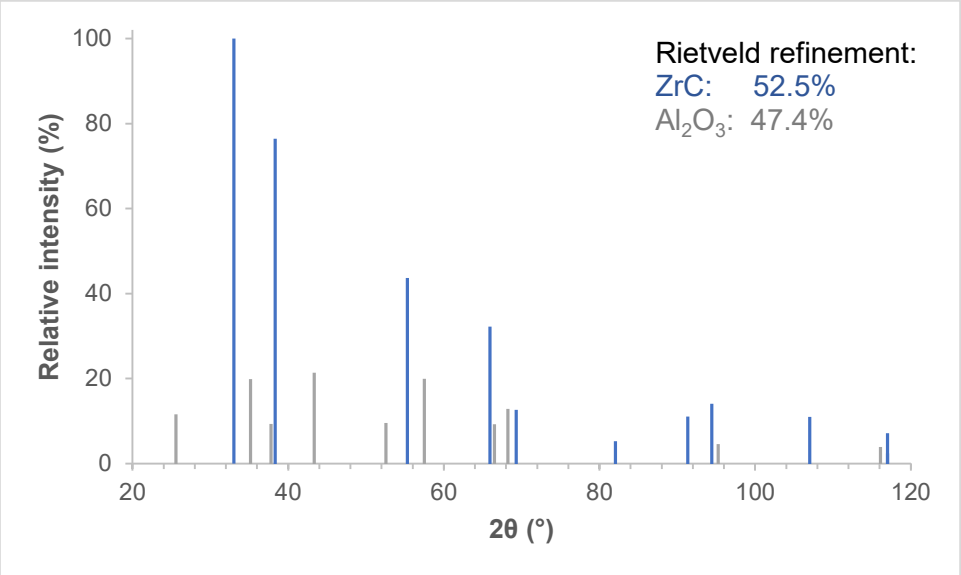

Pos. (°2θ)	Rel. Int. (%)	d-spacing (Å)	h	k	l	Phase Assignment
25.58	11.61	3.47951	0	-2	1	Corundum
33.03	100.00	2.70998	1	1	1	Zirconium Carbide
35.16	19.84	2.55065	0	4	1	Corundum
37.78	9.32	2.37927	1	0	1	Corundum
38.32	76.42	2.34695	2	0	0	Zirconium Carbide
43.36	21.40	2.08523	1	3	1	Corundum
52.56	9.56	1.73989	0	-4	2	Corundum
55.31	43.67	1.6596	2	2	0	Zirconium Carbide
57.51	19.93	1.60133	1	6	1	Corundum
65.95	32.23	1.41533	3	1	1	Zirconium Carbide
66.52	9.22	1.40447	1	4	2	Corundum
68.21	12.89	1.37374	0	0	3	Corundum
69.29	12.67	1.35508	2	2	2	Zirconium Carbide
82.05	5.25	1.17354	4	0	0	Zirconium Carbide
91.33	11.03	1.07692	3	3	1	Zirconium Carbide
94.42	14.04	1.04965	4	2	0	Zirconium Carbide
95.25	4.57	1.04267	2	6	2	Corundum
107.01	10.98	0.95821	4	2	2	Zirconium Carbide
116.10	3.93	0.90781	2	4	3	Corundum
117.00	7.13	0.90341	5	1	1	Zirconium Carbide

S0.25 – 1400

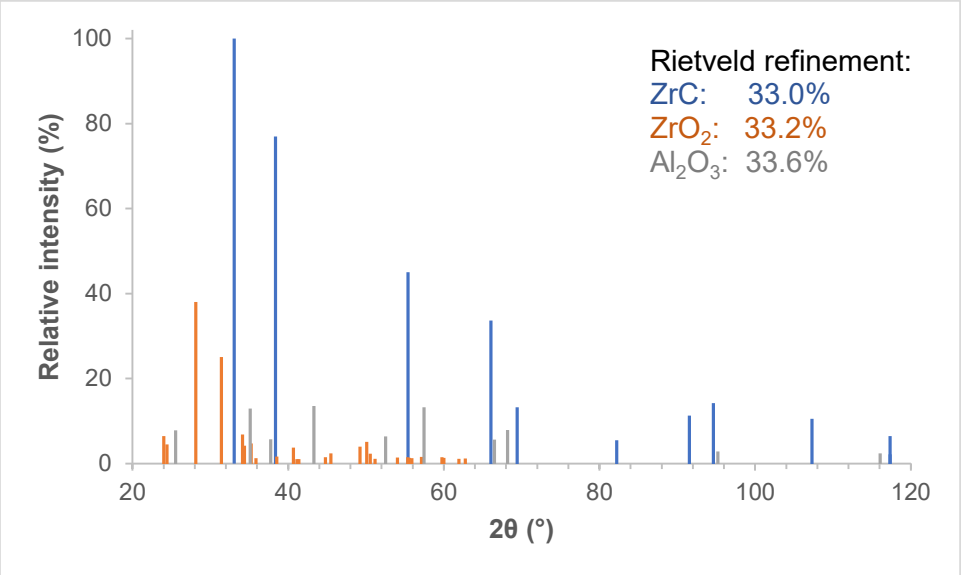

Pos. (°2θ)	Rel. Int. (%)	d-spacing (Å)	h	k	l	Phase Assignment
17.40	2.22	5.09232	0	0	1	Baddeleyite
24.02	6.45	3.70164	1	1	0	Baddeleyite
24.42	4.54	3.64273	1	0	1	Baddeleyite
25.54	7.81	3.48461	0	-2	1	Corundum
28.15	38.05	3.16799	1	1	-1	Baddeleyite
31.43	25.04	2.84370	1	1	1	Baddeleyite
33.06	100.00	2.70747	1	1	1	Zirconium Carbide
34.12	6.83	2.62575	0	2	0	Baddeleyite
34.37	4.17	2.60697	2	0	0	Baddeleyite
35.12	12.93	2.55332	0	4	1	Corundum
35.26	4.70	2.54358	0	0	2	Baddeleyite
35.86	1.26	2.50237	0	2	-1	Baddeleyite
37.74	5.72	2.38159	1	0	1	Corundum
38.36	76.96	2.34439	2	0	0	Zirconium Carbide
38.53	1.63	2.33481	2	1	0	Baddeleyite
40.69	3.76	2.21584	1	1	-2	Baddeleyite
41.11	1.02	2.19394	0	2	1	Baddeleyite
41.35	1.05	2.18159	2	1	-1	Baddeleyite
43.32	13.53	2.08697	1	3	1	Corundum
44.79	1.47	2.02201	1	2	1	Baddeleyite
45.47	2.38	1.99312	0	2	-2	Baddeleyite
49.23	3.98	1.84942	2	2	0	Baddeleyite

Pos. (°2θ)	Rel. Int. (%)	d-spacing (Å)	h	k	l	Phase Assignment
50.08	5.10	1.82001	2	0	2	Baddeleyite
50.53	2.30	1.80472	2	2	-1	Baddeleyite
51.16	1.08	1.78409	2	1	-2	Baddeleyite
52.52	6.42	1.74106	0	-4	2	Corundum
54.04	1.41	1.69548	0	2	2	Baddeleyite
55.34	1.50	1.65880	1	3	0	Baddeleyite
55.40	45.06	1.65725	2	2	0	Zirconium Carbide
55.56	1.31	1.65280	1	3	-1	Baddeleyite
55.88	1.30	1.64399	3	0	1	Baddeleyite
57.11	1.53	1.61139	1	1	-3	Baddeleyite
57.47	13.21	1.60230	1	6	1	Corundum
59.76	1.50	1.54610	3	1	1	Baddeleyite
59.99	1.33	1.54088	0	2	-3	Baddeleyite
61.93	1.11	1.49719	1	3	-2	Baddeleyite
62.78	1.19	1.47887	1	1	3	Baddeleyite
66.06	33.62	1.41315	3	1	1	Zirconium Carbide
66.49	5.65	1.40518	1	4	2	Corundum
68.17	7.91	1.37441	0	0	3	Corundum
69.41	13.23	1.35295	2	2	2	Zirconium Carbide
82.22	5.46	1.17159	4	0	0	Zirconium Carbide
91.53	11.25	1.07506	3	3	1	Zirconium Carbide
94.64	14.19	1.04783	4	2	0	Zirconium Carbide
95.22	2.88	1.04298	2	6	2	Corundum
107.29	10.53	0.95648	4	2	2	Zirconium Carbide
116.07	2.40	0.90800	2	4	3	Corundum
117.35	6.47	0.90174	5	1	1	Zirconium Carbide

S0.50 – 1400

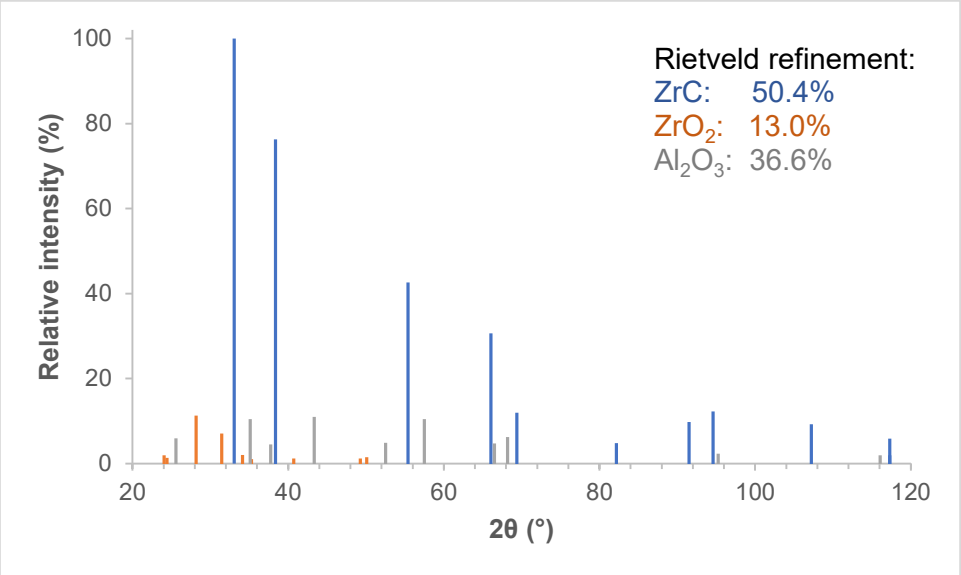

Pos. (°2θ)	Rel. Int. (%)	d-spacing (Å)	h	k	l	Phase Assignment
24.04	1.94	3.69856	1	1	0	Baddeleyite
24.44	1.34	3.63979	1	0	1	Baddeleyite
25.56	5.92	3.48208	0	-2	1	Corundum
28.17	11.25	3.16561	1	1	-1	Baddeleyite
31.46	7.07	2.84166	1	1	1	Baddeleyite
33.06	100.00	2.70721	1	1	1	Zirconium Carbide
34.15	2.01	2.62365	0	2	0	Baddeleyite
35.14	10.43	2.55199	0	4	1	Corundum
35.28	1.05	2.5417	0	0	2	Baddeleyite
37.76	4.53	2.38044	1	0	1	Corundum
38.36	76.28	2.34436	2	0	0	Zirconium Carbide
40.71	1.19	2.21451	1	1	-2	Baddeleyite
43.34	10.97	2.08611	1	3	1	Corundum
49.25	1.20	1.84865	2	2	0	Baddeleyite
50.10	1.51	1.81929	2	0	2	Baddeleyite
52.54	4.87	1.74048	0	-4	2	Corundum
55.39	42.60	1.65749	2	2	0	Zirconium Carbide
57.49	10.43	1.60182	1	6	1	Corundum
66.05	30.67	1.41344	3	1	1	Zirconium Carbide
66.50	4.72	1.40483	1	4	2	Corundum
68.19	6.26	1.37408	0	0	3	Corundum
69.39	11.94	1.35325	2	2	2	Zirconium Carbide

Pos. (°2θ)	Rel. Int. (%)	d-spacing (Å)	h	k	l	Phase Assignment
82.19	4.77	1.1719	4	0	0	Zirconium Carbide
91.50	9.74	1.07539	3	3	1	Zirconium Carbide
94.60	12.29	1.04815	4	2	0	Zirconium Carbide
95.24	2.34	1.04283	2	6	2	Corundum
107.24	9.26	0.9568	4	2	2	Zirconium Carbide
116.08	1.96	0.9079	2	4	3	Corundum
117.28	5.85	0.90207	5	1	1	Zirconium Carbide

S0.75 – 1400

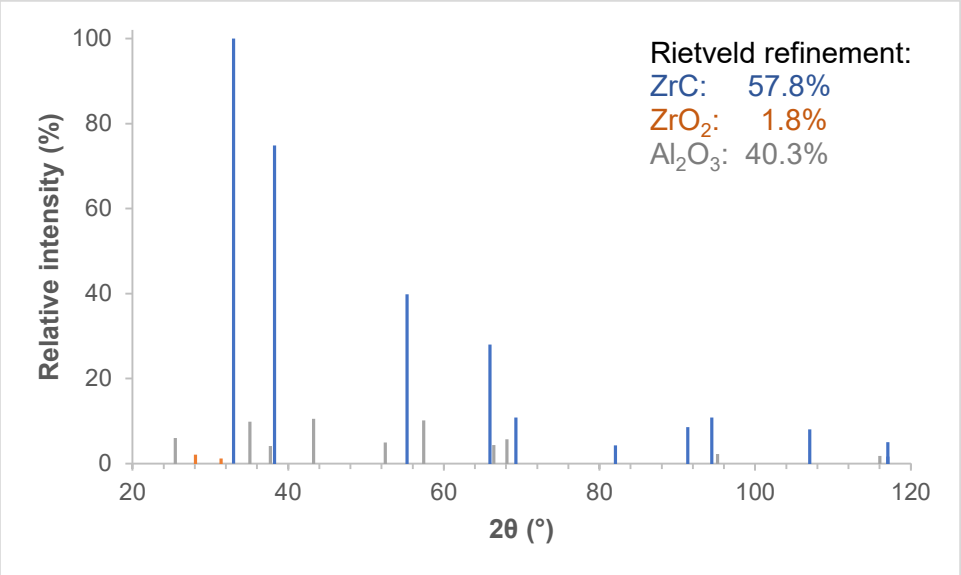

Pos. (°2θ)	Rel. Int. (%)	d-spacing (Å)	h	k	l	Phase Assignment
25.50	6.04	3.49091	0	-2	1	Corundum
28.09	2.06	3.17370	1	1	-1	Baddeleyite
31.39	1.18	2.84757	1	1	1	Baddeleyite
32.97	100.00	2.71475	1	1	1	Zirconium Carbide
35.07	9.88	2.55663	0	4	1	Corundum
37.70	4.13	2.38444	1	0	1	Corundum
38.27	74.86	2.35021	2	0	0	Zirconium Carbide
43.27	10.50	2.08912	1	3	1	Corundum
52.47	4.96	1.74250	0	-4	2	Corundum
55.27	39.79	1.66071	2	2	0	Zirconium Carbide
57.42	10.19	1.60349	1	6	1	Corundum
65.92	28.01	1.41588	3	1	1	Zirconium Carbide
66.44	4.38	1.40606	1	4	2	Corundum
68.13	5.69	1.37524	0	0	3	Corundum
69.26	10.84	1.35551	2	2	2	Zirconium Carbide
82.04	4.25	1.17366	4	0	0	Zirconium Carbide
91.34	8.59	1.07689	3	3	1	Zirconium Carbide
94.43	10.80	1.04959	4	2	0	Zirconium Carbide
95.17	2.23	1.04337	2	6	2	Corundum
107.04	8.04	0.95801	4	2	2	Zirconium Carbide
116.02	1.79	0.90822	2	4	3	Corundum
117.06	5.04	0.90314	5	1	1	Zirconium Carbide

S1.00 – 1400

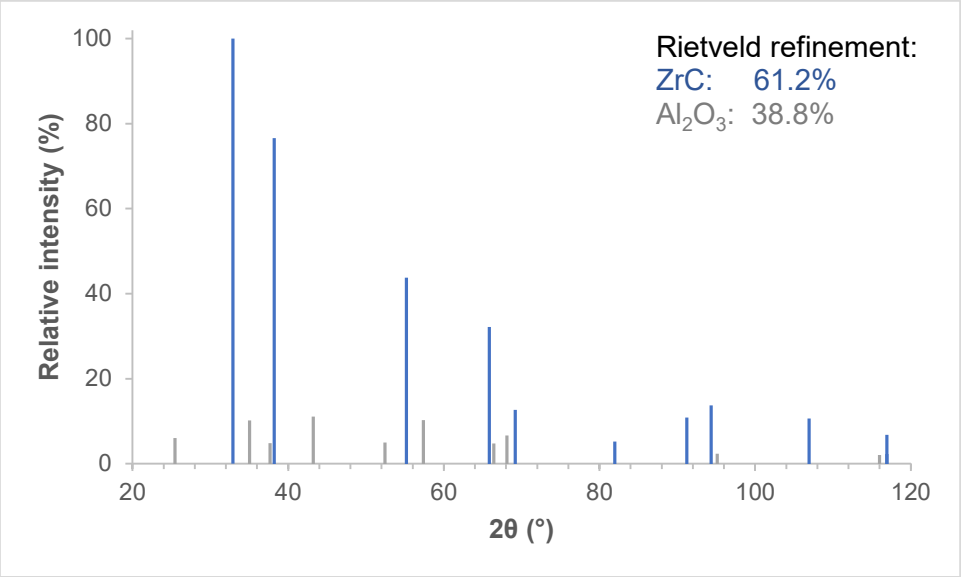

Pos. (°2θ)	Rel. Int. (%)	d-spacing (Å)	h	k	l	Phase Assignment
25.46	6.06	3.49531	0	-2	1	Corundum
32.92	100.00	2.7188	1	1	1	Zirconium Carbide
35.04	10.21	2.55893	0	4	1	Corundum
37.66	4.80	2.38642	1	0	1	Corundum
38.21	76.59	2.35339	2	0	0	Zirconium Carbide
43.24	11.10	2.09061	1	3	1	Corundum
52.44	4.97	1.7435	0	-4	2	Corundum
55.21	43.78	1.66249	2	2	0	Zirconium Carbide
57.39	10.27	1.60432	1	6	1	Corundum
65.85	32.19	1.41725	3	1	1	Zirconium Carbide
66.41	4.77	1.40666	1	4	2	Corundum
68.10	6.61	1.37581	0	0	3	Corundum
69.19	12.63	1.35679	2	2	2	Zirconium Carbide
81.95	5.19	1.17466	4	0	0	Zirconium Carbide
91.24	10.82	1.07776	3	3	1	Zirconium Carbide
94.33	13.73	1.05042	4	2	0	Zirconium Carbide
95.14	2.36	1.04363	2	6	2	Corundum
106.93	10.59	0.95872	4	2	2	Zirconium Carbide
115.99	2.01	0.90838	2	4	3	Corundum
116.93	6.79	0.90377	5	1	1	Zirconium Carbide

S0.25 – 1500

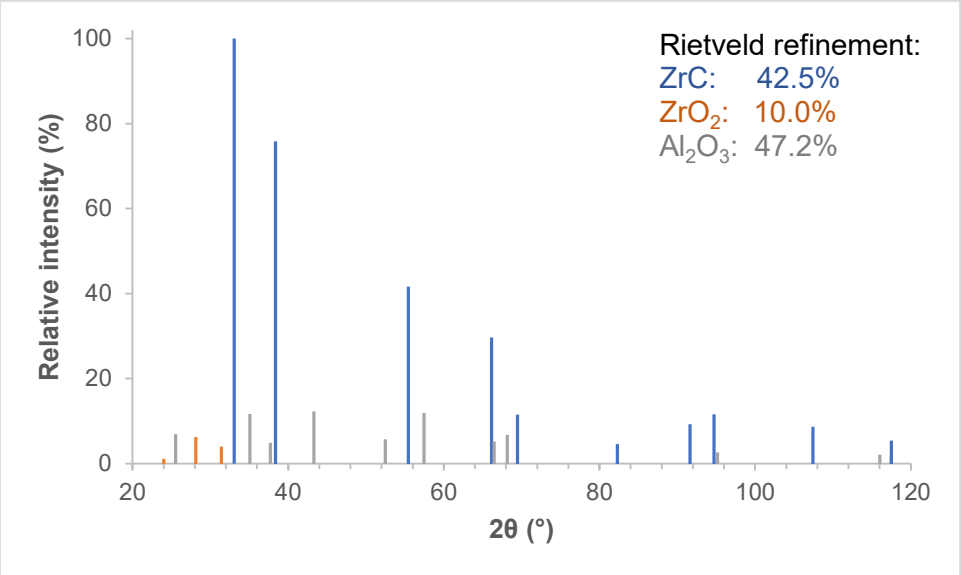

Pos. (°2θ)	Rel. Int. (%)	d-spacing (Å)	h	k	l	Phase Assignment
24.02	1.14	3.70207	1	1	0	Baddeleyite
25.52	6.93	3.48783	0	-2	1	Corundum
28.14	6.24	3.16855	1	1	-1	Baddeleyite
31.41	4.01	2.84546	1	1	1	Baddeleyite
33.07	100.00	2.70662	1	1	1	Zirconium Carbide
35.09	11.69	2.55501	0	4	1	Corundum
37.72	4.89	2.38304	1	0	1	Corundum
38.38	75.84	2.34341	2	0	0	Zirconium Carbide
43.30	12.26	2.08807	1	3	1	Corundum
52.49	5.70	1.74179	0	-4	2	Corundum
55.43	41.60	1.65622	2	2	0	Zirconium Carbide
57.44	11.92	1.60291	1	6	1	Corundum
66.11	29.66	1.41217	3	1	1	Zirconium Carbide
66.46	5.16	1.40563	1	4	2	Corundum
68.15	6.75	1.37483	0	0	3	Corundum
69.47	11.51	1.35198	2	2	2	Zirconium Carbide
82.29	4.55	1.17067	4	0	0	Zirconium Carbide
91.63	9.22	1.07419	3	3	1	Zirconium Carbide
94.74	11.59	1.04696	4	2	0	Zirconium Carbide
95.19	2.61	1.04318	2	6	2	Corundum
107.42	8.62	0.95565	4	2	2	Zirconium Carbide
117.52	5.38	0.90094	5	1	1	Zirconium Carbide

S0.50 – 1500

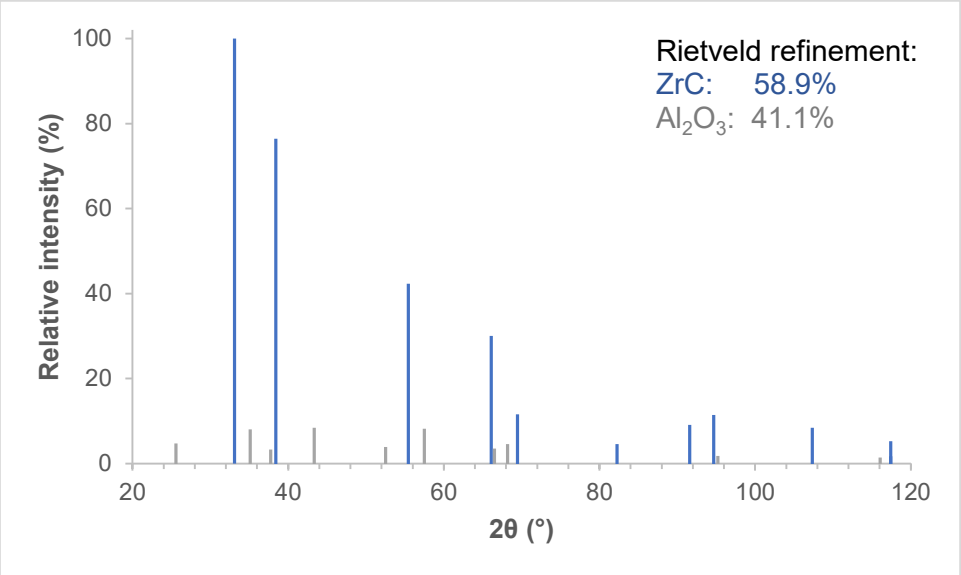

Pos. (°2θ)	Rel. Int. (%)	d-spacing (Å)	h	k	l	Phase Assignment
25.56	4.74	3.48233	0	-2	1	Corundum
33.09	100.00	2.70518	1	1	1	Zirconium Carbide
35.13	8.02	2.55213	0	4	1	Corundum
37.76	3.31	2.38055	1	0	1	Corundum
38.39	76.42	2.34258	2	0	0	Zirconium Carbide
43.34	8.41	2.08619	1	3	1	Corundum
52.54	3.90	1.74054	0	-4	2	Corundum
55.43	42.29	1.65621	2	2	0	Zirconium Carbide
57.49	8.19	1.60187	1	6	1	Corundum
66.10	30.01	1.41234	3	1	1	Zirconium Carbide
66.50	3.54	1.40487	1	4	2	Corundum
68.19	4.57	1.37411	0	0	3	Corundum
69.45	11.62	1.3522	2	2	2	Zirconium Carbide
82.27	4.55	1.17098	4	0	0	Zirconium Carbide
91.59	9.13	1.07454	3	3	1	Zirconium Carbide
94.70	11.46	1.04732	4	2	0	Zirconium Carbide
95.23	1.79	1.04284	2	6	2	Corundum
107.36	8.45	0.95604	4	2	2	Zirconium Carbide
116.08	1.45	0.90791	2	4	3	Corundum
117.43	5.25	0.90135	5	1	1	Zirconium Carbide

S0.75 – 1500

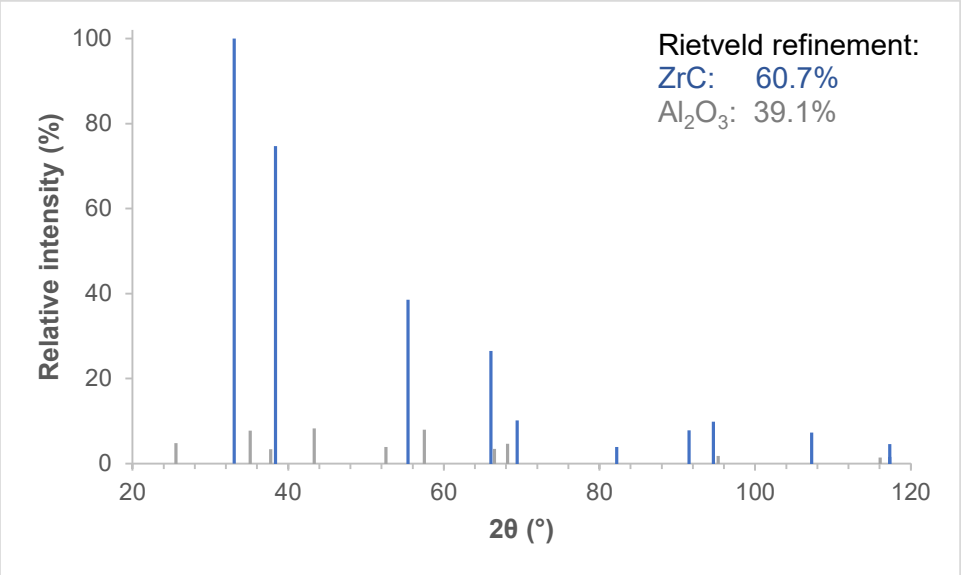

Pos. (°2θ)	Rel. Int. (%)	d-spacing (Å)	h	k	l	Phase Assignment
25.56	4.77	3.48159	0	-2	1	Corundum
33.07	100.00	2.70656	1	1	1	Zirconium Carbide
35.14	7.72	2.55174	0	4	1	Corundum
37.76	3.36	2.38022	1	0	1	Corundum
38.37	74.72	2.34383	2	0	0	Zirconium Carbide
43.34	8.28	2.08594	1	3	1	Corundum
52.54	3.93	1.74037	0	-4	2	Corundum
55.40	38.54	1.65717	2	2	0	Zirconium Carbide
57.49	7.98	1.60173	1	6	1	Corundum
66.06	26.48	1.41319	3	1	1	Zirconium Carbide
66.51	3.46	1.40476	1	4	2	Corundum
68.20	4.65	1.37401	0	0	3	Corundum
69.41	10.18	1.35301	2	2	2	Zirconium Carbide
82.21	3.91	1.17171	4	0	0	Zirconium Carbide
91.52	7.83	1.07521	3	3	1	Zirconium Carbide
94.62	9.83	1.04798	4	2	0	Zirconium Carbide
95.24	1.77	1.0428	2	6	2	Corundum
107.26	7.30	0.95665	4	2	2	Zirconium Carbide
116.09	1.44	0.90788	2	4	3	Corundum
117.31	4.58	0.90193	5	1	1	Zirconium Carbide

S1.00 – 1500

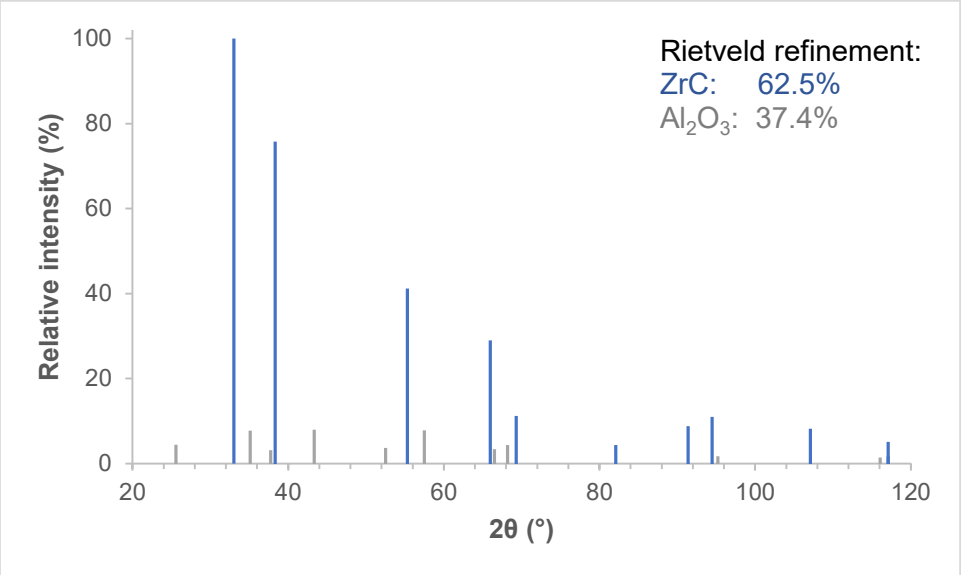

Pos. (°2θ)	Rel. Int. (%)	d-spacing (Å)	h	k	l	Phase Assignment
25.56	4.46	3.48226	0	-2	1	Corundum
33.03	100.00	2.70982	1	1	1	Zirconium Carbide
35.14	7.75	2.55209	0	4	1	Corundum
37.76	3.16	2.38052	1	0	1	Corundum
38.33	75.78	2.34660	2	0	0	Zirconium Carbide
43.34	7.96	2.08617	1	3	1	Corundum
52.54	3.67	1.74052	0	-4	2	Corundum
55.33	41.17	1.65906	2	2	0	Zirconium Carbide
57.49	7.85	1.60185	1	6	1	Corundum
65.98	28.96	1.41477	3	1	1	Zirconium Carbide
66.50	3.36	1.40486	1	4	2	Corundum
68.19	4.36	1.37410	0	0	3	Corundum
69.32	11.20	1.35452	2	2	2	Zirconium Carbide
82.10	4.36	1.17300	4	0	0	Zirconium Carbide
91.39	8.76	1.07639	3	3	1	Zirconium Carbide
94.48	11.00	1.04913	4	2	0	Zirconium Carbide
95.23	1.70	1.04284	2	6	2	Corundum
107.09	8.18	0.95769	4	2	2	Zirconium Carbide
116.08	1.38	0.90791	2	4	3	Corundum
117.11	5.13	0.90290	5	1	1	Zirconium Carbide

ZrC Standard (Sigma Aldrich batch number: 336351; with added Al_2O_3)

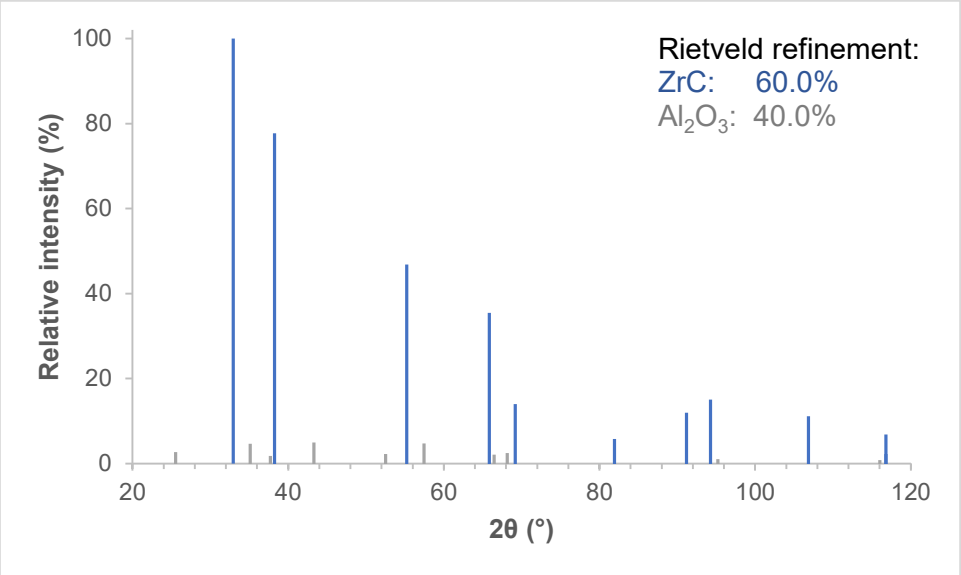

Pos. (°2θ)	Rel. Int. (%)	d-spacing (Å)	h	k	l	Phase Assignment
25.52	2.70	3.48707	0	-2	1	Corundum
32.95	100.00	2.71623	1	1	1	Zirconium Carbide
35.10	4.63	2.55461	0	4	1	Corundum
37.72	1.80	2.38270	1	0	1	Corundum
38.24	77.73	2.35179	2	0	0	Zirconium Carbide
43.30	4.93	2.08781	1	3	1	Corundum
52.50	2.22	1.74162	0	-4	2	Corundum
55.22	46.86	1.66222	2	2	0	Zirconium Carbide
57.45	4.72	1.60277	1	6	1	Corundum
65.84	35.46	1.41731	3	1	1	Zirconium Carbide
66.47	2.09	1.40552	1	4	2	Corundum
68.16	2.49	1.37473	0	0	3	Corundum
69.18	14.01	1.35691	2	2	2	Zirconium Carbide
81.93	5.82	1.17495	4	0	0	Zirconium Carbide
91.20	11.97	1.07813	3	3	1	Zirconium Carbide
94.29	15.07	1.05080	4	2	0	Zirconium Carbide
95.20	1.05	1.04313	2	6	2	Corundum
106.85	11.11	0.95917	4	2	2	Zirconium Carbide
116.05	0.82	0.90808	2	4	3	Corundum
116.83	6.84	0.90426	5	1	1	Zirconium Carbide

Example of the XRD patterns in Chapter 5

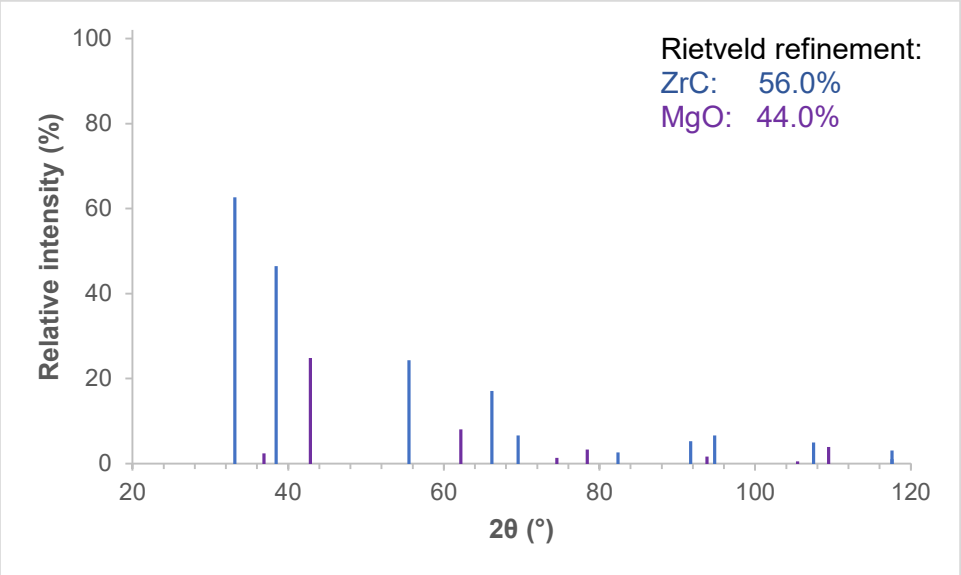

Pos. (°2θ)	Rel. Int. (%)	d-spacing (Å)	h	k	l	Phase Assignment
33.14	62.66	2.70101	1	1	1	Zirconium Carbide
36.87	2.41	2.43584	1	1	1	Periclase
38.45	46.48	2.33923	2	0	0	Zirconium Carbide
42.83	24.85	2.10957	2	0	0	Periclase
55.51	24.32	1.6542	2	2	0	Zirconium Carbide
62.18	8.08	1.49179	2	2	0	Periclase
66.19	17.07	1.41075	3	1	1	Zirconium Carbide
69.54	6.61	1.3507	2	2	2	Zirconium Carbide
74.53	1.36	1.27224	3	1	1	Periclase
78.45	3.30	1.21808	2	2	2	Periclase
82.37	2.60	1.16976	4	0	0	Zirconium Carbide
91.71	5.26	1.07346	3	3	1	Zirconium Carbide
93.81	1.66	1.05491	4	0	0	Periclase
94.82	6.62	1.04629	4	2	0	Zirconium Carbide
105.44	0.52	0.96807	3	3	1	Periclase
107.51	4.95	0.95514	4	2	2	Zirconium Carbide
109.45	3.91	0.94356	4	2	0	Periclase
117.61	3.11	0.90052	5	1	1	Zirconium Carbide